Spring 2019

Quantized Circulation in Racetrack Atomtronic Circuits at Non-Zero Temperature

Benjamin R. Eller

QUANTIZED CIRCULATION IN RACETRACK ATOMTRONIC CIRCUITS AT NON-ZERO TEMPERATURE

by

BENJAMIN ELLER

(Under the Direction of Mark Edwards)

ABSTRACT

We extend previous theoretical investigations of the creation of quantized circulation states by stirring Bose-Einstein condensates (BEC) confined in “racetrack" potentials. The previous study, *Producing Smooth Flow in Atom Circuits by Stirring*, used the Gross-Pitaevskii equation (GPE), which is valid at $T = 0$ K. Here we use a non-zero temperature model based on the Zaremba, Nikuni, Griffin (ZNG) theory to simulate stirring racetrack BECs. The two main goals of this thesis are 1) to understand the effects of temperature on the production of circulation and 2) to understand the mechanism by which the circulation is excited. We find that it is possible to produce circulation at non-zero T in much the same way as at absolute zero, and the consideration of thermal effects is important for determining the precise amount of circulation obtained by stirring for a fixed total number of atoms. We also present a case study of the mechanism by which stirring produces flow in the GPE model.

INDEX WORDS: Bose–Einstein condensate, Atom circuit, Non-zero temperature

QUANTIZED CIRCULATION IN RACETRACK ATOMTRONIC CIRCUITS AT NON-ZERO TEMPERATURE

by

BENJAMIN ELLER

B.S, Georgia Southern University, 2017

A Thesis Submitted to the Graduate Faculty of Georgia Southern University in Partial Fulfillment of the Requirements for the Degree

MASTER OF SCIENCE

STATESBORO, GEORGIA

QUANTIZED CIRCULATION IN RACETRACK ATOMTRONIC CIRCUITS AT NON-ZERO TEMPERATURE

by

BENJAMIN ELLER

Major Professor: Mark Edwards

Committee: Monique Aller

Ryan Fortenberry

Electronic Version Approved:

May 2019

DEDICATION

I dedicate this thesis to my family. Their support and encouragement has allowed me to find a clear purpose in life.

ACKNOWLEDGMENTS

Nothing is truly completed by an individual themselves. I would like to thank my advisor, Dr. Mark Edwards, for all of his assistance during the course of my studies and this research project. I would not be where I am today if not for his mentorship. I would also like to thank Drs. Monique Aller and Ryan Fortenberry for their investment of time as members of my graduate committee. Furthermore, I want to thank the Physics Department of Georgia Southern University. I cannot count how many pleasant and interesting conversations I have had with the faculty, staff, and students of this Department. These conversations have certainly helped me along my way.

TABLE OF CONTENTS

LIST OF FIGURES

LIST OF TABLES

CHAPTER 1

INTRODUCTION

When a gas of atoms is cooled down and its temperature approaches absolute zero, the matter-wave characteristics become pronounced. This can be understood by considering the behavior of the average matter-wavelength of the constituent atoms of the gas, $\lambda_{\mathrm{dB}} = h/p$. As the temperature is lowered, the average momentum p decreases as well, resulting in an increase of λ_{dB}. If the atoms are identical bosons confined in a box, at some point their average wavelength becomes comparable to the average inter-particle spacing, $\lambda_{\mathrm{dB}} \sim \rho^{-1/3}$, where ρ is the number density. When this happens their matter-waves can interlock and they all share the same single-particle wavefunction. This is a Bose-Einstein condensate (BEC).

After a laboratory BEC was created in trapped atomic gases in 1995 [1, 2], researchers began using them as a test-bed for theories of superfluidity and condensed matter. Since then, ultra-cold atomic systems have become a versatile and widely used system for physics research. Some examples of such research include the investigation of states that obey anyonic statistics [3, 4], simulation of the expansion of the universe in a laboratory [5], and the realization of circuits that use neutral atom currents [6]. This thesis falls under the category of this last development, which is termed *atomtronics* [7]. There has been much research done involving atomic BECs after they were created in the lab, see Refs. [8] and [9] and references therein for a broad overview.

The bulk of the theoretical research examining the properties and behavior of

atomic BECs is based on the Gross-Pitaevskii equation (GPE). However, the GPE model does not account for the effects of non-zero temperature. Since the 3rd law of thermodynamics prevents any system from reaching absolute zero temperature in a finite number of operations, the importance of the effects of non-zero temperature needs to be investigated. There are a number of non-zero temperature models. These are briefly discussed in section 2. In this work we use the Zaremba, Nikuni, and Griffin (ZNG) model [10], to extend to non-zero T a previous study [11] where the GPE was used to simulate the production of macroscopic flow by stirring BECs confined in “racetrack" potentials. The racetrack potential consists of two semi-circular channels connected by straight channels of length L.

1.1 The Gross-Pitaevskii Equation

The time-dependent Gross-Pitaevskii equation models a system of identical bosons and assumes that all of the particles are in the same single-particle state. This equation has the form:

$$i\hbar\frac{\partial}{\partial t}\Phi(\mathbf{r},t) = \left(\frac{-\hbar^2}{2m}\nabla^2 + V_{\text{trap}}(\mathbf{r},t) + gn_c(\mathbf{r},t)\right)\Phi(\mathbf{r},t) \tag{1.1}$$

where $\Phi(\mathbf{r},t)$ is the condensate wavefunction that all of the atoms in the BEC share so that $n_c(\mathbf{r},t) = \Phi^*(\mathbf{r},t)\Phi(\mathbf{r},t)$ is the condensate density. In the above equation, m is the mass of a condensate atom, V_{trap} is the external potential that the BEC sits in, $g = 4\pi\hbar^2 a_s/m$ determines the strength of binary scattering, and a_s is the s-wave scattering length. A derivation of the GPE is presented in Appendix A.

More often than not this equation needs to be solved numerically, although there exist some exact solutions. The system that we will consider requires the numerical approach. The GPE reduces to the linear single-particle Schrödinger equation if $g = 0$, and even if not shares some important features with it. One of those features is the quantization of circulation, as we describe next.

1.2 Quantization of Circulation

The "circulation" of a fluid around a closed path is a measure of flow of the fluid along the path. In this section we motivate and present a quantitative definition of this quantity and relate it to the condensate wavefunction.

We can compute the time derivative of the condensate density $n_c(\mathbf{r},t)$ and use the GPE and its complex conjugate to show that the probability distribution governed by the time-dependent Schrödinger equation and GPE obeys a continuity equation:

$$\frac{\partial n_c}{\partial t} = -\boldsymbol{\nabla}\cdot\mathbf{j}, \tag{1.2}$$

which is a statement of the conservation of probability. The probability current $\mathbf{j}$ is defined by

$$\mathbf{j}(\mathbf{r},t) = \frac{\hbar}{2mi}\left(\Phi^*\boldsymbol{\nabla}\Phi - \Phi\boldsymbol{\nabla}\Phi^*\right) \tag{1.3}$$

where m is the mass of a condensate atom, and $i = \sqrt{-1}$. We can define the velocity field $\mathbf{v}_c(\mathbf{r},t)$ of the condensate in terms of the probability current as

$$\mathbf{j}(\mathbf{r},t) = n_c(\mathbf{r},t)\mathbf{v}_c(\mathbf{r},t).$$

By introducing the phase, $\theta(\mathbf{r},t)$, and amplitude, $A(\mathbf{r},t)$, of the complex-valued wavefunction $\Phi(\mathbf{r},t) = A(\mathbf{r},t)e^{i\theta(\mathbf{r},t)}$, it can be shown that the velocity of the condensate is proportional to the gradient of the phase of the wavefunction:

$$\mathbf{v}_c(\mathbf{r},t) = \frac{\hbar}{m}\nabla\theta(\mathbf{r},t). \tag{1.4}$$

We can compute the path-integral of this velocity field between two points in space $\mathbf{r}_\mathrm{i}$ and $\mathbf{r}_\mathrm{f}$

$$\tilde{\mathscr{C}}(t) = \int_P \mathbf{v}_c(\mathbf{r},t)\cdot d\mathbf{r} \tag{1.5}$$

where the integration is along a specified, directed path P. The path P is a piece-wise smooth continuous curve that connects $\mathbf{r}_\mathrm{i}$ and $\mathbf{r}_\mathrm{f}$, and $d\mathbf{r}$ is a line element along P. With this we can define the circulation of the condensate around the given path P by letting $\mathbf{r}_\mathrm{i} = \mathbf{r}_\mathrm{f}$ and write it as

$$\mathscr{C}(t) \equiv \oint_P \mathbf{v}_c(\mathbf{r},t)\cdot d\mathbf{r}, \tag{1.6}$$

and this is illustrated in Fig. 1.1. The quantization of the circulation of a BEC arises from the requirement of single-valuedness of the wavefunction and is a general feature of the linear Schrödinger equation as well as the GPE and the generalized GPE that is introduced

in Sec. 2.2 as part of the ZNG model. We can make use of Eq. (1.4):

$$\begin{aligned}\mathscr{C}(t) &= \oint_P \mathbf{v}_c(\mathbf{r},t)\cdot d\mathbf{r} \\ &= \frac{\hbar}{m}\oint_P \nabla\theta(\mathbf{r},t)\cdot d\mathbf{r} \\ &= \frac{\hbar}{m}\big(\theta(\mathbf{r}_\mathrm{f},t)-\theta(\mathbf{r}_\mathrm{i},t)\big) \\ &= \frac{2\pi\hbar w(t)}{m}\end{aligned} \tag{1.7}$$

where $w(t)$ is an integer, which we will often refer to as the "winding number." The accumulated phase around the closed path must be an integer multiple of 2π because the condensate wavefunction must be single-valued:

$$\begin{aligned}\Phi(\mathbf{r}_\mathrm{f},t) &= \Phi(\mathbf{r}_\mathrm{i},t) \\ |\Phi(\mathbf{r}_\mathrm{f},t)|e^{i\theta(\mathbf{r}_\mathrm{f},t)} &= |\Phi(\mathbf{r}_\mathrm{i},t)|e^{i\theta(\mathbf{r}_\mathrm{i},t)},\end{aligned} \tag{1.8}$$

and we can write

$$\theta(\mathbf{r}_\mathrm{f},t) = \theta(\mathbf{r}_\mathrm{i},t) + 2\pi w(t). \tag{1.9}$$

Thus, the circulation is quantized in units of (h/m). The creation and destruction of states with non-zero w is a central theme in the operation of our atom circuits. In Fig. 1.1, the path shown encloses several vortex lines. We note that $\nabla\times\mathbf{v}_c = 0$, except on the line of a vortex. This means that $\mathbf{v}_c$ is a conservative vector field, and so the path P can be deformed arbitrarily, as long as it does not cross a vortex line. This deformation is illustrated in Fig. 1.1, and it shows that the winding number represents the net number of vortices enclosed by the path of integration P since we can equivalently integrate around concentric

circles enclosing each vortex line. Therefore, a calculation of Eq. (1.7) for Fig. 1.1 would yield a circulation proportional to a winding number $w = 1$.

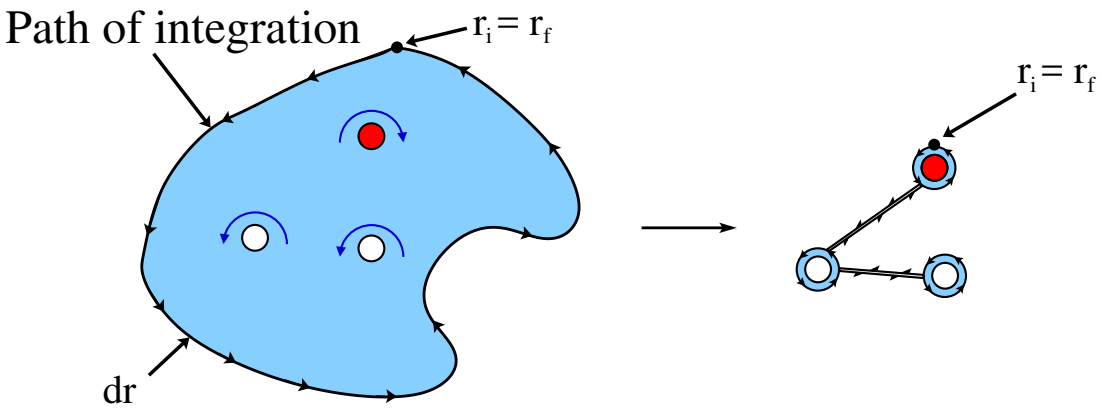

Figure 1.1: A visual aid for circulation calculations. The white holes represent counter-clockwise (CCW) vortices and the red hole a clockwise (CW) vortex.

1.3 Atom Circuits

Atom circuits are analogous to electric circuits, except that instead of electric charge flowing there is a neutral-atom current. The design and study of such systems is known as atomtronics. Atom circuits consisting of Bose-Einstein condensed gases confined and manipulated by laser light have potential for applications and fundamental physics research, due to the relative ease with which system parameters can be tuned. A major advantage of using BECs is the fact that they are coherent matter, and as such can be used for interferometric routines [12, 13]. This matter-wave interference can then be used to create quantum sensors. Matter-wave rotation sensing schemes making use of the Sagnac effect can boost sensitivity improvements on the order of 10^{11} compared to light-based schemes

with the same area [14].

There is also the prospect of using atomtronic systems for the physical implementation of a quantum computer owing to the coherent nature of BECs and their long decoherence time. Researchers are on the hunt for atomtronic-enabled quantum computing [15, 16]. Atomtronic systems can also be used as “simulators" of physical phenomena not easily accessible in other systems. Currently experimentalists can precisely tune system parameters including the strength of interactions via a Feshbach resonance [8, 17] and the trapping potential energy landscape [18].

Modern society relies heavily on electronic circuitry. Almost everything we do seems to involve the use of electricity, be it preparing food, operating machinery, saving lives, or communicating with each other. Before electronic circuits became as pervasive and useful as they are now, scientists and engineers had to develop an understanding of the basic principles that govern their behavior. This is the stage we are at now with atomtronics. A few basic components of atom circuits have been designed and studied [6, 19], and an important next step would be to come up with a standard set of rules for a lumped abstract model, akin to those used in basic electronics such as Kirchoff’s loop and junction rules.

In 2013, a group at the Joint Quantum Institute performed experiments wherein they formed BECs into rings in an all-optical trap and excited units of quantized circulation in them by stirring with focused laser beams scanned across the channel fast enough to produce a time-averaged flat barrier [20]. This thesis work is inspired by these experiments, and it generalizes the ring geometry to a racetrack, described in Sec. 3.1, in order to have

room for atom circuit elements.

If macroscopic circulation can be excited in more generalized geometries than rings, more possibilities for atomtronics applications will be opened up for the future. Figure 1.2 shows an idealized picture of possible atom circuit operation. The first step is to create a BEC in the confining potential as shown in panel a) of Fig. 1.2. The next step is to create flow by some means, e.g. stirring the BEC, shown in panels b) and c). Once a state of overall circulation is present, the trapping potential can be modified in realtime in order to realize some sort of application. As an example, panel d) of Fig. 1.2 shows a ring formed along the path of the racetrack.

It is clear from this idealized atom-circuit model that creating smooth flow in the BEC is an essential component of its operation. In this thesis we are interested in studying whether and how smooth flow can be created in an atom-circuit BEC by stirring it with a barrier. In addition, we are also interested in understanding the mechanism for production of flow. A previous work [11] considered the question of making flow in a condensate by stirring using a zero temperature model based on the GPE. The study presented here extends that work with a non-zero temperature model, the ZNG model, which is briefly reviewed in the next chapter.

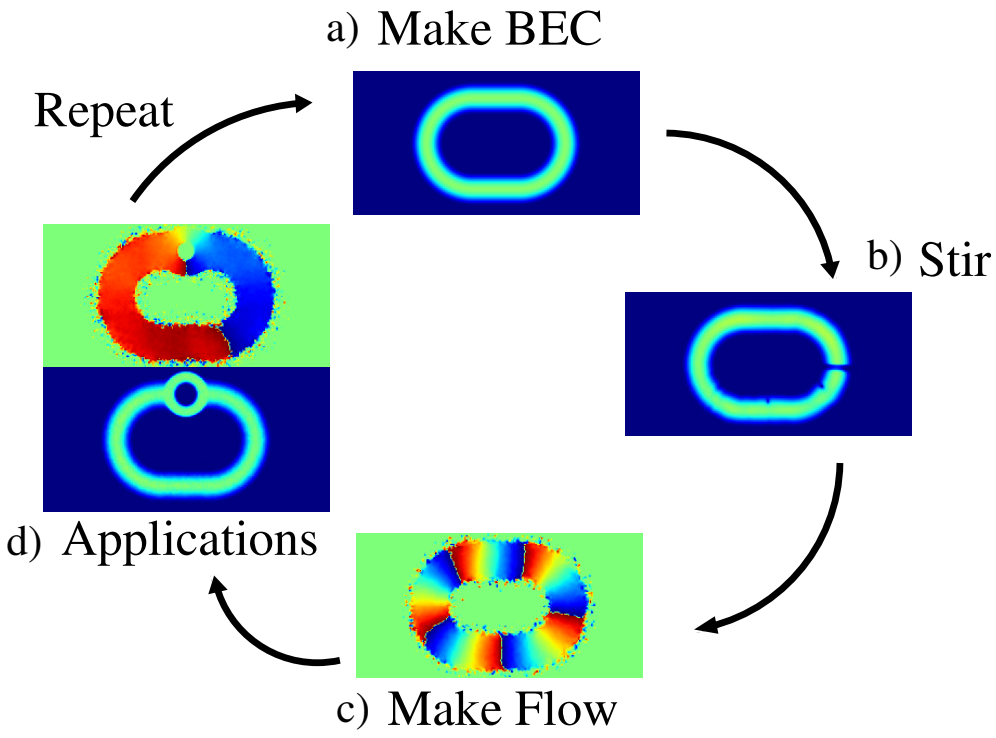

Figure 1.2: Depiction of atom circuit operation. The images with the dark blue backgrounds show the density of the BEC, dark blue corresponding to zero. The images with the green backgrounds (and the bands) are the phase of the condensate wavefunction in the $z = 0$ plane, with the color scale representing the phase from $-\pi$ to π, going from blue to red. The number of bands is given by Eq. (1.7).

CHAPTER 2

MODELING THE EFFECTS OF TEMPERATURE

2.1 The Zaremba-Nikuni-Griffin (ZNG) Model

In order to study the effect that non-zero temperature has on these ultra-cold atomic systems, which exist at temperatures $T \sim 10^{-7}$ K, a model beyond the zero-temperature GPE model is needed. Here we illustrate the ideas behind the ZNG model by imagining a system of identical bosonic particles confined in a harmonic oscillator potential in which the different atoms can occupy different energy levels. Figure 2.1 shows an example of how the particles are distributed among the different energy levels. Since we are dealing with bosons, an arbitrary number of them can occupy the same state. If the temperature is below a critical value, T_c, a large fraction of the particles occupy the ground state. This is the condensate. At temperature T, the non-condensate atoms are distributed according to the Bose-Einstein distribution, which gives the average number of bosons in a state with energy $\tilde{\varepsilon}_j$ in thermal equilibrium,

$$f^0(\tilde{\varepsilon}_j) = \frac{1}{e^{(\tilde{\varepsilon}_j - \tilde{\mu})/k_B T} - 1}, \tag{2.1}$$

where k_B is the Boltzmann constant. The chemical potential, $\tilde{\mu}$, of the non-condensate is the energy required to add another non-condensate atom.

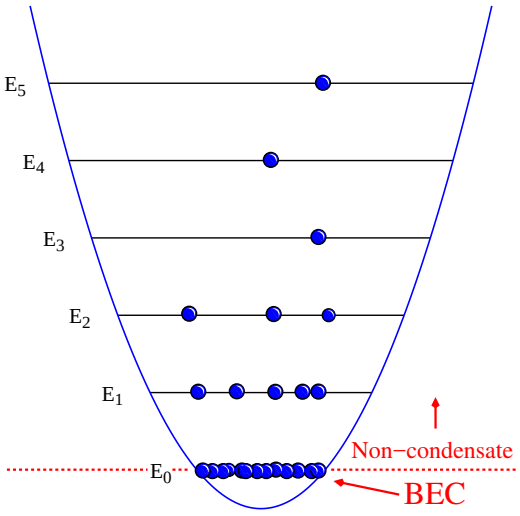

Figure 2.1: A representation of indistinguishable bosons distributed over allowed energy levels. The dotted line is an energy cutoff below which the energy levels have occupations $N_j >> 1$.

Many non-zero T theories such as the truncated Wigner approximation (TWA), stochastic-projected GPE (SPGPE), and the ZNG model determine an energy cutoff below which the system energy levels have occupations much greater than unity. This cutoff is shown as the dotted line in Fig. 2.1. Identifying the location of this dotted line is done mathematically by taking the bose field operator $\hat{\psi}(\mathbf{r},t)$ that destroys a boson at position $\mathbf{r}$ and time t and separating the ground state level from the rest like so [21]:

$$\hat{\psi}(\mathbf{r},t) = \hat{b}_0(t)\varphi_0(\mathbf{r},t) + \sum_{n\neq 0} \hat{b}_n(t)\varphi_n(\mathbf{r},t) \tag{2.2}$$

where the $\varphi_n(\mathbf{r},t)$ are the single-particle wavefunctions for the different levels and the $\hat{b}_n(t)(\hat{b}_n^{\dagger}(t))$ are operators that annihilate(create) a boson in the state $\varphi_n(\mathbf{r},t)$. If the occupation of the level $n = 0$ (ground state) is much larger than unity, $N_0 >> 1$, we can make

an approximation [22] and replace the annihilation(creation) operators $\hat{b}_0(t)(\hat{b}_0^\dagger(t))$ with complex numbers, since in that limit they approximately commute. We can see this by acting the commutator of single-particle operators corresponding on the state having N_j bosons in it:

$$\begin{aligned}
[\hat{b}_j, \hat{b}_j^\dagger]\,|N_j\rangle &= (\hat{b}_j\hat{b}_j^\dagger - \hat{b}_j^\dagger\hat{b}_j)\,|N_j\rangle \\
[\hat{b}_j, \hat{b}_j^\dagger]\,|N_j\rangle &= ((N_j+1) - N_j)\,|N_j\rangle \\
[\hat{b}_j, \hat{b}_j^\dagger]\,|N_j\rangle &\approx (0)\,|N_j\rangle
\end{aligned} \tag{2.3}$$

in the limit $N_j >> 1$. We can therefore write the field operator as

$$\hat{\psi}(\mathbf{r},t) = \hat{I}\Phi(\mathbf{r},t) + \sum_{n\neq 0} \hat{b}_n(t)\varphi_n(\mathbf{r},t) \tag{2.4}$$

where $\hat{I}$ is the identity operator and we have introduced the condensate wavefunction $\Phi(\mathbf{r},t) \equiv \sqrt{N_0}\varphi_0(\mathbf{r},t)$, following the notation of [10]. Doing this is equivalent to saying that $\Phi(\mathbf{r},t) = \langle\hat{\psi}(\mathbf{r},t)\rangle$, and if we define $\tilde{\psi}(\mathbf{r},t) \equiv \sum_{n\neq 0}\hat{b}_n(t)\varphi_n(\mathbf{r},t)$ then we can write

$$\langle\tilde{\psi}(\mathbf{r},t)\rangle = 0. \tag{2.5}$$

The ZNG model sets the cutoff just at the lowest level, whose occupation is much larger than all others. The system is therefore composed of two distinct components, one component a BEC, the other a non-condensate as illustrated in Fig. 2.1. From the equation $\hat{\psi}(\mathbf{r},t) = \hat{I}\Phi(\mathbf{r},t) + \tilde{\psi}(\mathbf{r},t)$, and with the Heisenberg equation of motion for the operator $\hat{\psi}(\mathbf{r},t)$, equations of motion for the condensate wavefunction and the non-condensate field operator can be found [10]. Other theoretical approaches to the problem of modeling bosonic gases at low temperatures, such as the TWA and SPGPE, differ at their heart in

how the bose field operator $\hat{\psi}(\mathbf{r},t)$ is separated, and low lying atoms not in the BEC but below an energy cutoff are included in $\Phi(\mathbf{r},t)$. Therefore, $\Phi(\mathbf{r},t)$ no longer represents the condensate itself.

While the implementation of these other methods can be simpler (in that they only require a slight modification to existing GPE solving code), the physics is less clear. That is to say, figuring out what is and is not the BEC requires post-processing after the solutions of the models have been obtained. We are most interested in the dynamics of the BEC since it has interesting quantum mechanical properties that can be exploited for atomtronics. With the ZNG, the implementation requires more work up front but the solutions are clearly divided as to what is in the BEC and what is not. A review of the various methods employed in the low temperature bosonic gas modeling field is given in Ref. [21].

2.2 ZNG Equations of Motion

The ZNG model assumes a fraction of the fixed total number of atoms is in the BEC and the rest are in the non-condensate. Therefore equations of motion are needed for both components. Of course, the effect of the two components on each other will have to be incorporated into their respective governing equations. The non-condensate affects the dynamics of the condensate in two ways: 1) by adding a density-dependent mean-field contribution to the interaction term of the Hamiltonian, and 2) by colliding with the condensate atoms, which enables the condensate and non-condensate to exchange particles.

The behavior of the condensate is described by a condensate wavefunction, $\Phi(\mathbf{r},t)$.

The evolution of $\Phi(\mathbf{r},t)$ is governed by a generalized Gross-Pitaevskii equation (GGPE) [10]:

$$i\hbar\frac{\partial}{\partial t}\Phi(\mathbf{r},t) = \left(\frac{-\hbar^2}{2m}\nabla^2 + V_{\text{trap}}(\mathbf{r},t) + gn_c(\mathbf{r},t) + 2g\tilde{n}(\mathbf{r},t) - iR(\mathbf{r},t)\right)\Phi(\mathbf{r},t). \tag{2.6}$$

Here $n_c(\mathbf{r},t) = |\Phi|^2$ is the condensate density, $\tilde{n}(\mathbf{r},t)$ is the non-condensate density, and $R(\mathbf{r},t)$ is a local source & sink term that accounts for the exchange of atoms into and out of the condensate. In the limit that $T \to 0$, Eq. (2.6) reduces to the GPE, Eq. (1.1), since the quantities $R(\mathbf{r},t)$ and $\tilde{n}(\mathbf{r},t)$ both vanish at absolute zero. In reality, a small fraction of atoms are not in the condensate even at $T = 0$, but this fraction is typically less than 1% so it can be neglected for our purposes [8].

The non-condensate is described by a single-particle distribution function, $f(\mathbf{p},\mathbf{r},t)$, and is defined as the number of non-condensate atoms per differential volume of phase-space. Defining $d\tilde{N}(\mathbf{p},\mathbf{r},t)$ as the number of non-condensate atoms in a differential phase-space volume element $d^3p\,d^3r$ around momentum $\mathbf{p}$ and position $\mathbf{r}$ at time t, we can write

$$d\tilde{N}(\mathbf{p},\mathbf{r},t) = f(\mathbf{p},\mathbf{r},t)\frac{d^3p\,d^3r}{(2\pi\hbar)^3}. \tag{2.7}$$

From this definition we can calculate the local non-condensate density, $\tilde{n}(\mathbf{r},t)$, as

$$\tilde{n}(\mathbf{r},t) = \int \frac{d^3p}{(2\pi\hbar)^3}\, f(\mathbf{p},\mathbf{r},t). \tag{2.8}$$

The total number of atoms in the non-condensate, $\tilde{N}$, is given by

$$\tilde{N} = \int\int \frac{d^3p\,d^3r}{(2\pi\hbar)^3}\, f(\mathbf{p},\mathbf{r},t). \tag{2.9}$$

The single-particle distribution function, $f(\mathbf{p},\mathbf{r},t)$, [10] satisfies a quantum Boltzmann equation (QBE) that can be understood qualitatively as

$$\frac{\partial}{\partial t}f(\mathbf{p},\mathbf{r},t) = \left(\frac{\partial f}{\partial t}\right)_{\text{diff}} + \left(\frac{\partial f}{\partial t}\right)_{\text{force}} + \left(\frac{\partial f}{\partial t}\right)_{\text{coll}}. \tag{2.10}$$

In words, the time rate of change of $f(\mathbf{p},\mathbf{r},t)$ is determined by three separate considerations. First, atoms that are in a volume d^3r around $\mathbf{r}$ may leave that volume between t and $t+\delta t$ because of their momentum at time t, or atoms can move into d^3r because of their momentum. This diffusion effect is represented by the $(\partial f/\partial t)_{\text{diff}}$ term. Second, atoms may be pushed into or out of a volume d^3p around $\mathbf{p}$ between t and $t+\delta t$ by an external force field acting on them at their positions. This is represented by the $(\partial f/\partial t)_{\text{force}}$ term. Third, two non-condensate atoms may collide with each other, scattering them into and out of d^3p, or a collision of condensate and non-condensate particles may cause particles to be lost or gained by the non-condensate. This is represented by the $(\partial f/\partial t)_{\text{coll}}$ term.

We can determine a form for the diffusion and force terms by noting that, ignoring collisions, the system evolution obeys Hamilton's equation and so Liouville's theorem gives

$$f(\mathbf{p}+\mathbf{F}\delta t,\mathbf{r}+\frac{\mathbf{p}}{m}\delta t,t+\delta t) = f(\mathbf{p},\mathbf{r},t), \tag{2.11}$$

for small δt. Expanding the left-hand side in a Taylor series to first order we have

$$f(\mathbf{p}+\mathbf{F}\delta t,\mathbf{r}+\frac{\mathbf{p}}{m}\delta t,t+\delta t) \approx f(\mathbf{p},\mathbf{r},t) + \delta t\mathbf{F}\cdot\boldsymbol{\nabla}_p f + \delta t\frac{\mathbf{p}}{m}\cdot\boldsymbol{\nabla}_r f + \delta t\left(\frac{\partial f}{\partial t}\right) \tag{2.12}$$

Using Eq. (2.11) and dividing through by δt the expansion becomes

$$\frac{\partial f}{\partial t} - \boldsymbol{\nabla}_r U_{\text{eff}}\cdot\boldsymbol{\nabla}_p f + \frac{\mathbf{p}}{m}\cdot\boldsymbol{\nabla}_r f = 0 \tag{2.13}$$

where the force field has been written as minus the space-gradient of an effective potential felt by the non-condensate atoms, $\mathbf{F} = -\boldsymbol{\nabla}_r U_{\rm eff}$. Since we used an identity that is only valid in the absence of collisions, we can identify the second two terms in this equation as being the diffusion and force terms in Eq. (2.10).

Now we can rewrite Eq. (2.13) as

$$\frac{\partial f}{\partial t} - \boldsymbol{\nabla}_r U_{\rm eff} \cdot \boldsymbol{\nabla}_p f + \frac{\mathbf{p}}{m} \cdot \boldsymbol{\nabla}_r f = \left(\frac{\partial f}{\partial t}\right)_{\rm coll} \tag{2.14}$$

The collision term can be written as a pair of binary collision integrals [23] and in the ZNG model the final QBE that the non-equilibrium single-particle distribution satisfies is written

$$\frac{\partial f}{\partial t} - \boldsymbol{\nabla}_r U_{\rm eff} \cdot \boldsymbol{\nabla}_p f + \frac{\mathbf{p}}{m} \cdot \boldsymbol{\nabla}_r f = C_{12}[f,\Phi] + C_{22}[f]. \tag{2.15}$$

The collision integrals are [10]:

$$C_{12}[f(\mathbf{p},\mathbf{r},t),\Phi(\mathbf{r},t)] = \frac{2g^2 n_c}{(2\pi)^2\hbar^4}\int d^3p_1 \int d^3p_2 \int d^3p_3\, \Delta_{12}(\mathbf{v}_c,\mathbf{p},\mathbf{p}_1,\mathbf{p}_2,\mathbf{p}_3) \times [(1+f_1)f_2 f_3 - f_1(1+f_2)(1+f_3)] \tag{2.16}$$

$$C_{22}[f(\mathbf{p},\mathbf{r},t)] = \frac{2g^2}{(2\pi)^5\hbar^7}\int d^3p_2 \int d^3p_3 \int d^3p_4\, \Delta_{22}(\mathbf{p},\mathbf{p}_2,\mathbf{p}_3,\mathbf{p}_4) \times [(1+f)(1+f_2)f_3 f_4 - f f_2(1+f_3)(1+f_4)] \tag{2.17}$$

where

$$\Delta_{12}(\mathbf{v}_c,\mathbf{p},\mathbf{p}_1,\mathbf{p}_2,\mathbf{p}_3) = \delta(m\mathbf{v}_c + \mathbf{p}_1 - \mathbf{p}_2 - \mathbf{p}_3)\,\delta(\varepsilon_c + \tilde{\varepsilon}_{p_1} - \tilde{\varepsilon}_{p_2} - \tilde{\varepsilon}_{p_3}) \times \left[\delta(\mathbf{p}-\mathbf{p}_1) - \delta(\mathbf{p}-\mathbf{p}_2) - \delta(\mathbf{p}-\mathbf{p}_3)\right] \tag{2.18}$$

and

$$\Delta_{22}(\mathbf{p},\mathbf{p}_2,\mathbf{p}_3,\mathbf{p}_4) = \delta(\mathbf{p}+\mathbf{p}_2-\mathbf{p}_3-\mathbf{p}_4)\,\delta(\tilde{\varepsilon}_p+\tilde{\varepsilon}_{p_2}-\tilde{\varepsilon}_{p_3}-\tilde{\varepsilon}_{p_4}). \tag{2.19}$$

The factors like $(1+f_j)$ correspond to the addition of a boson in state j and those like f_j correspond to the removal of a boson from that state. $\mathbf{v}_c = (\hbar/m)\boldsymbol{\nabla}\theta$ is the velocity of the condensate, while $\varepsilon_c = \mu_c + (1/2)m\mathrm{v}_c^2$ is the local energy of the condensate. The quantity $\tilde{\varepsilon}_j = p_j^2/2m + U_{\mathrm{eff}}(\mathbf{r},t)$ is the local energy of a non-condensate atom in the state j, with the momentum $\mathbf{p}_j$. The effective potential felt by the non-condensate atoms, $U_{\mathrm{eff}}(\mathbf{r},t)$, is given by

$$U_{\mathrm{eff}}(\mathbf{r},t) = V_{\mathrm{trap}}(\mathbf{r},t) + 2g(n_c(\mathbf{r},t)+\tilde{n}(\mathbf{r},t)). \tag{2.20}$$

Note that there is a similar effective potential in Eq. (2.6), $U_c(\mathbf{r},t) = V_{\mathrm{trap}}(\mathbf{r},t) + gn_c(\mathbf{r},t) + 2g\tilde{n}(\mathbf{r},t)$ that only differs by a factor of 2 on the term involving the BEC density. The connections between the condensate and the non-condensate are these effective potentials involving each others' densities, as well as the $C_{12}[f,\Phi]$ integral in the QBE, and the source/sink term $R(\mathbf{r},t)$ in the GGPE.

2.3 Numerical Solution of the ZNG Model Equations

The ZNG model is used to simulate the behavior of a condensate/non–condensate system that is initially in thermal equilibrium and is subjected to a weak perturbation. In our system a condensate is formed in the racetrack potential in thermal equilibrium with a non–condensate modeled as an interacting classical gas at temperature T. The ZNG–model behavior of this system can be determined by evolving the system of coupled equations

consisting of the GGPE (Eq. (2.6))

$$i\hbar\frac{\partial}{\partial t}\Phi(\mathbf{r},t)=\left(\frac{-\hbar^2}{2m}\nabla^2+V_{\rm trap}(\mathbf{r},t)+gn_c(\mathbf{r},t)+2g\tilde{n}(\mathbf{r},t)-iR(\mathbf{r},t)\right)\Phi(\mathbf{r},t), \qquad (2.21)$$

and the QBE (Eq. (2.15))

$$\frac{\partial f}{\partial t}-\boldsymbol{\nabla}_r U_{\rm eff}\cdot\boldsymbol{\nabla}_p f+\frac{\mathbf{p}}{m}\cdot\boldsymbol{\nabla}_r f=C_{12}[f,\Phi]+C_{22}[f]. \qquad (2.22)$$

The essential quantities produced by these equations are the condensate wave function, $\Phi(\mathbf{r},t)$, which is the solution of the GGPE, and the non–condensate density, $\tilde{n}(\mathbf{r},t)$, which is obtained from the QBE by integration:

$$\tilde{n}(\mathbf{r},t)=\int\frac{d^3p}{(2\pi\hbar)^3}f(\mathbf{p},\mathbf{r},t). \qquad (2.23)$$

Starting from an initial thermal–equilibrium state $\Phi(\mathbf{r},t)$ and $\tilde{n}(\mathbf{r},t)$ are repeatedly evolved from the current time to the next time step.

In the simulations described in this work we ignore all condensate/non-condensate and non-condensate/non-condensate collisions so that the collision integrals $C_{12}[f,\Phi]$ and $C_{22}[f]$ in the QBE are neglected. These collisions can lead to the damping of excitations, and therefore may play a role in the creation and destruction of circulation states in the BEC. Their inclusion in future work is needed to investigate exactly how, if at all, they affect the ability to produce flow by stirring. Neglecting the collision integrals precludes any exchange of atoms between the condensate and non–condensate which implies that the term $R(\mathbf{r},t)$ in the GGPE will also be zero. Thus the equations to model the system evolution are reduced to the following form:

$$i\hbar\frac{\partial}{\partial t}\Phi(\mathbf{r},t)=\left(\frac{-\hbar^2}{2m}\nabla^2+V_{\rm trap}(\mathbf{r},t)+gn_c(\mathbf{r},t)+2g\tilde{n}(\mathbf{r},t)\right)\Phi(\mathbf{r},t) \qquad (2.24)$$

and

$$\frac{\partial f}{\partial t} - \boldsymbol{\nabla}_r U_{\rm eff} \cdot \boldsymbol{\nabla}_p f + \frac{\mathbf{p}}{m} \cdot \boldsymbol{\nabla}_r f = 0. \tag{2.25}$$

We first describe how the GGPE is evolved.

We use a split-step Crank-Nicholson (SSCN) algorithm to solve Eq. (2.24) [24]. The SSCN method propagates $\Phi(\mathbf{r},t)$ to $\Phi(\mathbf{r},t+\delta t)$ by separating the GGPE Hamiltonian into two parts (1) the kinetic energy term and (2) everything else:

$$\hat{H} = \frac{-\hbar^2}{2m}\nabla^2 + V_{\rm trap}(\mathbf{r},t) + g n_c(\mathbf{r},t) + 2g\tilde{n}(\mathbf{r},t) \equiv \hat{T} + \hat{V} \tag{2.26}$$

where $\hat{T} = (-\hbar^2/2m)\nabla^2$ is the kinetic energy operator. The condensate wave function is propagated one time step in this way

$$\begin{aligned} \Phi(\mathbf{r},t+\delta t) &= e^{-i\hat{H}\delta t/\hbar}\Phi(\mathbf{r},t) = e^{-i(\hat{T}+\hat{V})\delta t/\hbar}\Phi(\mathbf{r},t) \\ &\approx e^{-i\hat{T}\delta t/\hbar}e^{-i\hat{V}\delta t/\hbar}\Phi(\mathbf{r},t) \equiv e^{-i\hat{T}\delta t/\hbar}\Phi_{1/2}(\mathbf{r},t'=0) \end{aligned} \tag{2.27}$$

The last equation above shows the two steps performed to evolve Φ by one time step. The wave function is first multiplied by $e^{-i\hat{V}\delta t/\hbar}$ to get the function $\Phi_{1/2}(\mathbf{r},t'=0)$. This can be done at each space point.

The subsequent multiplication by $e^{-i\hat{T}\delta t/\hbar}$ is carried out equivalently by solving

$$i\hbar\frac{\partial\Phi_{1/2}(\mathbf{r},t')}{\partial t'} = \hat{T}\Phi_{1/2}(\mathbf{r},t') \tag{2.28}$$

with initial state $\Phi_{1/2}(\mathbf{r},t'=0)$. This equation is propagated for one time step, δt, by the Crank–Nicolson algorithm, and then we set $\Phi(\mathbf{r},t+\delta t) = \Phi_{1/2}(\mathbf{r},\delta t)$.

The QBE, Eq. (2.25), is evolved from time t to $t+\delta t$ by performing a Monte–Carlo simulation. This is carried out by using a set of "test particles" to sample the initial

single–particle distribution whose thermal–equilibrium form is given by [10]

$$f^0(\mathbf{p},\mathbf{r},t) = \frac{1}{e^{\beta\left[p^2/2m+U_0(\mathbf{r})-\mu_0\right]}-1} \tag{2.29}$$

where $\beta = 1/k_BT$ and $U_0(\mathbf{r}) = V_{\rm trap}(\mathbf{r}) + 2g(n_{c0}(\mathbf{r}) + \tilde{n}_0(\mathbf{r}))$ is the initial Hartree–Fock mean–field potential. The set of test particles is simply a list of $\tilde{N}_{tp}$ positions, $\mathbf{r}_i$, and velocities, $\mathbf{v}_i$ where $i = 1,\ldots,\tilde{N}_{tp}$, that sample $f(\mathbf{p},\mathbf{r},t)$ in phase space. The single–particle distribution function can thus be written as:

$$f(\mathbf{p},\mathbf{r},t) \approx \left(\frac{\tilde{N}}{\tilde{N}_{tp}}\right)(2\pi\hbar)^3 \sum_{i=1}^{\tilde{N}_{tp}} \delta(\mathbf{r}-\mathbf{r}_i(t))\delta(\mathbf{p}-\mathbf{p}_i(t)) \tag{2.30}$$

where $\tilde{N}_{tp}$ is the number of test particles and $\tilde{N}$ is the number of actual non–condensate particles. The factor $(\tilde{N}/\tilde{N}_{tp})$ is included so that the integral of f over all phase space will yield the total number of non–condensate atoms.

The initial test–particle set is generated so that the position and velocity statistics of the test particles matches the known thermal–equilibrium non–condensate density and Bose–Einstein speed distributions obtained from Eq. (2.29). The left panel of Fig. 2.2 shows the initial, thermal–equilibrium non–condensate density distribution along the radial direction computed from Eq. (2.8) (red curve) with that obtained from statistics gathered from the list of test particles (green curve). A similar comparison is shown in the right panel of the figure for the speed distributions.

The single–particle distribution is in general evolved from t to $t+\delta t$ in two steps. First their positions and momenta are updated according to Newton's laws of motion with the force given as the space gradient of $U_0(\mathbf{r})$. This accounts for the change in f due to the diffusion and force terms in the Boltzmann equation. Second, changes in f due to collisions

would also have to be accounted for in the full model, but again we are neglecting them in this work. The details of how these steps are carried out are described in Ref. [10].

The last step in the evolution procedure is to compute a new non-condensate density from the test-particle distribution. The non-condensate is found by assigning these test-particles (which do not fall on our computational grid) weights to nearby grid-points, according to how close they are, and then convolving this coarse-grain distribution with a 3D Gaussian to make a smooth density distribution at $t + \delta t$.

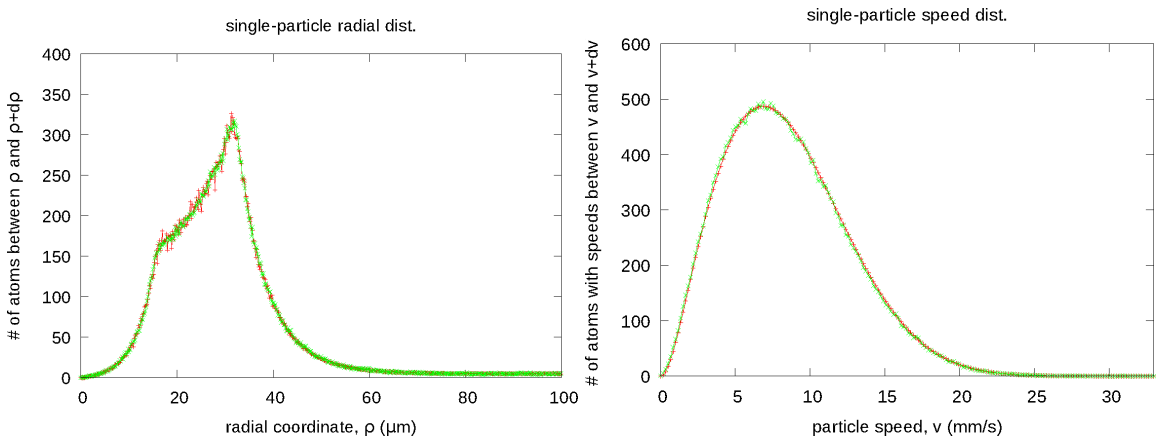

Figure 2.2: In the left panel is plotted the radial distribution of the initial state test-particles (green) alongside the distribution they should have according to the Bose-Einstein distribution, Eq. (2.33) (red). The right panel is the same, except the test-particles' speed distribution is shown instead.

Different initial thermal equilibrium states are needed for each different combination of racetrack length, L, and temperature, T. Because we assume a fixed total number of atoms in the sample, the higher the equilibrium temperature the fewer the number of atoms in the condensate and more in the non–condensate. At some critical temperature, T_c, there

are no atoms in the condensate. It can be shown that the number of atoms in the condensate, expressed as a fraction of the total number obeys the following law for $T \leq T_c$ [25]

$$\frac{N_c}{N_{total}} = 1 - \left(\frac{T}{T_c}\right)^{\alpha}. \tag{2.31}$$

Here N_c is the number of atoms in the BEC and α is a potential dependent parameter. For different racetrack lengths and a fixed total number of particles $N_{total} = 500,000$, calculation of the initial states of the system at different temperatures enables us to extract the values for T_c and α by fitting Eq. (2.31) to the ZNG numerical results. The data from these calculations are plotted alongside the fits in Fig. 2.3.

Note that T_c decreases as the racetrack length increases. This happens because longer racetracks afford a larger volume for the gas which increases the average interparticle spacing. Condensates begin to form when the matter wavelengths of the atoms (which lengthen as the atoms get colder) are comparable to the average interparticle spacing. Thus, colder atoms are needed to form condensates for longer racetracks.

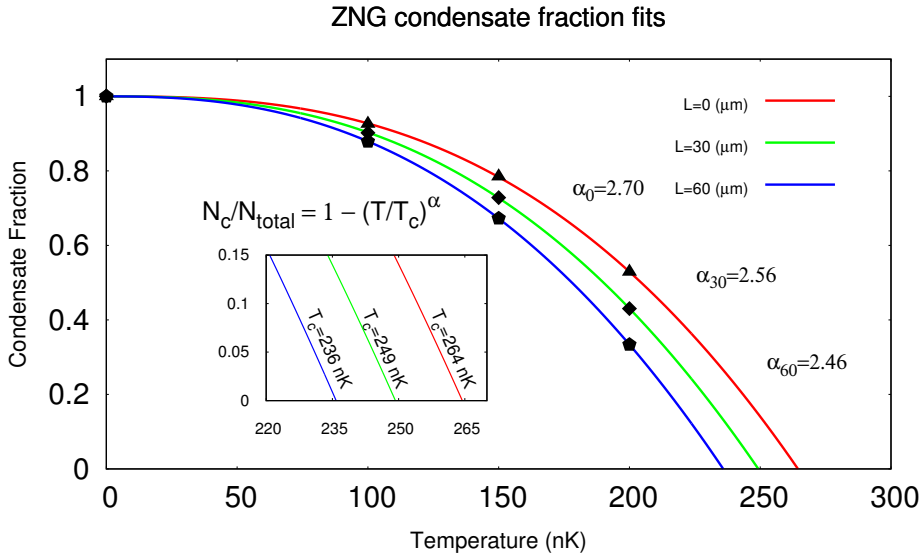

Figure 2.3: Thermal–equilibrium condensate fractions versus temperature for three different lengths of the racetrack potential, $L = 0, 30, 60\,\mu$m. The points correspond to condensate fractions obtained from the ZNG model at temperatures $T = 100, 150, 200$ nK and the solid curves are fits through these curves to Eq. (2.31). The inset shows the fits where they intersect the temperature axis, which is the critical temperature, T_c, at which condensation begins.

The ZNG initial state consists of a thermal–equilibrium condensate wave function and non–condensate density which are self–consistent simultaneous solutions of the time–independent GGPE and the thermal–equilibrium single–particle distribution function. The time–independent GGPE (found by letting $\Phi(\mathbf{r},t) = e^{-i\mu_0 t/\hbar}\Phi_0(\mathbf{r})$ in Eq. (2.24)) is given by

$$\mu_0\Phi_0(\mathbf{r}) = \left(\frac{-\hbar^2}{2m}\nabla^2 + V_{\rm trap}(\mathbf{r}) + g|\Phi_0(\mathbf{r})|^2\Phi_0(\mathbf{r}) + 2g\tilde{n}_0(\mathbf{r})\right)\Phi_0(\mathbf{r}), \qquad (2.32)$$

and the thermal–equilibrium single–particle distribution function (from Eq. (2.29)) is written as

$$f^0(\mathbf{p},\mathbf{r}) = \frac{1}{e^{\beta\left[p^2/2m+V_{\rm trap}(\mathbf{r})+2g(|\Phi_0(\mathbf{r})|^2+\tilde{n}_0(\mathbf{r}))-\mu_0\right]}-1}. \tag{2.33}$$

These two equations are coupled because the time–independent GGPE contains the non–condensate density, $\tilde{n}_0(\mathbf{r})$, which also appears along with $\Phi_0(\mathbf{r})$ in $f^0(\mathbf{p},\mathbf{r})$. The non–condensate density is obtained from the single–particle distribution function as

$$\tilde{n}_0(\mathbf{r}) = \int \frac{d^3p}{(2\pi\hbar)^3} f^0(\mathbf{p},\mathbf{r}). \tag{2.34}$$

These equations are solved simultaneously subject to the condition that the number of condensate atoms, N_c, and the number of non–condensate atoms, $\tilde{N}$, add up to the fixed total number of atoms, N_{total}.

The procedure for performing this self–consistent calculation is to solve the time–independent GGPE, Eq. (2.32), assuming that all the atoms are in the condensate so that the non–condensate density, $\tilde{n}_0(\mathbf{r})$, is zero. This solution is normalized so that the total number of condensate atoms equals N_{total}. This yields a zeroth–order guess for the condensate wave function, $\Phi_0^{(0)}(\mathbf{r})$, and chemical potential, $\mu_0^{(0)}$. Now, still assuming that $\tilde{n}_0(\mathbf{r})$ is zero, $f^0(\mathbf{p},\mathbf{r})$, is constructed and a zeroth guess at the non–condensate density, $\tilde{n}^{(0)}(\mathbf{r})$, is computed using Eq. (2.34). With this new non–condensate density, the first guess at the number of non–condensate atoms (zeroth guess was zero) is computed by

$$\tilde{N}^{(1)} = \int d^3r \tilde{n}^{(0)}(\mathbf{r}) \tag{2.35}$$

and a new number of condensate atoms is computed by $N_c^{(1)} = N_{total} - \tilde{N}^{(1)}$. Using the new guess at the non–condensate density and number of condensate atoms, we go back to the

GGPE and solve this again to obtain a new guess at the condensate wavefunction which is now normalized to the new value of N_c. This process, where the condensate wavefunctions and the non–condensate densities are alternately computed, and the number of condensate and non–condensate atoms alternately updated, is continued for a prescribed number of steps.

Convergence is reached if these two numbers stabilize as the iterative process continues. Figure 2.4 displays example density profiles for the condensate and non–condensate for the case where $L = 0\,\mu$m and $T = 200$ nK. The BEC sits lowest in the trap, and since the non-condensate feels a repulsion from the BEC based on its density it sits in an effective double-well potential, and concentrates along the inside and outside of the ring BEC.

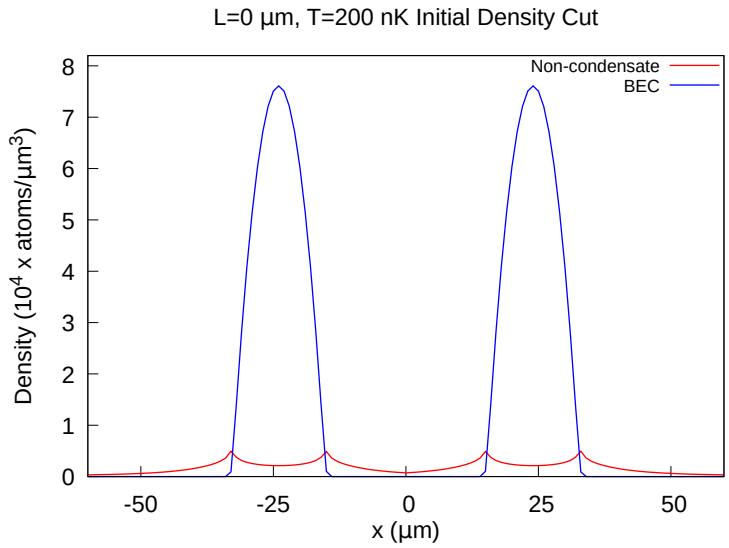

Figure 2.4: Density profile cuts for the condensate and non–condensate in thermal equilibrium at temperature $T = 200$ nK and confined in the racetrack potential with $L = 0\,\mu$m (ring BEC). Here, the density along a cut straight through a ring case in the $z = 0$ plane is shown.

CHAPTER 3

DESCRIPTION OF PRESENT STUDY

We conducted a systematic study of the smooth flow produced by stirring a BEC confined in a racetrack atom circuit at non-zero temperature. In this chapter we first describe the racetrack potential confining the BEC, and the potential used to model the stirring barrier in Sec. 3.1. Next we describe the different simulations that are the focus of this thesis in Sec. 3.2. Following that, in Sec. 3.3 we discuss the quantities that we calculate for every simulation.

3.1 System Characteristics

When an atom is subjected to a laser field, it can be treated as a two-level system with a ground state of energy E_g and an excited state of energy E_e. The laser frequency, ω_L, is such that the energy of the photons is close to the transition energy of the two levels, i.e., $\hbar\omega_L \approx E_e - E_g \equiv \hbar\omega_{eg}$. The difference in the frequencies $\omega_L - \omega_{eg}$ is known as the laser detuning. When $\omega_L > \omega_{eg}$, we say that the laser is *blue-detuned*. When $\omega_L < \omega_{eg}$, we say that the laser is *red-detuned*. In this laser field, it can be shown using perturbation theory [8] that the spatially dependent shift in the ground state energy is

$$\Delta E_g(\mathbf{r}) = \Big[\frac{\hbar(\omega_L - \omega_{eg})}{(\omega_L - \omega_{eg})^2 + (\Gamma_e/2)^2}\Big]\Omega_{\mathrm{R}}^2(\mathbf{r}). \tag{3.1}$$

The symbol Γ_e^{-1} represents the lifetime of the excited state, and Ω_{R} is known as the Rabi frequency, which is the frequency at which the laser field photons stimulate absorption to,

and subsequent emission from, the excited state. Ω_R^2 is proportional to the intensity of the laser field, which gives Eq. (3.1) its spatial dependence.

Since the shift in the ground state energy is spatially dependent, the center of mass of the atom feels an effective potential. If the laser is blue-detuned, ΔE_g is positive and the atom will move to where it can find the lowest value of Ω_R, away from high intensity regions of the laser field. If the laser is red-detuned, ΔE_g is negative and the atom will move to where it can find the highest value of Ω_R, towards high intensity regions of the laser field. So blue-detuned lasers push atoms away, red-detuned lasers attract them. Experimentalists take advantage of this behaviour to realize all optical atom-trapping. Using laser light enables the use of magnetic fields solely for the purpose of tuning the interactions via Feshbach resonances [8], giving a greater degree of freedom in what experiments can be performed. It also gives more flexibility in what potentials can be created for the trapped ultra-cold gases, which means that theorists can consider a wider range of potentials that are also practical.

The potential that we consider in this thesis can be broken into three parts:

$$V_{\text{trap}}(x,y,z,t) = V_{\text{lightsheet}}(z) + V_{\text{racetrack}}(x,y) + V_{\text{barrier}}(x,y,t) \tag{3.2}$$

The system is strongly confined in the vertical z-direction by a harmonic term

$$V_{\text{lightsheet}}(z) = \frac{1}{2} m\omega_z^2 z^2, \tag{3.3}$$

where $\omega_z = 2\pi \cdot 320$ Hz is taken as the vertical trapping frequency. This confinement could be achieved by either a sheet of red-detuned light or two sheets of blue-detuned light with a space in the middle.

The racetrack potential is then imposed in the horizontal xy-plane. It consists of a channel with two semi-circular end-caps characterized by inner and outer radii, connected by straightaways. We model this potential by writing the $V_{\text{racetrack}}$ term as

$$V_{\text{racetrack}}(x,y) = V_{\text{rt}}\left\{\frac{1}{2}\left[\tanh\left(\frac{\rho(x,y)-R_o}{\sigma}\right)+\tanh\left(\frac{R_i-\rho(x,y)}{\sigma}\right)\right] + \tanh\left(\frac{R_o-R_i}{2\sigma}\right)\right\}. \tag{3.4}$$

The inner and outer radii of the semi-circular endcaps are controlled by the parameters $R_i = 12\,\mu$m and $R_o = 36\,\mu$m respectively, $\sigma = 24\,\mu$m determines how steep the channel walls are, $V_{\text{rt}} = 1132.4$ nK controls the overall depth of the channel, and the shape of the racetrack path is determined by

$$\rho(x,y) = \begin{cases} \sqrt{(x-L/2)^2+y^2} & x > L/2 \\ \sqrt{(x+L/2)^2+y^2} & x < -L/2 \\ |y| & |x| \le L/2\,. \end{cases} \tag{3.5}$$

The length of the racetrack potential straightaway is denoted by L. The racetrack potential is depicted in Fig. 3.1. The actual width, measured in the $z = 0$ plane using the density that is 10% of the maximum in that plane as a cutoff, is about $10\,\mu$m compared to $R_o - R_i = 24\,\mu$m. The physical inner radius of the cloud is measured from the results of our simulations, by the same criterion as the width, to be $W_i \approx 17\,\mu$m and the outer radius $W_o \approx 27\,\mu$m.

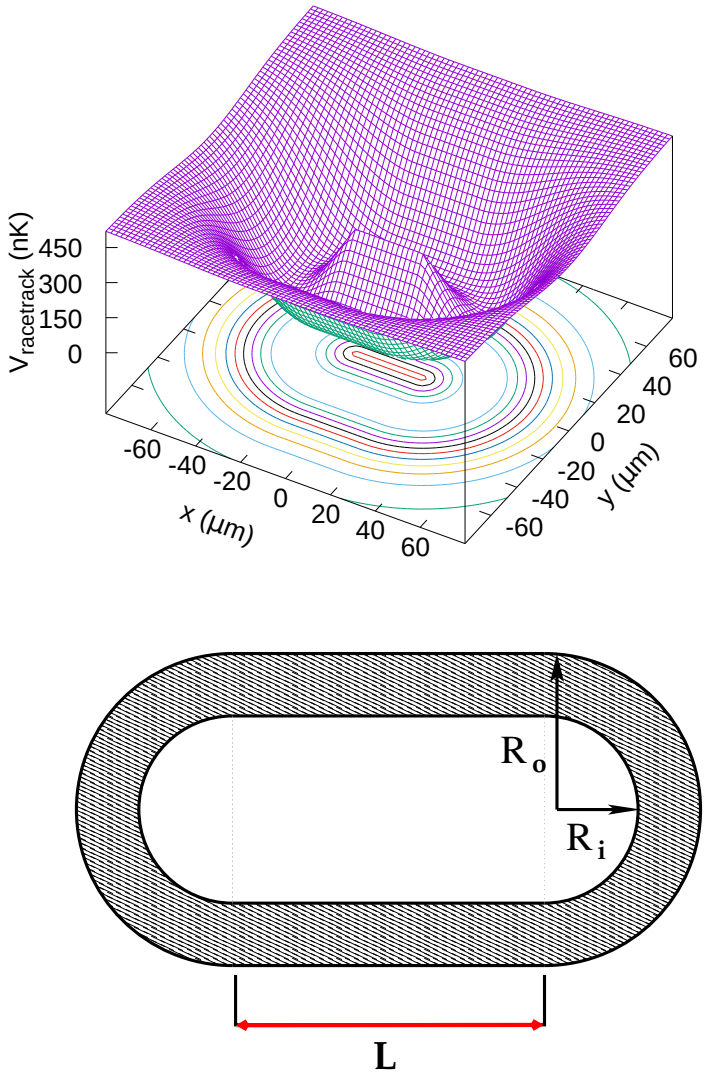

Figure 3.1: Above: A plot of $V_{\text{racetrack}}(x,y)$. Below: A schematic representation of the shape the BEC takes in the trap and the dimensions of the racetrack.

To stir the gas we add a barrier term $V_{\text{barrier}}(x,y,t)$ to the static potential made up of Eqs. (3.3) and (3.4). In order to express the shape of this barrier clearly in mathematical

terms, we introduce a step-up and step-down function:

$$V_{\text{up}}(x, x_{\text{up}}, a) = (1/2)\Big[1 + \tanh\Big(a(x - x_{\text{up}})\Big)\Big] \tag{3.6}$$

$$V_{\text{down}}(x, x_{\text{down}}, a) = (1/2)\Big[1 + \tanh\Big(a(x_{\text{down}} - x)\Big)\Big] \tag{3.7}$$

The step up function is plotted in Fig. 3.2, and the step down function is $V_{\text{down}} = 1 - V_{\text{up}}$, which reflects V_{up} across a horizontal axis through $V(x) = 1/2$. This is just a mathematical function and is made into a potential energy term by multiplication of a factor with units of energy.

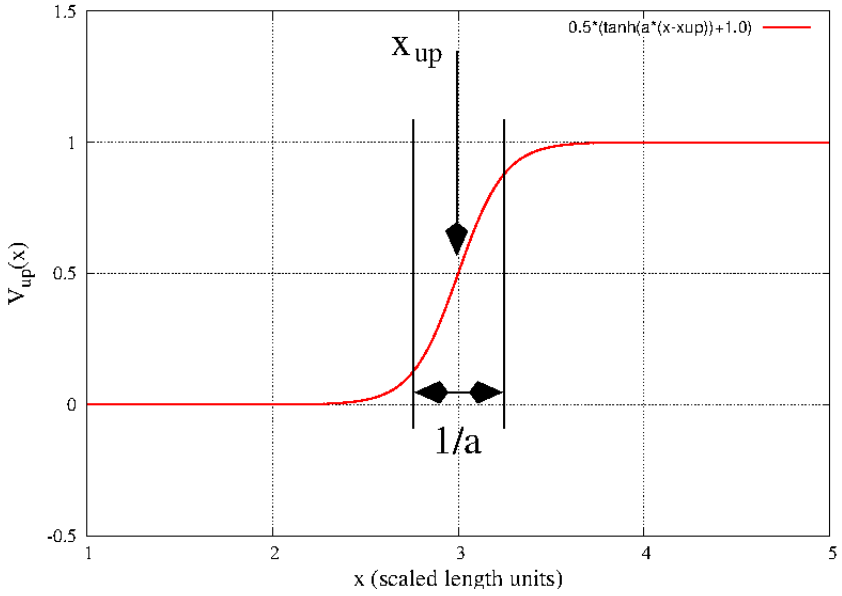

Figure 3.2: A plot of Eq. (3.6). The function steps up around the position x_{up}, and the parameter a^{-1} controls the width of the step. In the first two two terms of Eq. (3.4), $a^{-1} = \sigma$, and in the third $a^{-1} = 2\sigma$.

By multiplying Eqs. (3.6) and (3.7) together, we can make a bump since they are both positive in some region where they overlap, and outside that region they are both zero.

To make our barrier we use two such products, one in the x direction and one in the y. The barrier has the form:

$$\begin{aligned} V_{\text{barrier}}(x,y,t) = & V_p(t)\Big\{ V_{\text{up}}\big(x_p(x,y),(-L_p/2),\sigma\big)\times \\ & V_{\text{down}}\big(x_p(x,y),(L_p/2),\sigma\big)\times \\ & V_{\text{up}}\big(y_p(x,y),(-W_p/2),\sigma\big)\times \\ & V_{\text{down}}\big(y_p(x,y),(W_p/2),\sigma\big)\Big\} \end{aligned} \tag{3.8}$$

where $L_p = 48.0\ \mu$m and $W_p = 3.0\ \mu$m control the length and width of the barrier, respectively. The position and orientation of the barrier are determined by the barrier coordinates (x_p, y_p)

$$x_p(x,y,x_c,y_c,\theta_p) = \quad (x-x_c)\cos(\theta_p) + (y-y_c)\sin(\theta_p) \tag{3.9}$$

$$y_p(x,y,x_c,y_c,\theta_p) = -(x-x_c)\sin(\theta_p) + (y-y_c)\cos(\theta_p). \tag{3.10}$$

These equations are parameterized through the coordinates of the barrier's center (x_c, y_c) and angle of orientation θ_p by the arclength along the racetrack s, which is itself parameterized by time with the equation:

$$s(t) = \left(\frac{s_0 + v_p t}{s_{total}} - \left\lfloor \frac{s_0 + v_p t}{s_{total}} \right\rfloor \right) s_{total}, \tag{3.11}$$

where $s_0 = L + \pi R/2$, $s_{total} = 2L + 2\pi R$, $R = \frac{1}{2}(R_o + R_i) = 24\,\mu$m, and $\lfloor x \rfloor$ is the floor function which rounds a real number input down to the nearest integer. The constant speed at which the barrier moves is given by v_p, however we also express it in a convenient measure referred to as TR, which stands for "total revolutions". A given number of TR means that the barrier moves at the speed at which it would complete that number of revolutions in 4

seconds in the $L = 0$ case. So TR is related to v_p in the following way for the particular racetrack parameters in our simulations:

$$v_p = \left(\frac{\pi R}{2}\right)(\text{TR})\ \text{s}^{-1} \tag{3.12}$$

$$\approx 37.7\,(\text{TR})\ \mu\text{m s}^{-1} \tag{3.13}$$

The parametric equations that determine the position of the center of the barrier are:

$$x_c(s) = \begin{cases} s - \frac{L}{2} & 0 \le s < L \\ \frac{L}{2} + R\sin(\frac{s-L}{R}) & L \le s < \frac{s_{total}}{2} \\ \frac{3L}{2} + \pi R - s & \frac{s_{total}}{2} \le s < s_{total} - \pi R \\ -\frac{L}{2} - R\sin(\frac{s-s_{total}+\pi R}{R}) & s_{total} - \pi R \le s < s_{total} \end{cases} \tag{3.14}$$

$$y_c(s) = \begin{cases} -R & 0 \le s < L \\ -R\cos(\frac{s-L}{R}) & L \le s < \frac{s_{total}}{2} \\ R & \frac{s_{total}}{2} \le s < s_{total} - \pi R \\ R\cos(\frac{s-s_{total}+\pi R}{R}) & s_{total} - \pi R \le s < s_{total}. \end{cases} \tag{3.15}$$

The barrier starts at $s_0 = L + \pi R/2$ and is made to stay oriented with its long direction of length L_p perpendicular to the racetrack. This is achieved by rotating the

coordinates $\big((x-x_c),(y-y_c)\big)$ by the angle $\theta_p(s)$ whose parameterization is given by:

$$\theta_p(s) = \begin{cases} -\frac{\pi}{2} & 0 \le s < L \\ -\frac{\pi}{2} + \frac{s-L}{R} & L \le s < \frac{s_{total}}{2} \\ \frac{\pi}{2} & \frac{s_{total}}{2} \le s < s_{total} - \pi R \\ \frac{\pi}{2} + \frac{s-s_{total}+\pi R}{R} & s_{total} - \pi R \le s < s_{total} \end{cases} \tag{3.16}$$

and the result of this is Eqs. (3.9) and (3.10) used in V_{barrier}.

During the stirring phase of the simulation, the energy height of the barrier is ramped up linearly from zero to a maximum value, $V_{p\max}$, in 500 ms, held constant for another 500 ms, and then ramped down linearly over another 500 ms. The energy height of the barrier is controlled by $V_p(t)$ in eq. (3.8). This parameter follows what will be referred to as the *stirring schedule*, and is given by

$$V_p(t) = \begin{cases} [t/(500\text{ ms})]V_{p\max} & 0 \le t < 500\text{ ms} \\ V_{p\max} & 500\text{ ms} \le t < 1000\text{ ms} \\ (3-[t/(500\text{ ms})])V_{p\max} & 1000\text{ ms} \le t < 1500\text{ ms} \\ 0 & 1500\text{ ms} \le t \le 2000\text{ ms} \end{cases} \tag{3.17}$$

where $V_{p\max}$ is the highest energy height of the barrier during the simulation. This is shown in Fig. 3.3. Note that the slopes of the on and off ramps are $+V_{p\max}/(500\,\text{ms})$ and $-V_{p\max}/(500\,\text{ms})$, respectively. Thus, the different values of $V_{p\max}$ correspond to different rates of change depending linearly on the given value.

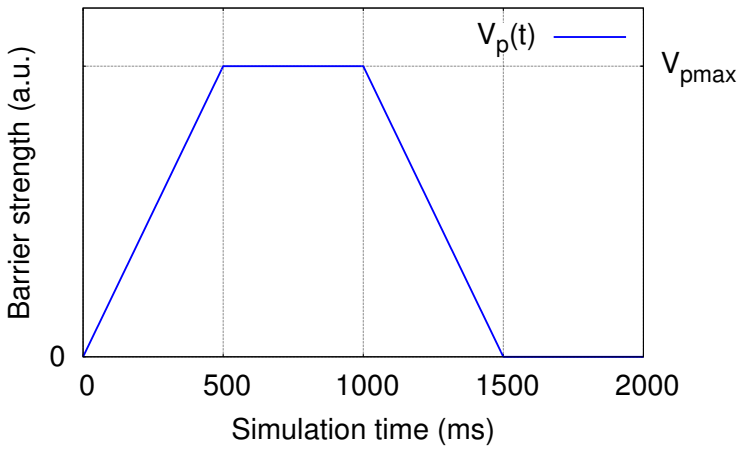

Figure 3.3: A generic plot of the stirring schedule for the ZNG simulations.

3.2 Parameter Space of Simulations

In order to study the effects of temperature on the production of quantized circulation by stirring we simulated the stirring of our racetrack BEC with a rectangular barrier under different conditions. The parameters that we varied were the racetrack length, L, the stirring speed, v_p, the initial temperature, T, and the maximum barrier height, $V_{p\max}$. Approximately 2700 simulations were performed. We also added ≈ 900 zero-temperature simulations from Ref. [11] to analyze our results.

Chemical Potential and Sound Speed Values

$\{L, T\}$	μ (nK)	c (μm/s)
{00, 000}	58.1	4,610
{00, 100}	56.0	4,520
{00, 150}	53.3	4,410
{00, 200}	46.8	4,130
{30, 000}	50.0	4,270
{30, 100}	47.6	4,170
{30, 150}	44.7	4,040
{30, 200}	38.0	3,720
{60, 000}	44.9	4,050
{60, 100}	42.1	3,920
{60, 150}	39.0	3,770
{60, 200}	31.9	3,410

Table 3.1: A table of chemical potentials and speeds of sound calculated for the various initial states. These quantities decrease with both increasing length and temperature due to resulting decreases in BEC density (for a fixed total number of atoms).

A natural energy scale for the condensate is its chemical potential, μ. This chemical potential is the work required to add one more atom to the condensate. The chemical

potential can be related to the speed of sound, c, in the gas by [8]

$$c = \sqrt{\frac{\mu}{m}} = \sqrt{\frac{g|\Phi_{\max}|^2}{m}}. \tag{3.18}$$

The second equality is valid in the “Thomas-Fermi" limit [26] where the condensate atom interaction energy is much greater than the kinetic energy. Values of μ and c for different cases are presented in Table 3.1 for reference.

The parameter ranges contained in our set of simulations included three different temperatures $T = 100$ nK, 150 nK, 200 nK; three different racetrack lengths $L = 0\,\mu$m, $30\,\mu$m, $60\,\mu$m; four different stirring speeds $v_p = 113.1\,\mu$m/s, $226.2\,\mu$m/s, $339.3\,\mu$m/s, and $452.4\,\mu$m/s. For a given set of values (L, v_p, T), simulations were performed for 76 values of $V_{p\max}$ which varied from one half the chemical potential, μ, up to twice μ in steps of 0.02μ. This parameter space is summarized in Table 3.2. A given set of simulations is identified by a name such as `L_30_TR_09_T_100`, which would mean $L = 30\,\mu$m, TR$= 9$, and $T = 100$ nK.

Simulation Parameter Space

T (nK) $\downarrow$ v_p (μm/s) $\rightarrow$	113.1	226.2	339.3	452.4
0 (GPE)	$\{V_{p\max}\}$	$\{V_{p\max}\}$	$\{V_{p\max}\}$	$\{V_{p\max}\}$
100 (ZNG)	$\{V_{p\max}\}$	$\{V_{p\max}\}$	$\{V_{p\max}\}$	$\{V_{p\max}\}$
150 (ZNG)	$\{V_{p\max}\}$	$\{V_{p\max}\}$	$\{V_{p\max}\}$	$\{V_{p\max}\}$
200 (ZNG)	$\{V_{p\max}\}$	$\{V_{p\max}\}$	$\{V_{p\max}\}$	$\{V_{p\max}\}$

Table 3.2: $\{V_{p\max}\} = \{0.50, 0.52, ..., 2.00\}\mu$ is the set of all different $V_{p\max}$ cases for each speed TR and temperature T. μ is the chemical potential of the initial state of the system, the values for different cases of which are presented in Table 3.1. Furthermore, simulations were done with these parameters for racetrack lengths $L \in \{0, 30, 60\}$ μm. Simulations were not done for cases where $V_{p\max} > 999.9$, but this only represents 2% of this parameter space.

3.3 Quantities Output in ZNG Simulations

In each simulation of the non–zero temperature systematic study, Eqs. (2.24) and (2.25) were evolved from $t = 0$ to $t = 2000$ ms using 35,000 equal sized time steps. This corresponds to a step-size $\delta t = 5.71 \times 10^{-2}$ ms. This step-size was chosen to be similar to the step-size of the GPE solver code used in Ref. [11]. The step-size needs to be small enough to reduce numerical errors from the split-step Crank-Nicolson algorithm

used in both the GPE and GGPE solvers. The step-size used in Ref. [11] was known to be small enough based on experience using the GPE solver code in previous projects, see Refs. [27–30].

The condensate wavefunction, $\Phi(\mathbf{r},t)$, and the non–condensate density, $\tilde{n}(\mathbf{r},t)$, were saved to disk at 100 equally spaced time intervals during the total evolution time. These times were at $t_k = k\delta t,\ k = 0,\ldots,100$, and we will refer to t_k as the k-th frame time. At the end of each simulation these quantities occupied approximately 100 Gigabytes of storage even in binary format. Since the systematic study comprised approximately 2700 simulations, saving all of the condensate wave functions and non–condensate densities in non-binary would have required about 270 Terabytes (TB) of storage space.

All of the runs were performed on the `raritan.nist.gov` supercomputer at the National Institute of Standards and Technology (NIST), and we did not have access to that much storage on the NIST machine. Thus we decided that, for each simulation, we would perform further processing on these wave functions and non–condensate densities to extract important quantities and then delete the wave functions and non–condensate densities in order to save space. This procedure also significantly reduced the amount of time required to download the results to local storage at Georgia Southern University.

The quantities saved at each frame time (i.e., $t = t_k$) included (1) the two–dimensional grid of points (x_i, y_j) where $i = 0,\ldots,N_x$ and $j = 0,\ldots,N_y$ in the $z = 0$ plane; (2) the real part of condensate wave function on the 2D grid in the $z = 0$ plane, $\mathfrak{Re}(\Phi(x,y,0,t_k))$; (3) the imaginary part of the condensate wave function on the 2D grid in the $z = 0$ plane, $\mathfrak{Im}(\Phi(x,y,0,t_k))$; (4) the non–condensate density on the 2D grid in the $z = 0$ plane, $\tilde{n}(x,y,0,t_k)$;

(5) the condensate optical density (defined in the next paragraph), $\rho_{c,opt}(x,y,t_k)$, on the 2D grid in the $z=0$ plane; (6) the non–condensate optical density, $\tilde{\rho}_{opt}(x,y,t_k)$, on the 2D grid in the $z=0$ plane; (7) the trap potential, $V_{\rm trap}(x,y,0,t_k)$ on the 2D grid in the $z=0$ plane, (8) the effective potential, which is the trap potential plus $2g$ times the total density and denoted as $U_{\rm eff}(x,y,0,t_k)$ on the 2D grid in the $z=0$ plane, and finally (9) the condensate phase, $\theta(x,y,0,t_k)$, on the 2D grid in the $z=0$ plane.

The optical density in a plane at a given point in the plane is the total number of atoms per unit plane area contained in a narrow tube perpendicular to the given plane and which passes through the given point. Thus, the condensate optical density in the $z=0$ plane at point (x,y) in the plane and at time t is

$$\rho_{c,opt}(x,y,t) \equiv \int_{-\infty}^{\infty} |\Phi(x,y,z,t)|^2 \, dz. \tag{3.19}$$

Thus, $\rho_{c,opt}(x,y,t)dxdy$ is the total number of atoms in the tube of cross section $dxdy$ that passes through the point (x,y). This definition can be applied to the non–condensate density in a similar way. The total optical density distribution (sum of condensate and non–condensate optical densities) in a plane can be compared directly with experimental images of the sample of atoms. The atomic sample absorbs the laser light used to make the image, and thus casts a shadow which can be detected with a charge–coupled device.

Figure 3.4 shows examples of some of the quantities described above for a representative simulation. In this simulation the racetrack length is $L = 30\,\mu$m, the barrier stir speed is TR$=6$ which translates into $v_p = 226\,\mu$m/s, and the temperature was $T = 150$ nK. The figure shows the condensate density, non–condensate density and condensate phase in

the $z = 0$ plane at four different times during the simulation. For all ZNG simulations the total simulation time was 2000 milliseconds. The simulation time for the GPE simulations performed in the previous study [11] was 4000 milliseconds. This was in part to see if the circulation states excited would persist for a long time (they did) and in part to leave time free to use those states for applications after they were created. Since the excited states were seen to be persistent with the long run time, we shortened it using the ZNG for efficiency.

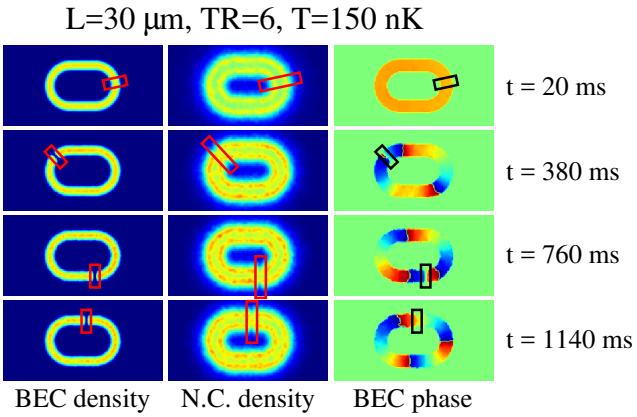

Figure 3.4: Examples of the condensate density, non–condensate density and phase in the $z = 0$ plane at four different times during a representative simulation. Simulation characteristics are racetrack length $L = 30\,\mu$m, barrier stir speed $v_p = 226\,\mu$m/s, and temperature $T = 150$ nK.

CHAPTER 4

ANALYSIS OF THE RESULTS

In this chapter we present the results of our analysis of the data collected in our systematic study of flow production, in order to understand the effects of temperature, T, racetrack length, L, stir speed, v_p, and barrier strength, $V_{p\max}$, on the amount of flow produced by stirring. First we describe the way we reduced and formatted the data collected in the systematic flow production study described in Ch. 3. We then present our analysis of this data to describe the general features of flow produced by stirring.

We found that the flow produced by stirring presented two features that appeared in every simulation. The first is that, for fixed T, L, and v_p, non–zero flow appeared for barrier strengths where $V_{p\max}$ was above a critical value, which we denote as $V_{p\max,c}$. The second feature is that, as $V_{p\max}$ increases, the flow produced levels off and oscillates around an average value, w_{avg}.

4.1 Reduction of the Data

A key quantity computed in this study is the phase distribution in the $z = 0$ plane, $\theta(x, y, 0, t_{\text{final}})$, of the BEC after the stirring schedule has taken place. Since the velocity distribution of the BEC is proportional to the gradient of the phase, the signature of macroscopic circulation is a non-zero integer phase winding, i.e. how many times the value of the phase cycles through 2π going around the racetrack. It is essential to know what overall

circulation state is obtained in the BEC after stirring the gas if one wants to use atomtronic circuits such as these for applications or experiments.

We want to be able to predict the circulation for any given set of the parameters $(L, \mathrm{TR}, T, V_{p\mathrm{max}})$. Such a prediction would be valid within reasonable bounds of the parameters, the bounds being other quantities of interest. For example one would get inherently different results, likely turbulent, if the gas is stirred above the speed of sound, or at least above some other critical speed.

We applied three levels of reduction to our entire set of simulation results. In the first level, we reduced the data in each simulation by computing the condensate wavefunction phase distribution in the $z = 0$ plane at the final time of the simulation. Such a result can be displayed as a two-dimensional false-color image where the color at a point represents the value of the wavefunction phase at that point within the range $[-\pi, \pi)$. Figure 4.1 shows an array of such plots for simulations where $L = 30\,\mu$m, TR$= 6$ ($v_p = 226.2\,\mu$m/s), and $T = 150$ nK. Each phase distribution plot within this array is labeled with the value of $V_{p\mathrm{max}}$ used in the associated simulation in units of the chemical potential, μ, of the initial condensate. The full set of these figures is included in Appendix B.

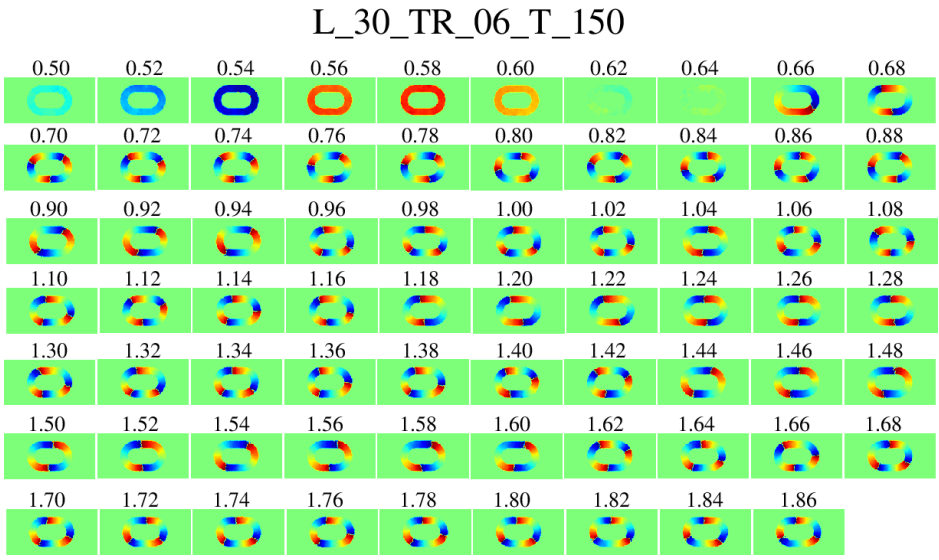

Figure 4.1: Final phase distributions for simulations where the length is $L = 30\,\mu$m, the stir speed is TR=6, and the temperature is $T = 150$ nK. Each small picture is a false-color plot of the phase distribution at the end of a simulation, $\theta(x, y, 0, t_{\text{final}})$, for a particular value of $V_{p\max}$. The value of $V_{p\max}$ is given above each picture in units of μ. The color scale represents the phase from $-\pi$ to π, going from blue to red. The winding numbers w are best found by counting the number of yellow bands (in grey scale this corresponds to the number of brightest bands) across the channel.

In the second level of reduction, we determined the winding numbers produced by stirring in each simulation by counting the number of 2π cycles of phase accumulated in traversing the mid-line of the racetrack. The winding numbers are plotted on the vertical axis against $V_{p\max}$ in units of the chemical potential μ on the horizontal axis for each case. The data sets are plotted alongside cases with the same length L and stirring speed TR but different temperatures T in order to elucidate the role of the non-zero temperature.

An example of this is shown in Fig. 4.2. The final winding numbers were counted by hand as well as by numerical integration of Eq. (1.6). Computing this integral numerically and combining it with the result $\mathscr{C} = 2\pi\hbar w/m$ allows us to determine $w(t_{\text{final}})$. The full set of plots like the example in Fig. 4.2 is shown in Appendix C.

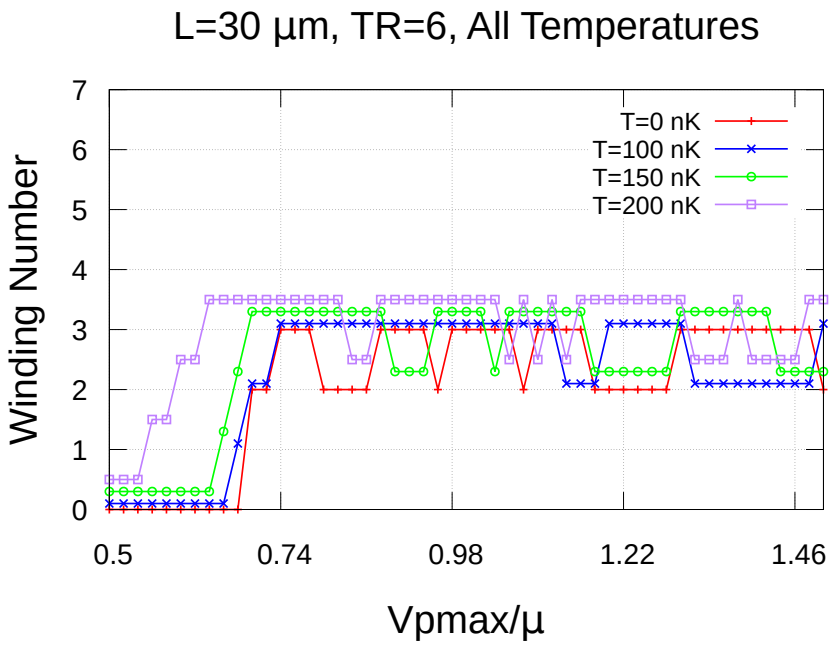

Figure 4.2: $w(t_{\text{final}})$ plotted versus the parameter $V_{p\max}$ scaled by the chemical potential of the initial state of the BEC, μ. Values of μ for different cases are found in Table 3.1. These curves are for the $L = 30\,\mu$m length racetrack, stirring speed TR$=6$, for all temperatures considered. The different T cases have been offset slightly for clarity, and should be floored to the next lowest integer. The curve for $T = 150$ nK is extracted from the final phase distributions shown in Fig. 4.1.

The third level of data reduction is a "heat map" flow plot where the maximum flows (for all values of $V_{p\max}$) are arranged in a 2×2 array displaying all cases of different L and TR for fixed T. For each (L, TR, T) case, we found the highest winding number, $w_{\max}$, achieved across all $V_{p\max}$ cases. This was done in order to see what determines an upper-bound for the amount of flow able to be produced for a given case, and specifically to see if temperature plays a role in determining that bound. An example of the results for $w_{\max}$ for the cases with $T = 150$ nK is shown in Fig. 4.3, while all of the results are found in Appendix D.

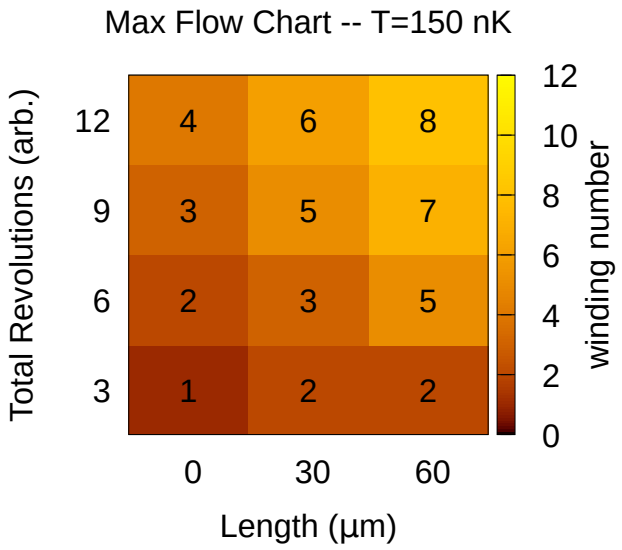

Figure 4.3: The maximum winding number out of all the $V_{p\max}$ for different length and stirring speed cases at $T = 150$ nK is plotted as a heat-map, with the values of $w_{\max}(L, \mathrm{TR})$ shown in the squares.

4.2 Analysis of Results

Looking at the results described in Sec. 4.1 for all of the cases, we can make several observations. First it is possible to produce flow (excite states of quantized circulation) in all length, stirring speed, and temperature cases considered in this project for many values of $V_{p\max}$. This is evidenced by the non-zero winding numbers present in the final phase distributions at the end of the simulations for a range of $V_{p\max}$, for every (L, TR, T) shown in Appendix B.

For all of the simulations, where the parameters (L, TR, T) are fixed, there are two features common to the phase plots. The first feature is the existence of a critical max barrier strength, $V_{p\max,c}$, below which no circulation of the BEC is present at the end of the simulation. This is illustrated in panel a) of Fig. 4.4 for $L = 0$ and TR$= 6$, where, at all temperatures, there is a relatively rapid onset of flow as $V_{p\max}$ increases.

The second feature that all of the cases share is that as $V_{p\max}$ continues to increase, the winding number $w(t_{\mathrm{final}})$ rapidly rises from zero to an average value w_{avg}, about which the winding number fluctuates, usually by no more than ± 1. This feature is displayed in panels b) and c) of Fig. 4.4. In 4 out of 48 cases of fixed (L, TR, T), the final flow is around this average value even at $V_{p\max} = 0.5\mu$, i.e. the smallest value of $V_{p\max}$ for which simulations were performed. Since there are many more cases where there is a clear value of $V_{p\max,c}$, or at it is at least clear that the data is trending to such a value, we feel it is safe to assert that this critical max barrier strength is a general feature. There is also a physical reason for thinking this way. Since the circulation is quantized, and since having

$V_{p\max} = 0$ would clearly produce no flow, there has to be some minimum value above zero in order for stirring to produce flow.

These features are displayed in Fig. 4.4. For a fixed (L, TR), it seems that as T increases, $V_{p\max,c}$ generally decreases. This is strictly the case at $L = 0\,\mu$m, however in the non-zero length cases it is somewhat more complicated. In some of these cases, $V_{p\max,c}$ first increases as the temperature is raised but when $T = 200$ nK, it is lower than the $T = 0$ nK situation. While it seems like this applies for the higher speed cases $\mathrm{TR} = 9, 12$, it is not possible to say this definitively since there is flow excited for all $V_{p\max}$ considered.

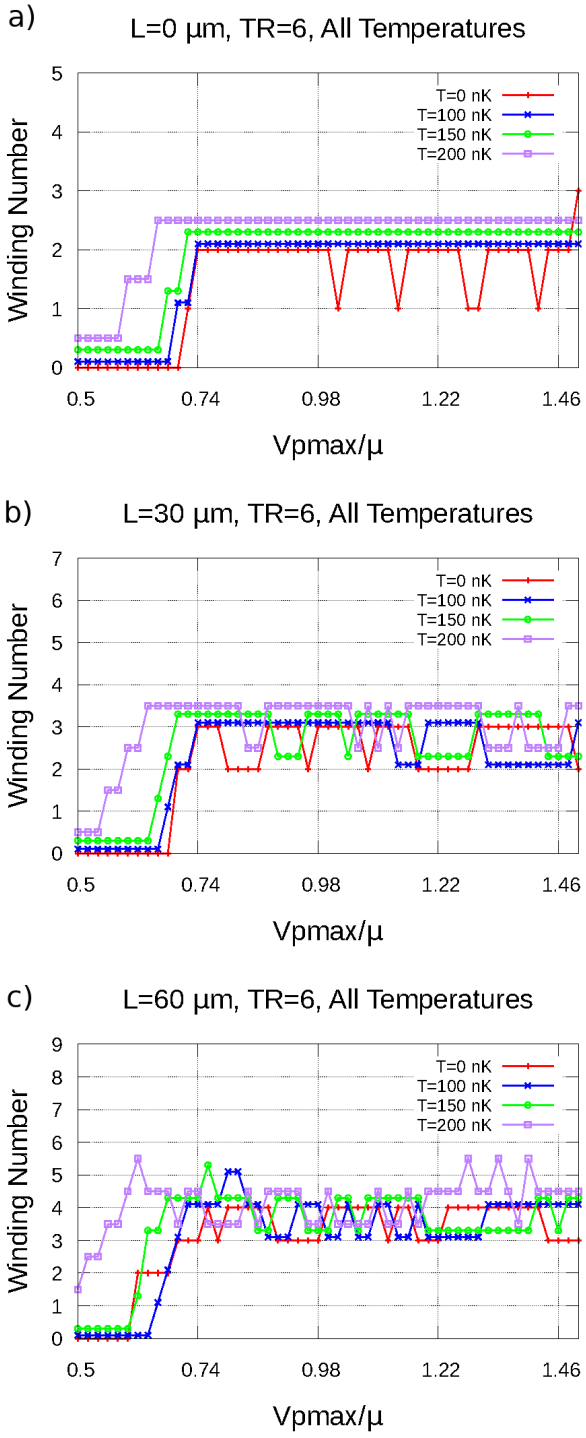

Figure 4.4: Three examples of the flow as a function of $V_{p\max}$. The critical max barrier strengths for the $T = 0$ nK case are $V_{p\max,c} = 0.72, 0.70, 0.62$ and the average flow are $w_{\text{avg}} = 2, 3, 4$, for panels a), b), and c) respectively.

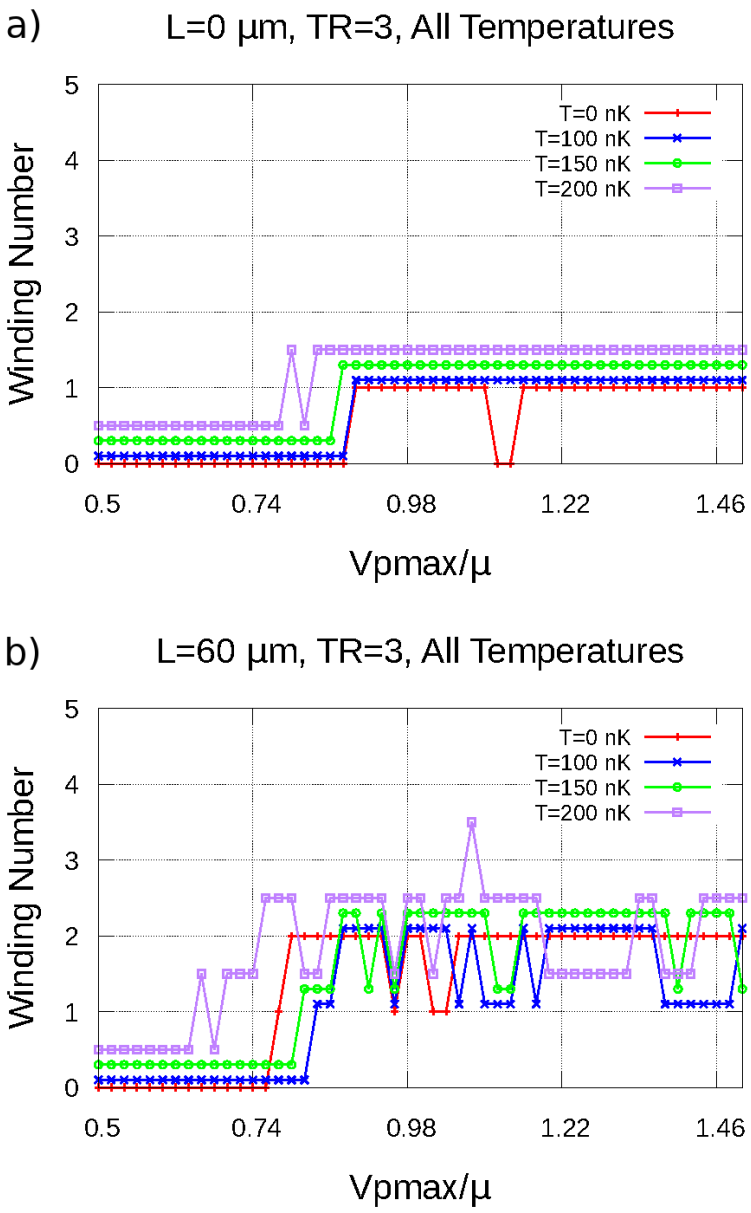

Figure 4.5: The decreasing trend of $V_{p\max,c}$ as T increases is shown. In the $L = 0\,\mu$m case it is strictly true, while in the $L = 60\,\mu$m case the story seems more complicated, but at $T = 200$ nK $V_{p\max,c}$ is still lower than at $T = 0$ nK.

Another trend we see is that for a fixed (L, T), increasing the stirring speed TR

leads to both a lower $V_{p\max,c}$ and a higher w_{avg}. This is illustrated in Fig. 4.6. Fixing the speed and temperature while increasing the length has a similar but weaker effect. One of the major effects of increasing the length is that it leads to more fluctuations about w_{avg}, and this is also illustrated in Fig. 4.4. The fluctuations are usually ± 1, but on occasion ± 2. From the charts looking at the maximum flow obtained, it is clear that temperature has little effect on how much flow can be produced, and the racetrack length and stirring speed are seen to be more significant determiners of flow. The charts for the two extremes, $T = 0$ nK and $T = 200$ nK are shown in Fig. 4.7. Comparing them to each other, and to Fig. 4.3, the lack of major dependence on T is evident.

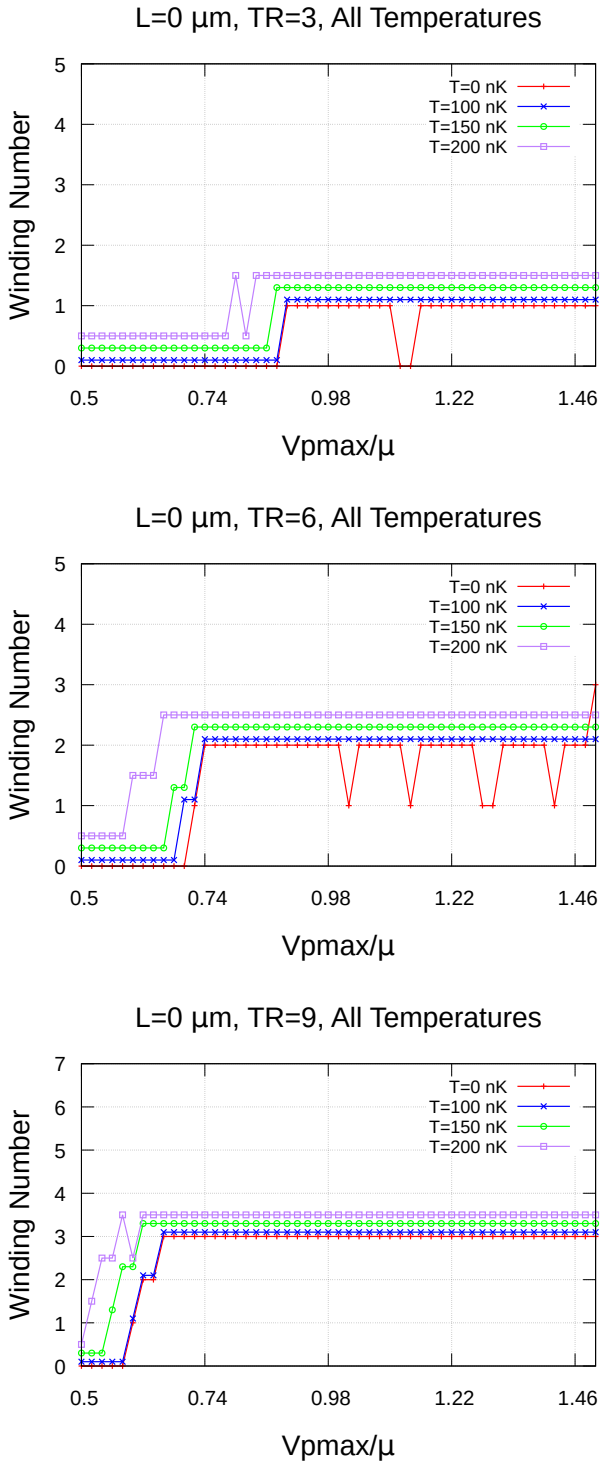

Figure 4.6: The trend of decreasing $V_{p\max,c}$ and increasing w_{avg} with increasing stirring speed is shown, fixing the length and temperature.

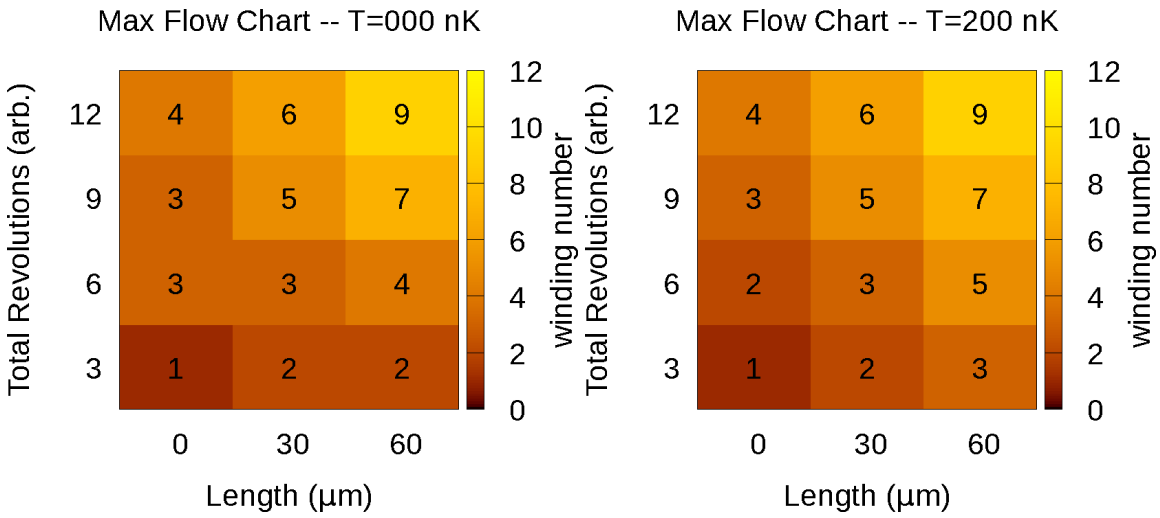

Figure 4.7: Heat-maps showing the maximum winding numbers for cases at $T = 0$ and $T = 200$ nK, the two temperature extremes considered in this thesis. Increasing speed at $L = 60\,\mu$m, or increasing length at TR $= 12$ has the most effect on the maximum amount of flow excited out of all $V_{p\max}$ cases. These charts show almost identical results, as does the $T = 150$ nK case shown in Fig. 4.3 and the $T = 100$ nK case shown in Appendix D.

4.3 Primary Impact of Non-zero Temperature

Based on the final phase distributions of the BEC wavefunction, it is clear that the results at non-zero temperature are qualitatively similar to those at zero temperature. However, for a fixed (L, TR), temperature quantitatively affects the value of the final circulation obtained for a given $V_{p\max}/\mu$, while not eliminating the ability to excite the circulation states in general by stirring. It also lowers the $V_{p\max}/\mu$ needed to produce any flow at all, especially at temperatures closer to T_c where Fig. 2.3 shows there is between about

30-55% of the atoms in the BEC. This shows that a major effect of temperature is to reduce the density of the BEC, for a fixed total number of atoms.

The non-condensate does exhibit some motion, which technically affects the motion of the BEC, however, even when the number of non-condensate atoms makes up half of the total, they are spread out over a larger volume and consequently have a much lower density, as shown in Fig. 2.4, so the mean-field effect of the non-condensate is rather weak. The relationship of lowering the overall BEC density by raising the temperature to the creation of circulation is best studied in the barrier region, since previous research has suggested that the local dynamics in the barrier is what is important for the excitation of the circulation states [20, 29, 31].

4.4 Summary of Results

We can summarize our main results as follows. The final flow produced in all of our simulations share two qualitative features: 1) the existence of a critical maximum barrier strength below which no flow is present by the end of the simulation and 2) at the onset, the amount of flow rises rapidly and levels off as $V_{p\max}$ is increased (for a fixed length, stirring speed, and temperature) and then fluctuates around an average value, w_{avg}. Within our parameter space the general trends of these two features can be summarized as:

- Trends for $V_{p\max,c}$
  - For fixed (L, TR), with increasing temperature $V_{p\max,c}$ gets lower.

  - For fixed (L,T), with increasing stirring speed $V_{p\max,c}$ gets lower.
  - For fixed (TR,T), with increasing racetrack length $V_{p\max,c}$ gets slightly lower (small effect).

- Trends for w_{avg}
  - For fixed (L,TR), increasing temperature has little effect on w_{avg}.
  - For fixed (L,T), with increasing stirring speed w_{avg} gets higher.
  - For fixed (TR,T), with increasing racetrack length w_{avg} gets higher.

Raising the temperature has little bearing on the maximum amount of flow that can be excited for a given (L,TR), the pair of which are more important for the determination of the maximum. It is clear from Figs. 4.3 and 4.7 that temperature has little effect on the $w_{\max}$ achievable. While this does not give us much of an understanding as to how the length of the racetrack or the speed of the stirring determine this maximum, we see that there is a general trend of increasing $w_{\max}$ as the length and speed increases.

Longer racetracks increase the ability for a barrier moving at a given speed to create more units of circulation. In the $L = 0\,\mu$m case, the barrier speeds are just below the speed of a ^{23}Na atom moving around a ring with a radius of $R = (R_o + R_i)/2 = 24\,\mu$m with units of angular momentum. For example, the $\mathrm{TR} = 3$ case corresponds to a stirring speed of about $113\,\mu\mathrm{m}\,s^{-1}$ while a classical ^{23}Na atom moving in a circular orbit of radius R with a single unit of orbital angular momentum has a speed of $v_1 = (1)\hbar/(MR) \approx 115\,\mu\mathrm{m}\,s^{-1}$.

The results obtained in this systematic study show that the flow produced by stir-

ring depends on the temperature, racetrack length, stirring speed, and maximum barrier height. We must note that our results and analysis excludes the collisions between the non-condensate and condensate atoms, which may or may not have a significant effect on the production of flow (particularly at temperatures where a significant portion of the system is non-condensate, such as at $T = 200$ nK). It also does not provide a detailed picture of how flow is created during the stirring phase of the simulation. We investigate this last question in the next chapter.

CHAPTER 5

INVESTIGATION OF THE MECHANISM OF FLOW PRODUCTION BY STIRRING AT ZERO TEMPERATURE

In this chapter, we attempt to understand the mechanism by which states of quantized circulation are excited by stirring in the racetrack BEC. Based on a comparison of the results of the ZNG simulations and the GPE simulations, the only major difference is the first $V_{p\max}/\mu$ at which a non-zero circulation is present by the end of the simulation, for a fixed (L, TR). This leads us to believe that the basic mechanism for the excitation of these states is the same at non-zero temperatures as it is at $T = 0$, if maybe slightly modified by the non-condensate. Since the results of the ZNG simulations are qualitatively similar to those of the GPE, we focus for now on flow production at $T = 0$ nK. First we will discuss a 1D model obtained from the full 3D GPE, and how the solutions of this 1D-GPE compare to the solutions of the 3D case. Analysis of the 1D model results will provide a simple signature of the onset of flow. Then we will analyze the behavior of the 3D condensate during the stirring schedule for a representative case study where the simulation has been carried out on a finer timescale than the simulations in the systematic study.

5.1 1-Dimensional Model

In order to model the BEC as a 1-dimensional system we consider the $L = 0\,\mu$m case, the ring. The starting point is the time-dependent 3D-GPE,

$$i\hbar\frac{\partial}{\partial t}\Phi(\mathbf{r},t) = \left(\frac{-\hbar^2}{2m}\nabla^2 + V_{\text{trap}}(\mathbf{r},t) + g_{3\text{D}}n_c(\mathbf{r},t)\right)\Phi(\mathbf{r},t). \tag{5.1}$$

In cylindrical coordinates, the trapping potential is

$$V_{\text{trap}}(\mathbf{r},t) = \frac{1}{2}m\omega_z^2 z^2 + \frac{1}{2}m\omega_\rho^2(\rho-\rho_0)^2 + U(\vartheta,t), \tag{5.2}$$

where ρ is the radial coordinate, ϑ is the azimuthal coordinate, and z the vertical coordinate. We write Eq. (5.1) in cylindrical coordinates and separate the wavefunction into three independent functions $\Phi(\rho,\vartheta,z,t) = F(\rho)Z(z)\Theta(\vartheta,t)$. Here $Z(z)$ is the ground state wavefunction of the vertical potential $m\omega_z^2 z^2/2$ and $F(\rho)$ is the ground state of the radial potential $\omega_\rho^2(\rho-\rho_0)^2/2$. Using the normalization condition on $F(\rho)$ and $Z(z)$ we can integrate out the radial and vertical coordinates and arrive at a 1D equation for the azimuthal wavefunction

$$i\hbar\frac{\partial}{\partial t}\Theta(\vartheta,t) = \left(\frac{-\hbar^2}{2mR^2}\frac{\partial}{\partial\vartheta^2} + U(\vartheta,t) + g_{1\text{D}}|\Theta(\vartheta,t)|^2\right)\Theta(\vartheta,t), \tag{5.3}$$

where R is the radius of the 1D ring, $U(\vartheta,t)$ is the potential in the azimuthal direction, and $g_{1\text{D}}$ is a re-normalized interaction constant which is related to the interaction constant in the 3D case by

$$g_{1\text{D}} = g_{3\text{D}}\int_0^\infty |F(\rho)|^4\rho d\rho\int_{-\infty}^\infty |Z(z)|^4 dz. \tag{5.4}$$

In order to get an idea of what the 1D model should look like if it is to capture qualitative features of the 3D case, the value of the 3D wavefunction was obtained at points

along the mid-line of the racetrack. This is the parametric path described by Eqs. (3.14) and (3.15). Our GPE solver outputs the wavefunction on a Cartesian grid, and these points rarely coincide with mid-line track points. Therefore, the mid-line track was discretized and the value of the wavefunction at points on the mid-line was found with a bilinear interpolation scheme using the values of the wavefunction at the nearest grid points in the $z = 0$ plane. This was done for a case-study with $L = 30\,\mu$m, TR$= 9$, and $V_{p\max} = 1.14\mu$, described in Sec. 5.2. This case study uses time steps of 0.4 ms. This is a finer timescale compared to the 40 ms time-steps used in the GPE systematic study in Ref. [11]. A finer timescale is required because the characteristic timescale for dynamics of the condensate wavefunction is fixed by the chemical potential as $\hbar/\mu$, which is typically on the order of a half millisecond in our systems. The results of this data-mining are shown in Fig. 5.1, while the solutions of Eq. (5.3) are shown in Fig. 5.2.

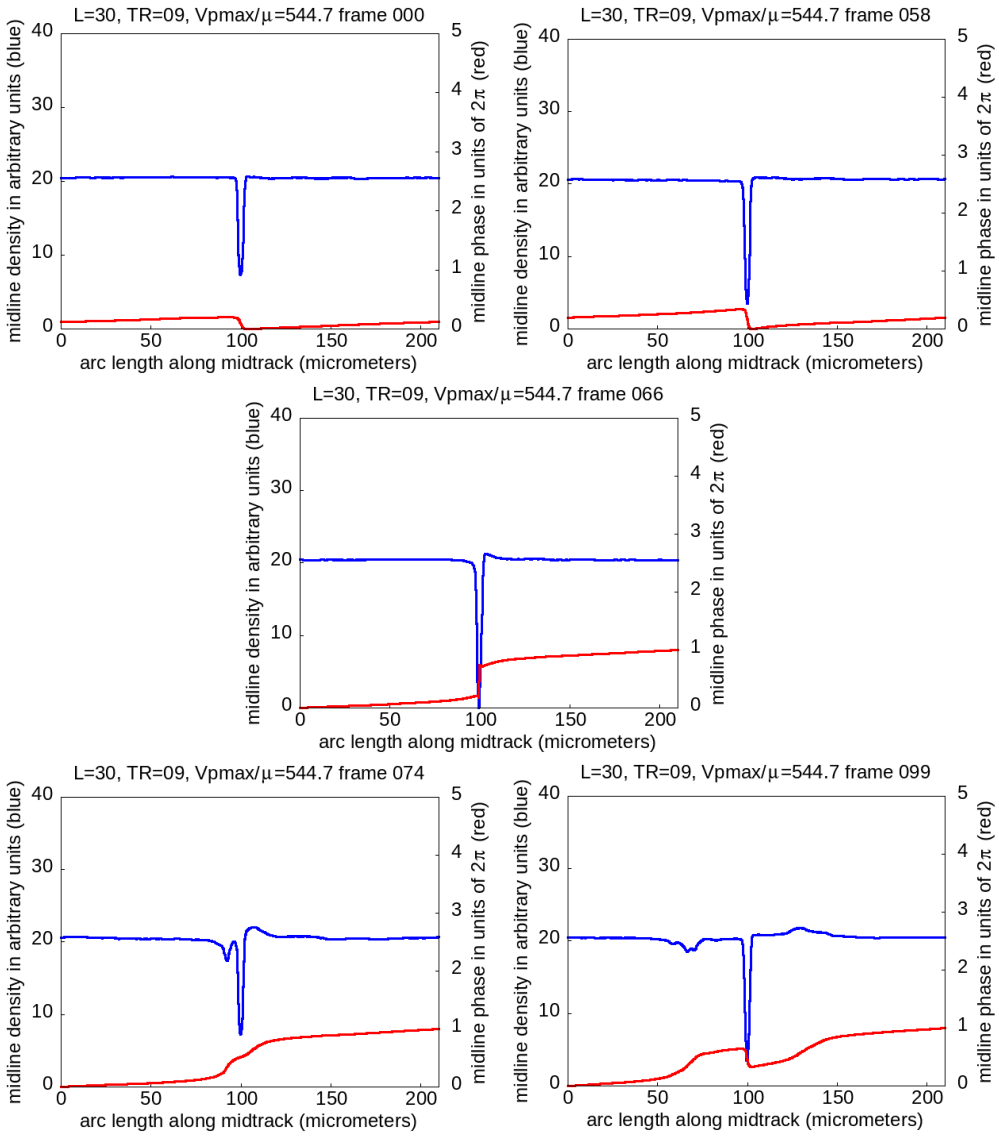

Figure 5.1: A series of density/phase plots of data mined from the 3D wavefunctions during the stirring phase of the simulation where $L = 30\mu$m, TR$= 9$, and $V_{p\max} = 1.14\mu$. The density is shown in blue curves while the phase is shown in red curves along the mid-line of the racetrack. The left vertical axis is for the density and the right vertical axis is for the phase in units of 2π. The onset of flow is signified by the appearance of a 2π change in phase around the racetrack mid-line.

As the barrier strength increases in Fig. 5.1, the density of the BEC has a notch develop in the barrier region, while a phase gradient builds up across the barrier. When the density notch reaches the bottom, this coincides with the appearance of a 2π phase winding around the racetrack. After this, the notch fills back in a bit as excitations are spawned off traveling in both directions away from the barrier.

This behaviour is also seen in the 1D model. Solutions are shown in Fig. 5.2. The density of the BEC has a notch develop in the barrier region as the barrier is raised, while a phase gradient builds up across the barrier, just as in the 3D case. When the density notch touches the bottom, a 2π winding in the phase is excited. This 1D case has a barrier width that is considerably thicker than that of the 3D case shown in Fig. 5.1, which leads to a wider density depression in the barrier region. Similar 1D simulations with a narrow barrier show identical behaviour. The key point is that in both the 3D and 1D cases, when the density notches touch bottom it coincides with the sudden onset of flow.

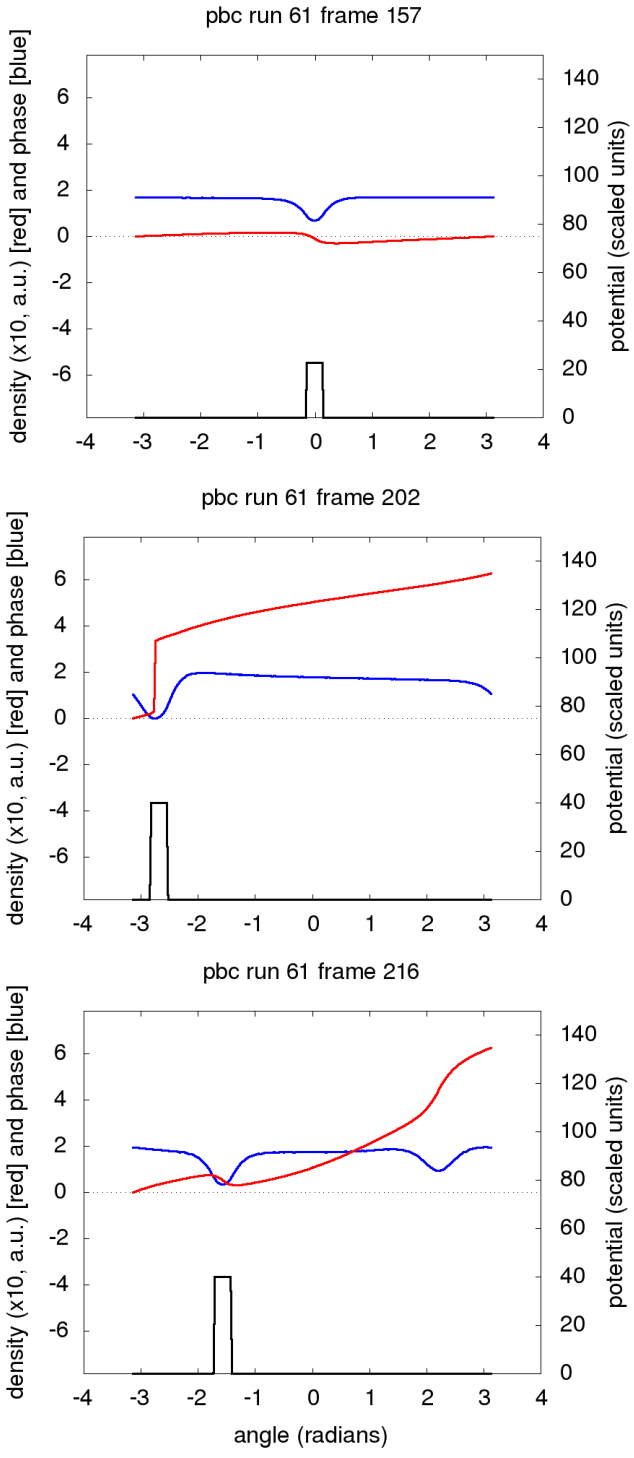

Figure 5.2: Density (blue, top curve in upper-left frame) and phase (red, bottom curve in upper-left frame) calculated from the 1D model, Eq. (5.3).

5.2 Case-Study of Stirring

While the 1D model does not match the 3D quantitatively since the 3D case has more degrees of freedom for the BEC, we see that there is a qualitative correspondence. This correspondence is that the density depression in the barrier region reaches zero and then there is a state of circulation present. We now look at a single case-study with $L = 30\,\mu$m, TR$= 9$, and $V_{p\max} = 1.14\mu$. For context, the final flow $w(t_{\text{final}})$ is pointed out for this particular case in Fig. 5.3.

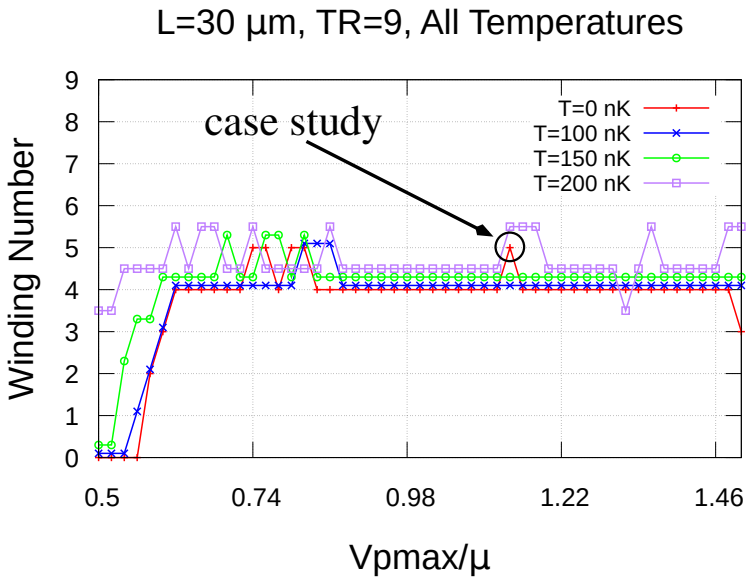

Figure 5.3: The case study we are considering, $L = 30\,\mu$m, TR$= 9$, and $V_{p\max} = 1.14\mu$, is pointed out above. It is one of the few cases in this set where $w(t_{\text{final}}) = 5$.

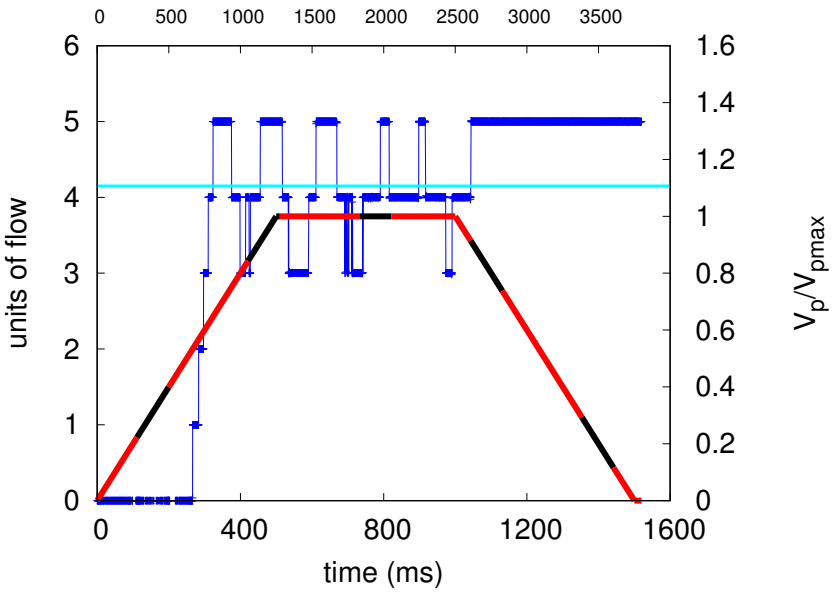

Figure 5.4: The winding number $w(t)$ (dark blue scatterplot) versus time during the stirring. The red/black curve shows the barrier height (in units of $V_{p\max}$). The red color represents the barrier moving along racetrack endcaps while black indicates the straight parts. The cyan line is the speed of the stirrer in units of the flow speed. The duration of each frame is 0.4 ms. The axis at the top of the figure represents the simulation time in frame numbers.

Much insight is gained by monitoring the dynamics of the circulation, $w(t)$, on a fine time scale during the stirring. These dynamics are shown in Fig. 5.4 where $w(t)$ is plotted (blue curve) along with the time–dependent value of the barrier strength, $V_p(t)/V_{p\max}$, (red and black curve). The red portion of the curve denotes an interval where the barrier is moving along the curved endcaps of the racetrack while in the black portion the barrier is moving along the straightaways. The flat cyan line is the stirring speed

$v_p(\mathrm{TR}=9) = 339\,\mu\mathrm{m}\ s^{-1}$ divided by $v_{\mathrm{circ}}(1) = \frac{(h/m)}{2L+2\pi R}$, which is the speed of a unit of circulation around the racetrack line given by Eqs. (3.14) and (3.15) assuming a constant phase gradient.

The behavior of the circulation can be understood as follows. At early times as the barrier height is ramping up, the circulation is zero. Above some critical barrier height, a unit of circulation is created. This is followed in quick succession by more units of circulation being added. This process stops when enough units of circulation are present so that the speed of the flow becomes larger than the speed of the stirring.

After this point the circulation oscillates up and down around the flow speed nearest the speed of the barrier. We also note that the circulation is affected when the barrier transitions from a straight section of the racetrack to a curved section, or vice versa. These transitions are signified as transitions on the barrier–height curve in Fig. 5.4 from black to red, or red to black, respectively. Above a certain barrier height, transitioning from straight to curved sections of the racetrack coincides with a drop of one unit of circulation. Transitioning from curved to straight sections of the racetrack coincides with the circulation increasing by one unit. In fact, the curved–to–straight transition just after the barrier begins to ramp down seems to be the reason for the final increase in circulation.

Further insight into the process of how the initial units of flow are generated is gained by looking at the velocity distribution in the vicinity of the barrier. As the barrier lowers the density locally while it is swept along the racetrack, it creates a back-flow (a negative phase gradient across the barrier region). The back-flow at early stages in its development is shown in the left panel of Fig. 5.5. The velocity of the BEC is practically

zero in the bulk, while it moves faster in the barrier region. Furthermore, it is faster at the edges of the barrier region than in the middle. This happens because the edges of the barrier create a higher potential when added to the bare trapping potential and lowers the density more than in the center. It can be thought of as putting two sticks down at the edge, and dragging them along the inside and outside edges of the BEC.

Since the barrier is on a straightaway, the velocity distribution across the barrier region is more or less symmetric. As the density is lowered more and more in the barrier region (slowly), the back-flow velocity increases until a point when it exceeds a critical value. The back-flow at the outer edge just before exceeding a critical value is also shown in the right panel of Fig. 5.5. The barrier is now moving around the left endcap of the racetrack. When going around an endcap, the BEC flows around the outer edge faster and the velocity profile across the barrier is no longer symmetric and increases toward the outer edge. The back-flow will therefore exceed a critical value at the outer edge first.

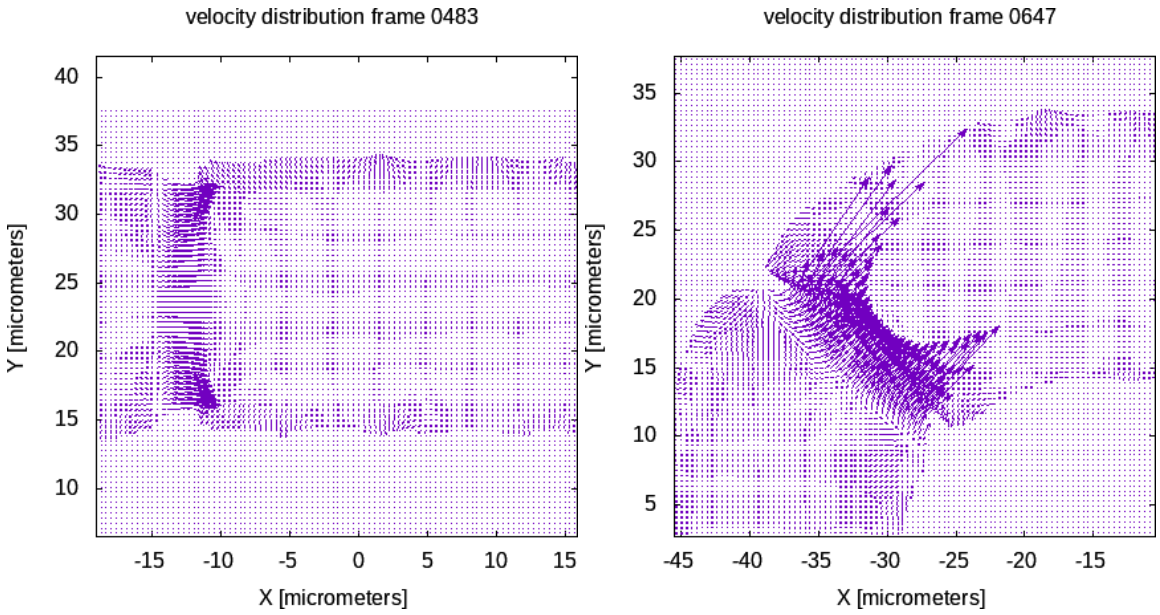

Figure 5.5: The velocity distribution in the $z = 0$ plane. The vectors have been scaled for clarity, and are intended to show where the BEC is moving the fastest. For reference, the center of the racetrack is at $(x, y) = (0, 0)\,\mu$m. Left: The barrier is moving to the left and is on a straightaway section of the racetrack, as the back-flow builds up. Right: The barrier is on the left endcap of the racetrack, and the back-flow is just about to exceed a critical velocity and spawn a vortex.

What happens after exceeding a critical velocity is that a vortex is spawned at the outer edge of the barrier region, shown in Fig. 5.6. It has the same handedness as the direction of stirring (if we stir CCW, the vortex is CCW). Since the density is low in the barrier region, as shown in Fig. 5.7, the vortex is able to slide through to the interior of the racetrack.

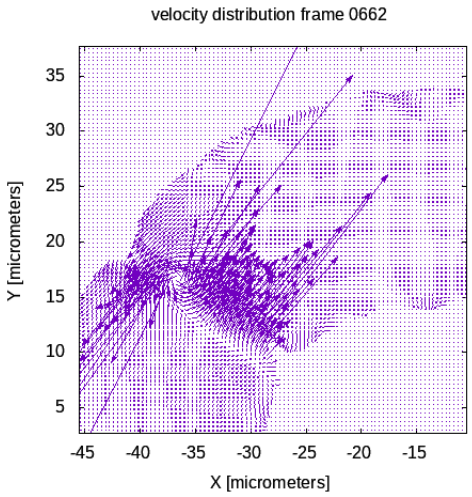

Figure 5.6: The first vortex sliding through. The vectors on the inside edge pointing up and to the right while the vectors on the outside edge pointing down and to the left indicate that this is a CCW vortex.

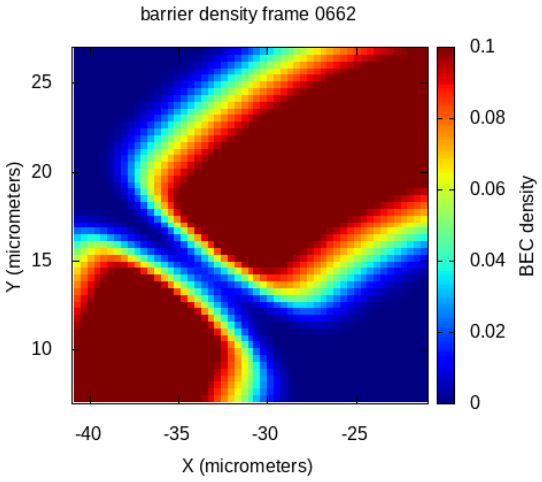

Figure 5.7: A plot of the BEC density in the $z = 0$ plane, around the barrier region at the same time as in Fig. 5.6. The density in the barrier region is about $1/10$ its value in the bulk.

When the vortex crosses through the barrier, any integration path for the circulation, Eq. (1.7), that encloses it will have a 2π phase winding around it. The 1D model corresponds to such a line going around the middle of the BEC in the $L = 0\,\mu$m case. The point at which the vortex is dead-center in the barrier region corresponds to the point in the 1D model and the 3D mid-track data-mining where the density scrapes bottom, since a vortex constitutes a zero in the wavefunction and any path that encloses it will have a non-zero circulation. Right after the vortex passes through, the direction of the flow through the barrier changes briefly. The velocity and phase distributions directly after the vortex has passed through are shown in Fig. 5.8.

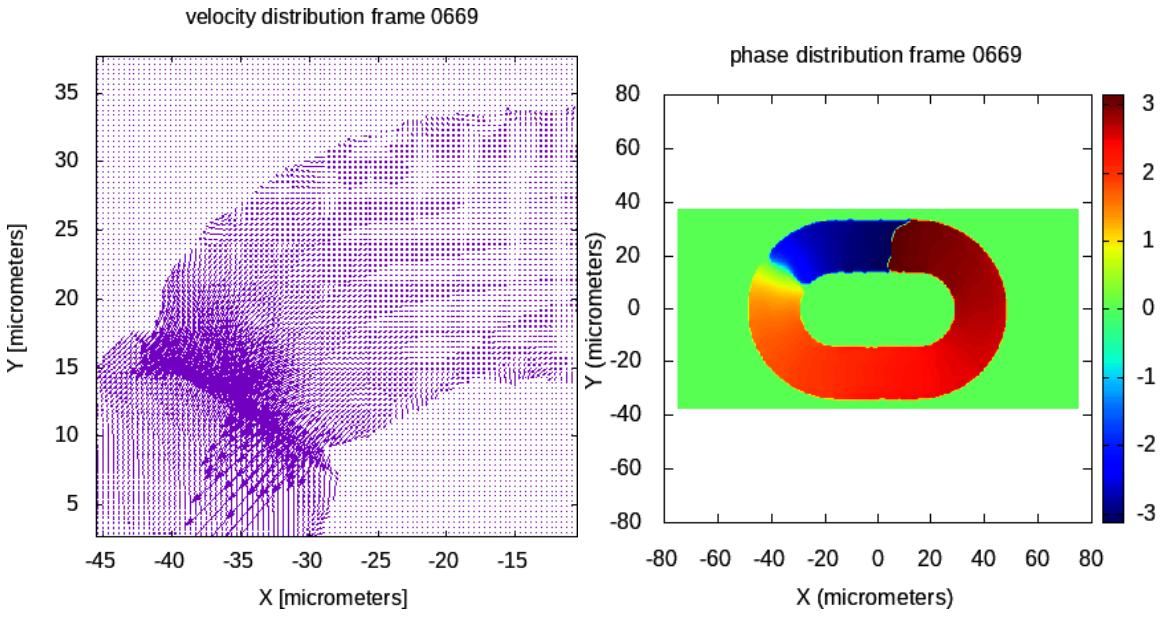

Figure 5.8: The vortex has now passed into the interior edge of the BEC. Left: the flow points forward (with respect to the direction of stirring) through the barrier briefly after the passing of the vortex. Right: we can now see a 2π winding in the phase around the racetrack.

The density depression that moves to the left away from the barrier in Fig. 5.1 is seen to be related to a vortex-antivortex pair moving along the edges of the BEC, with the vortex (CCW) on the inside edge as it must be if there is a macroscopic CCW circulation. This pair moves off opposite to the direction of stirring. As soon as this pair moves away from the barrier region, the back-flow through the barrier returns.

Once there is a unit of macroscopic circulation in the BEC, this will lessen the back-flow through the barrier compared to its value in the absence of flow. However, the strength of the barrier continues to increase and this compensates, building the back-flow back up until it once again exceeds a critical value and the process repeats, creating another unit of circulation. This can continue to happen, until the speed of the circulation exceeds the speed of stirring. For this case study, five units of circulation exceeds the speed of the stirring, as shown in Fig. 5.4. After the circulation speed exceeds the stirring speed, a persistent *forward*-flow through the barrier region is set up. This forward-flow can be seen in Fig. 5.10.

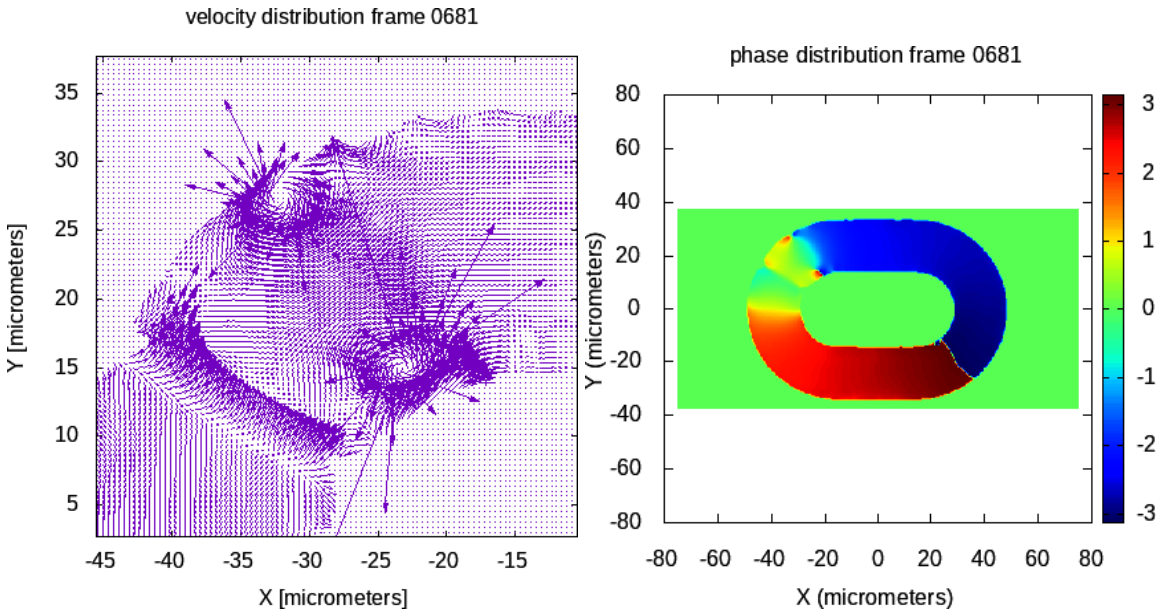

Figure 5.9: The vortex-antivortex pair can be seen in the upper-left corner of the racetrack as the two points in the phase distribution around which the phase cycles through 2π.

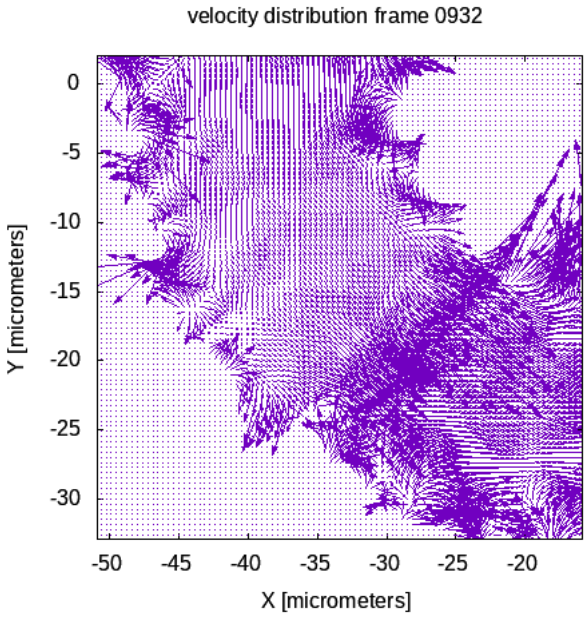

Figure 5.10: Here can be seen the forward-flow through the barrier region, centered around $(x,y) = (-30,-20)\,\mu$m. The barrier is moving down and to the right.

So the process for exciting circulation is carried out in reverse, and we see a CCW vortex leave the interior edge out through the barrier region in Fig. 5.11. Once this happens, the speed of the BEC circulation drops below the stirring speed. The winding number continues to fluctuate around the stirring speed throughout the rest of the stirring schedule until the barrier lowers too much, making the density in the barrier region too high and the flow through the barrier not fast enough to exceed a critical value. By this time the circulation around the racetrack is decided, leaving us with the winding number seen in Fig. 5.3.

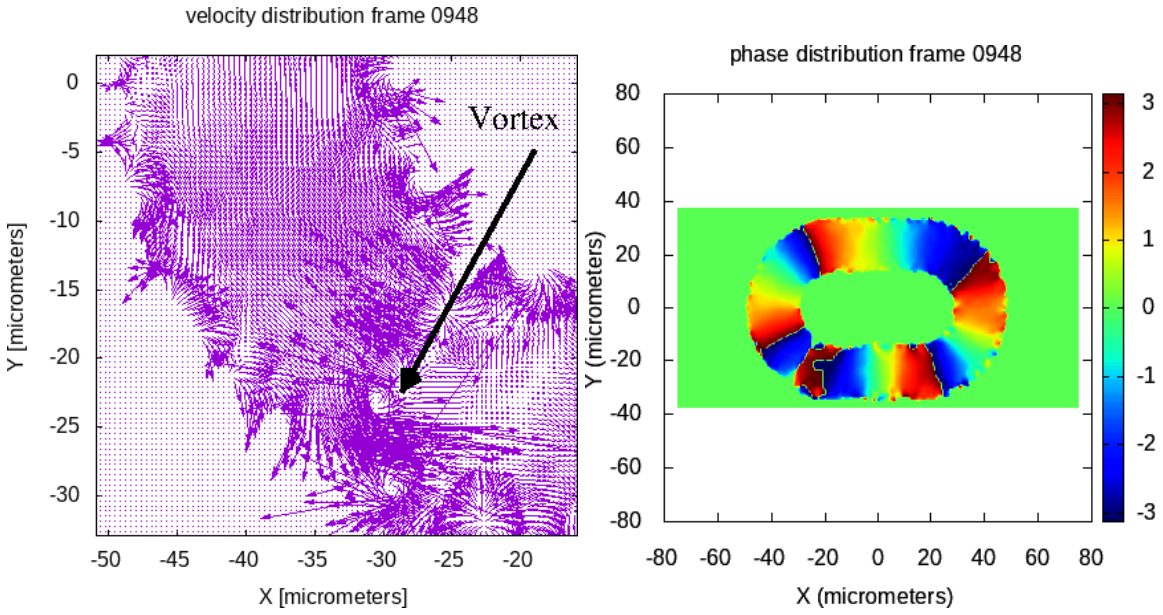

Figure 5.11: A CCW vortex is situated at about $(x,y) = (-30,-23)\,\mu$m, moving out through the barrier. The number of windings in the phase is now $w = 4$ around most paths through the BEC.

Looking at the dynamics of the flow production during the stirring schedule is

informative, and helps us better understand how the final flow obtained after the stirring is complete depends on our parameters. In the future, we plan on performing such fine-timescale simulations on other length and speed cases, and this should give us a good idea of how the racetrack length and stirring speed interplay. Furthermore, we will need to perform such simulations at non-zero temperatures with the ZNG model in order to see exactly how the presence of a non-condensate affects the mechanism by which circulation is produced.

CHAPTER 6

SUMMARY AND CONCLUSIONS

We have conducted a systematic study of the production of smooth atom flow in our racetrack atom circuits at non-zero temperature with simulations using the ZNG model. This was an extension of related modeling at zero temperature using GPE simulations. The ability to produce flow, and the quantity produced, has been characterized across a range of parameters including the length of our racetrack L, the speed of stirring TR, the maximum strength of the stirring barrier $V_{p\max}$, and the temperature of the initial state T.

We found that for fixed (L, TR, T), there are two qualitative features shared amongst all cases. These features are the existence of a critical maximum barrier strength, below which no flow is produced by the end of the stirring schedule, and the leveling off to an average amount of final flow as $V_{p\max}$ is increased. We characterized how these two features depend on the other parameters (L, TR, T). Furthermore by considering the flow dynamics of the condensate for a specific case study, $(L, \mathrm{TR}, T, V_{p\max}) = (30\,\mu\mathrm{m},\ 9,\ 0\,\mathrm{nK}, 1.14\mu)$, on a finer timescale than the systematic study, we have shed light on the underlying mechanism by which circulation around the whole racetrack is created.

Based on the observations of the mechanism by which macroscopic circulation is created and destroyed in our racetrack atomtronic circuit, we can understand in a preliminary way the dependence of w at the end of the stirring schedule on L,TR, and $V_{p\max}$. As the barrier is ramped up, the density in the barrier region lowers. As the local density lowers, a back-flow builds up and depends on the density, the speed at which the BEC is

circulating at (if $w \neq 0$), and the speed of stirring. We can estimate the speed of circulation if we assume that the phase gradient is evenly spaced around the arclength of the racetrack, and we can compare that to the speed of stirring. We have:

$$v_{\text{circ}} = \frac{(h/m)}{2L + 2\pi R} w \tag{6.1}$$

For the case $(L, \text{TR}, T = 0) = (30\,\mu\text{m}, 9)$ at $R = 24\,\mu\text{m}$, $v_{\text{circ}} = (82\,\mu\text{m}/s) \times w$ while $\upsilon_p = 339\,\mu\text{m}\,s^{-1}$. So at $w = 5$, the BEC overtakes the barrier and then we should have a forward-flow, which is what is seen in Fig. 5.10. In fact, since $v_{\text{circ}} \propto (L + \pi R)^{-1}$ and the barrier moves like a rigid body so that on the endcaps $\upsilon_p \propto R$, when there is back-flow it is greater in magnitude towards the outer edge, and this is where we see the vortices spawn when circulation is getting added. When there is a forward-flow it should be greater in magnitude towards the inner edge, and this is where we seen a CCW vortex move out from when circulation is lost.

Furthermore, the longer the racetrack length, the lower v_{circ}/w is, which means that more units of macroscopic circulation can be added to the racetrack before the flow due to it overtakes the barrier. This may explain why longer racetracks can sustain more circulation for a given stirring speed. There is also an effect on the process of adding and subtracting circulation when the barrier transitions from the straightaway to the endcaps and vice versa, but this effect is not understood and needs to be part of future investigations. The role of $V_{p\text{max}}$ is to control not only how strong the barrier gets, but also how quickly it gets there, the rate being $V_{p\text{max}}/(500\,\text{ms})$. This comes into play through the density in the barrier region, the lower it gets the faster the back/forward-flow gets. There are a

few possibilities as to how this works. One idea is that lowering the density could lower an appropriately defined local speed of sound [31]. This would mean that higher temperatures, leading to lower baseline densities, would have a head start and lower values of $V_{p\max}/\mu$ would be needed to get to lower local sound velocities. This is somewhat supported by our simulations, although the racetrack straightaway seems to complicate matters. Another approach would be to modify a model for vortex-antivortex spawning introduced by Feynman [32].

We see that as far as the ZNG model (without collisions between BEC and non-condensate atoms) is concerned, we can understand the creation of quantized circulation states in racetrack Bose-Einstein Condensates by stirring as the production of vortices, and the transfer of them into and out of the interior edge of the BEC through the barrier region. This is backed up by other experimental and theoretical efforts [20, 29, 31], and we have shown that this is a robust phenomenon even at higher temperatures at which less than half of the system is condensed into the ground state. In fact, it is in some sense easier to excite the circulation at higher temperatures since a weaker barrier is required. As far as we are aware, most every investigation to date has focused on our $L = 0\,\mu$m case, the ring BEC.

We have shown that macroscopic circulation can be sustained in a more generalized geometry that does not have azimuthal symmetry. The final circulation in the racetrack is dependant on the interplay of the speed of stirring and the speed of the circulation of the BEC, as well as the length of the racetrack. These results suggest a way to achieve a desired amount of circulation in racetrack type atomtronic circuits. That circulation can then be used along with the added room for components along the straightaway to realize novel

applications.

The next step will be to investigate further the mechanism by which circulation is produced, using simulations on fine timescales such as the one described in Ch. 5. This needs to be done at different length cases, especially $L = 0$, in order to understand better the role of the racetrack length and in particular the effect of barrier transitions from the straightaways to the semi-circular endcaps and from the endcaps to the straightaways. Running these simulations at different stirring speeds will help determine the nature and value of a critical velocity that seems to be exceeded, resulting in the production of vortices that slide through the barrier region.

Furthermore, since the role of non-zero temperature is important for determining the ultimate value of flow produced by stirring, fine-timescale simulations need to be run with the ZNG model to investigate how the non-condensate affects the mechanism by which flow is produced. Eventually, this needs to done while incorporating the collisions between condensate/non-condensate and non-condensate/non-condensate atoms. Including the collisions may or may not alter the mechanism, so it will be an important next step for this research. Interesting extensions of this atomtronics research could come in the form of more complicated geometries than the racetrack. It is an open question in what kinds of BEC geometries it is possible to create smooth, quantized flow.

REFERENCES

[1] M. H. Anderson, J. R. Ensher, M. R. Matthews, C. E. Wieman, and E. A. Cornell, *Observation of Bose-Einstein condensation in a dilute atomic vapor*, Science **269**, 198 (1995).

[2] K. B. Davis, M. O. Mewes, M. R. Andrews, N. J. van Druten, D. S. Durfee, D. M. Kurn, and W. Ketterle, *Bose-Einstein condensation in a gas of sodium atoms*, Phys. Rev. Lett. **75**, 3969 (1995).

[3] C. Zhang, V. W. Scarola, S. Tewari, and S. D. Sarma, *Anyonic braiding in optical lattices*, Proc. Natl Acad. Sci. USA **104**, 18415–18420 (2007).

[4] M. F. Maghrebi, S. Ganeshan, D. J. Clarke, A. V. Gorshkov, and J. D. Sau, *Parafermionic Zero Modes in Ultracold Bosonic Systems*, Phys. Rev. Lett. **115**, 065301 (2015).

[5] S. Eckel, A. Kumar, T. Jacobson, I. B. Spielman, and G. K. Campbell, *A Rapidly Expanding Bose-Einstein Condensate: An Expanding Universe in the Lab*, Phys. Rev. X **8**, 021021 (2018).

[6] C. Ryu and M. G. Boshier, *Integrated coherent matter wave circuits*, New Journal of Physics **17**, 092002 (2015).

[7] L. Amico, G. Birkl, M. Boshier, and L.-C. Kwek, *Focus on atomtronics-enabled quantum technologies*, New Journal of Physics **19**, 020201 (2017).

[8] C. J. Pethick and H. Smith, *Bose–Einstein Condensation in Dilute Gases*, Cambridge University Press, 2nd edition, 2008.

[9] L. Pitaevskii and S. Stringari, *Bose–Einstein Condensation and Superfluidity*, Oxford University Press, 2016.

[10] A. Griffin, T. Nikuni, and E. Zaremba, *Bose-Condensed Gases at Finite Temperatures*, Cambridge University Press, 2009.

[11] O. Oladehin, *Producing Smooth Flow in Atom Circuits by Stirring*, Electronic Theses and Dissertations, 1721, 2018.

[12] G. Rosi, F. Sorrentino, L. Cacciapuoti, M. Prevedelli, and G. M. Tino, *Precision measurement of the Newtonian gravitational constant using cold atoms*, Nature **510**, 518 (2014).

[13] G. M. Tino and M. A. Kasevich, editors, *Atom Interferometry*, Società Italiana di Fisica, 2013.

[14] B. Barrett, R. Geiger, I. Dutta, M. Meunier, B. Canuel, A. Gauguet, P. Bouyer, and A. Landragin, *The Sagnac effect: 20 years of development in matter-wave interferometry*, Comptes Rendus Physique **15**, 875 (2014).

[15] D. Aghamalyan, N. T. Nguyen, F. Auksztol, K. S. Gan, M. M. Valado, P. C. Condylis, L.-C. Kwek, R. Dumke, and L. Amico, *An atomtronic flux qubit: a ring lattice of Bose–Einstein condensates interrupted by three weak links*, New Journal of Physics **18**, 075013 (2016).

[16] M. Gajdacz, T. Opatrný, and K. K. Das, *An atomtronics transistor for quantum gates*, Physics Letters A **378**, 1919 (2014).

[17] T. Köhler, K. Góral, and P. S. Julienne, *Production of cold molecules via magnetically tunable Feshbach resonances*, Rev. Mod. Phys. **78**, 1311 (2006).

[18] G. Gauthier, I. Lenton, N. M. Parry, M. Baker, M. J. Davis, H. Rubinsztein-Dunlop, and T. W. Neely, *Direct imaging of a digital-micromirror device for configurable microscopic optical potentials*, Optica **3**, 1136 (2016).

[19] R. A. Pepino, J. Cooper, D. Z. Anderson, and M. J. Holland, *Atomtronic circuits of diodes and transistors*, Phys. Rev. Lett. **103**, 140405 (2009).

[20] K. C. Wright, R. B. Blakestad, C. J. Lobb, W. D. Phillips, and G. K. Campbell, *Driving Phase Slips in a Superfluid Atom Circuit with a Rotating Weak Link*, Phys. Rev. Lett. **110**, 025302 (2013).

[21] N. P. Proukakis and B. Jackson, *Finite-temperature models of Bose–Einstein condensation*, Journal of Physics B: Atomic, Molecular and Optical Physics **41**, 203002 (2008).

[22] N. N. Bogoliubov, *On the Theory of Superfluidity*, J. Phys. USSR **11**, 23 (1947).

[23] E. Zaremba, T. Nikuni, and A. Griffin, *Dynamics of trapped Bose gases at finite temperatures*, Journal of Low Temperature Physics **116**, 277 (1999).

[24] P.Muruganandam and S. Adhikari, *Fortran programs for the time-dependent Gross–Pitaevskii equation in a fully anisotropic trap*, Computer Physics Communications **180**, 1888 (2009).

[25] V. Bagnato, D. E. Pritchard, and D. Kleppner, *Bose-Einstein condensation in an external potential*, Phys. Rev. A **35**, 4354 (1987).

[26] G. Baym and C. J. Pethick, *Ground-State Properties of Magnetically Trapped Bose-Condensed Rubidium Gas*, Phys. Rev. Lett. **76**, 6 (1996).

[27] R. Mathew, A. Kumar, S. Eckel, F. Jendrzejewski, G. K. Campbell, M. Edwards, and E. Tiesinga, *Self-heterodyne detection of the in situ phase of an atomic superconducting quantum interference device*, Phys. Rev. A **92**, 033602 (2015).

[28] F. Jendrzejewski, S. Eckel, N. Murray, C. Lanier, M. Edwards, C. J. Lobb, and G. K. Campbell, *Resistive Flow in a Weakly Interacting Bose-Einstein Condensate*, Phys. Rev. Lett. **113**, 045305 (2014).

[29] S. Eckel, J. G. Lee, F. Jendrzejewski, N. Murray, C. W. Clark, C. J. Lobb, W. D. Phillips, M. Edwards, and G. K. Campbell, *Hysteresis in a quantized superfluid 'atomtronic' circuit*, Nature **506**, 200 (2014).

[30] N. Murray, M. Krygier, M. Edwards, K. C. Wright, G. K. Campbell, and C. W. Clark, *Probing the circulation of ring-shaped Bose-Einstein condensates*, Phys. Rev. A **88**, 053615 (2013).

[31] A. C. Mathey, C. W. Clark, and L. Mathey, *Decay of a superfluid current of ultracold atoms in a toroidal trap*, Phys. Rev. A **90**, 023604 (2014).

[32] R. Feynman, Chapter ii application of quantum mechanics to liquid helium, in *Progress in Low Temperature Physics*, edited by C. Gorter, Vol. 1 of *Progress in Low Temperature Physics*, p. 17 – 53, Elsevier, 1955.

APPENDIX A

DERIVATION OF THE GROSS-PITAEVSKII EQUATION

Quantum mechanical systems of many particles that move much slower than the speed of light in a vacuum ($c = 3 \times 10^8 \frac{\text{m}}{\text{s}}$) can be described by the many-body Schrödinger equation

$$i\hbar \frac{\partial}{\partial t} \Psi(\mathbf{r}_1, ..., \mathbf{r}_N, t) = \hat{\mathscr{H}} \Psi(\mathbf{r}_1, ..., \mathbf{r}_N, t). \tag{A.1}$$

$\Psi(\mathbf{r}_1, ..., \mathbf{r}_N, t)$ is the many-body wavefunction which contains all the information about a system of N generally interacting particles that have coordinates $\mathbf{r}_i$ at time t, and is the solution that we seek. $\hat{\mathscr{H}}$ is called the many-body Hamiltonian, and is a linear operator that represents the total energy of the system (kinetic plus potential). This can include external potentials imposed upon the system as well as interaction potentials between the different particles. For our purposes, Eq. (A.1) is a partial differential equation in $3N + 1$ independent variables. All the particles of the system are assumed to be identical bosons of mass m (particles with integer valued intrinsic angular momentum, often called “spin"), and the Hamiltonian will take the form

$$\hat{\mathscr{H}} = \sum_{k=1}^{N} \left(\frac{-\hbar^2}{2m} \nabla_k^2 + V(\mathbf{r}_k) \right) + g \sum_{k=2}^{N} \sum_{j=1}^{k-1} \delta(\mathbf{r}_k - \mathbf{r}_j), \tag{A.2}$$

$\hbar = 1.055 \times 10^{-34}$J·s being the reduced Planck’s constant (pronounced “h-bar"). What we have here is a sum over single-particle operators that only act on the k-th particle plus a sum over distinct interacting pairs (k, j). The single-particle operators are kinetic energy operators proportional to ∇_k^2, and the external potential at position $\mathbf{r}_k$, $V(\mathbf{r}_k)$. The interaction

between the particles has been assumed to be entirely due to contact forces in two-body collisions expressed as a Dirac delta-function $\delta(\mathbf{r}_k - \mathbf{r}_j)$ and characterized by a strength $g = 4\pi\hbar^2 a_s/m$, with a_s being the s-wave scattering length which is a property of the particular atomic species. We cannot solve Eq. (A.1) exactly with this Hamiltonian (in fact we cannot in the vast majority of situations), however we can attempt to find stationary, approximate ground-state solutions using the variational method of quantum mechanics wherein we guess a trial form of the wavefunction with parameters we can vary to find the form that minimizes the expectation value of the energy (since we want the ground state). Since the many-body wavefunction for identical bosons obeys the condition $\Psi(...,\mathbf{r}_i,...,\mathbf{r}_j,...,t) = \Psi(...,\mathbf{r}_j,...,\mathbf{r}_i,...,t)$, an arbitrary number of bosons can occupy the same quantum state and we can take as our trial wavefunction $\Psi(\mathbf{r}_1,...,\mathbf{r}_N,t) = e^{-iEt/\hbar}\prod_{k''=1}^{N}\phi(\mathbf{r}_{k''})$, where ϕ is the single-particle ground state orbital. This form of the wavefunction would not work if the particles were fermions (particles with odd half-integer values of spin), since they obey an antisymmetric condition $\Psi(...,\mathbf{r}_i,...,\mathbf{r}_j,...,t) = -\Psi(...,\mathbf{r}_j,...,\mathbf{r}_i,...,t)$, a consequence of which is the Pauli exclusion principle that states that no two fermions can occupy the same quantum state. All of the atoms are assumed to be in the same state of the system ϕ, and the wavefunction is symmetric under the interchange of two particles. By substituting our trial wavefunction into Eq. (A.1), multiplying both sides by $\prod_{k'=1}^{N}\phi^*(\mathbf{r}_{k'})$ and integrating over all the space-coordinates of the system, with $\int d^3R = \int d^3r_1 \int d^3r_2 ... \int d^3r_N$, we get

the expectation value of the Hamiltonian

$$E[\phi^*] = \int d^3R \left(\prod_{k'=1}^{N} \phi^*(\mathbf{r}_{k'})\right) \sum_{k=1}^{N} \left(\frac{-\hbar^2}{2m}\nabla_k^2 + V(\mathbf{r}_k)\right) \left(\prod_{k''=1}^{N} \phi(\mathbf{r}_{k''})\right) + g\int d^3R \left(\prod_{k'=1}^{N} \phi^*(\mathbf{r}_{k'})\right) \sum_{k=2}^{N}\sum_{j=1}^{k-1} \delta(\mathbf{r}_k - \mathbf{r}_j) \left(\prod_{k''=1}^{N} \phi(\mathbf{r}_{k''})\right). \tag{A.3}$$

We can separate off the wavefunctions not participating in the sums and write

$$E[\phi^*] = \int d^3R \sum_{k=1}^{N} \left(\prod_{k'\neq k}^{N} \phi^*(\mathbf{r}_{k'})\phi(\mathbf{r}_{k'})\right) \phi^*(\mathbf{r}_k) \left(\frac{-\hbar^2}{2m}\nabla_k^2 + V(\mathbf{r}_k)\right) \phi(\mathbf{r}_k) + g\int d^3R \sum_{k=2}^{N}\sum_{j=1}^{k-1} \left(\prod_{k'\neq k\neq j}^{N} \phi^*(\mathbf{r}_{k'})\phi(\mathbf{r}_{k'})\right) \phi^*(\mathbf{r}_k)\phi^*(\mathbf{r}_j)\delta(\mathbf{r}_k - \mathbf{r}_j)\phi(\mathbf{r}_k)\phi(\mathbf{r}_j). \tag{A.4}$$

Now we can use the fact that the many-body wavefunction is normalized and therefore satisfies

$$\int d^3R\, \Psi^*(\mathbf{r}_1, ..., \mathbf{r}_N)\Psi(\mathbf{r}_1, ..., \mathbf{r}_N) = 1, \tag{A.5}$$

and the properties of the Dirac delta-function to reduce Eq. (A.4) to

$$E[\phi^*] = \sum_{k=1}^{N} \int d^3r_k \phi^*(\mathbf{r}_k)\hat{h}_k\phi(\mathbf{r}_k) + g\sum_{k=2}^{N}\sum_{j=1}^{k-1} \int d^3r_k \phi^*(\mathbf{r}_k)\phi^*(\mathbf{r}_k)\phi(\mathbf{r}_k)\phi(\mathbf{r}_k), \tag{A.6}$$

where $\hat{h}_k = \left(\frac{-\hbar^2}{2m}\nabla_k^2 + V(\mathbf{r}_k)\right)$. We can swap the sums in Eq. (A.6) for a factors of N and $N(N-1)/2$ respectively, since all the particles have the same wavefunction, leaving us with

$$E[\phi^*] = N\int d^3r \left(\phi^*(\mathbf{r})\hat{h}\phi(\mathbf{r}) + \frac{g}{2}(N-1)\phi^{*2}(\mathbf{r})\phi^2(\mathbf{r})\right). \tag{A.7}$$

Now what we want to do is add in the constraint that $G[\phi^*] = \int d^3r\phi^*\phi - 1 = 0$, and find the form of ϕ that yields a stationary value of $E[\phi^*] - \lambda G[\phi^*]$, where λ is a Lagrange

multiplier. This can be accomplished by allowing either ϕ or ϕ^* to vary arbitrarily. Here we vary ϕ^*, and denoting this variation by $\delta\phi^*$ we have

$$\begin{aligned}
0 &= (E[\phi^* + \delta\phi^*] - E[\phi^*]) - \lambda(G[\phi^* + \delta\phi^*] - G[\phi^*]) \\
&= \left(\int d^3r \Big((\phi^*(\mathbf{r}) + \delta\phi^*(\mathbf{r}))\hat{h}\phi(\mathbf{r}) + \frac{g}{2}(N-1)(\phi^*(\mathbf{r}) + \delta\phi^*(\mathbf{r}))^2\phi^2(\mathbf{r}) \Big) \right. \qquad \text{(A.8)} \\
&\quad \left. - \int d^3r \left(\phi^*(\mathbf{r})\hat{h}\phi(\mathbf{r}) + \frac{g}{2}(N-1)\phi^{*2}(\mathbf{r})\phi^2(\mathbf{r}) \right) \right) \\
&\quad - \lambda \left(\int d^3r(\phi^*(\mathbf{r}) + \delta\phi^*(\mathbf{r}))\phi(\mathbf{r}) - 1 - \int d^3r\phi^*(\mathbf{r})\phi(\mathbf{r}) + 1 \right) \qquad \text{(A.9)}
\end{aligned}$$

Keeping only terms linear in $\delta\phi^*$ we see that (with $\phi^*\phi = |\phi|^2$)

$$\int d^3r\ \delta\phi^* \left\{ N\left(\hat{h}\phi + g(N-1)|\phi|^2\phi\right) - \lambda\phi \right\} = 0. \qquad \text{(A.10)}$$

Since the $\delta\phi^*$ are arbitrary, we can conclude that $\phi(\mathbf{r})$ must satisfy the equation

$$\left(\frac{-\hbar^2}{2m}\nabla^2 + V(\mathbf{r}) + g(N-1)|\phi|^2 \right)\phi = \mu\phi. \qquad \text{(A.11)}$$

Equation (1.1) is known as the time-independent Gross-Pitaevskii equation (GPE), and we have defined $\mu = \lambda/N$ which is still unknown. We have used the definition $\hat{h} = \left(\frac{-\hbar^2}{2m}\nabla^2 + V(\mathbf{r})\right)$ here since Eq. (A.11) is how the equation is typically written in the literature. The factor of $N-1$ shows up because it was assumed that there is a definite number N of atoms in the condensate. Another way to derive the time-independent GPE is to take as a trial wavefunction a coherent superposition of ground states with different numbers of atoms. Doing so will result in a factor of N rather than $N-1$, however it corresponds to the average number of atoms instead. We note that the single-particle wavefunction ϕ is related to the condensate wavefunction Φ used in the body of this thesis in the following way,

$\Phi = \sqrt{N}\phi$, and therefore the condensate wavefunction is normalized so that $\int d^3r|\Phi|^2 = N$. If we multiply both sides of the GPE by ϕ^* and integrate over all space, we get a formula for μ:

$$\mu = \int d^3r \left(\phi^* \hat{h} \phi + g(N-1)|\phi|^4\right). \tag{A.12}$$

Considering the energy functional (A.7), we can compute the chemical potential $\partial E/\partial N$ and show that (since the entropy and volume are fixed):

$$\frac{\partial E}{\partial N} = \int d^3r \left(\phi^* \hat{h} \phi + g(N-1/2)|\phi|^4\right). \tag{A.13}$$

We see that Eqs. (A.12) and (A.13) are the same if $N >> 1$, and conclude that in this limit we can interpret μ as the chemical potential of the condensate, i.e. the energy required to add another particle to it. Solutions of Eq. (A.11) and the determination of the chemical potential from Eq. (A.12) for a given external potential $V(\mathbf{r})$ yield an equilibrium mean-field approximate form of the wavefunction that all particles in the system share. A time-dependent GPE can be found as well via the action principle [8]

$$\delta \int_{t_1}^{t_2} L(\phi, \phi^*, t)\, dt = 0 \tag{A.14}$$

with the Lagrangian (for large N)

$$L(\phi, \phi^*, t) = \int d^3r \left[\frac{i\hbar}{2}\left(\phi^* \frac{\partial \phi}{\partial t} - \phi \frac{\partial \phi^*}{\partial t}\right) - \left(\frac{\hbar^2}{2m}|\nabla\phi|^2 + V(\mathbf{r})|\phi|^2 + (gN/2)|\phi|^4\right)\right]. \tag{A.15}$$

There are a number of books that have consolidated much of the research on this subject, such as Refs. [8] and [9].

APPENDIX B

FINAL PHASE DISTRIBUTION

The figures in this appendix each display a label like `L_30_TR_06_T_150`, denoting the parameters of the corresponding simulations. In this example, the length is $L = 30\,\mu$m, the stir speed is TR=6, and the temperature is $T = 150$ nK. Each frame is the phase distribution at the end of an entire simulation, $\theta(x, y, 0, t_{\text{final}})$. The numbers above the frames are the fractions $V_{p\max}/\mu$. The color scale represents the phase from $-\pi$ to π, going from blue to red. The winding numbers w are best found by counting the number of yellow bands (in grey scale this corresponds to the number of brightest bands) across the channel.

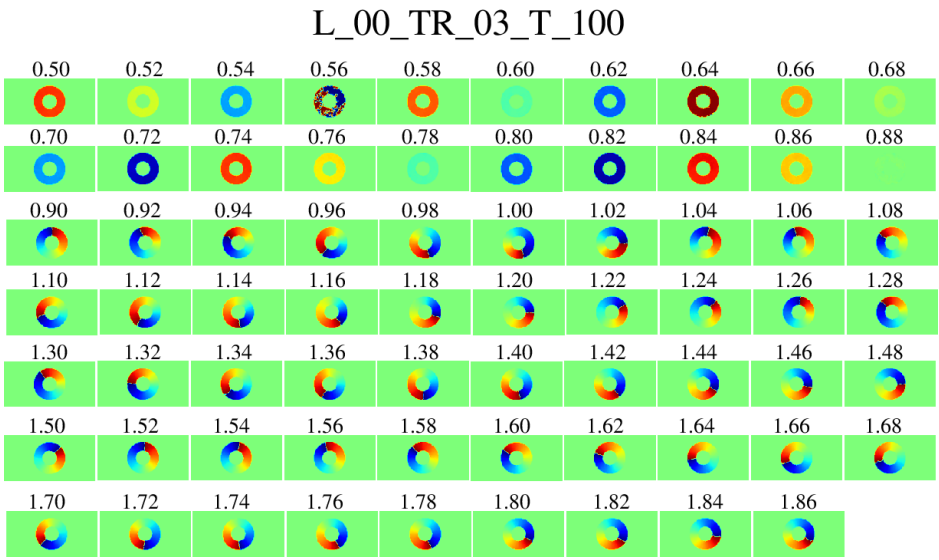

L_00_TR_03_T_150

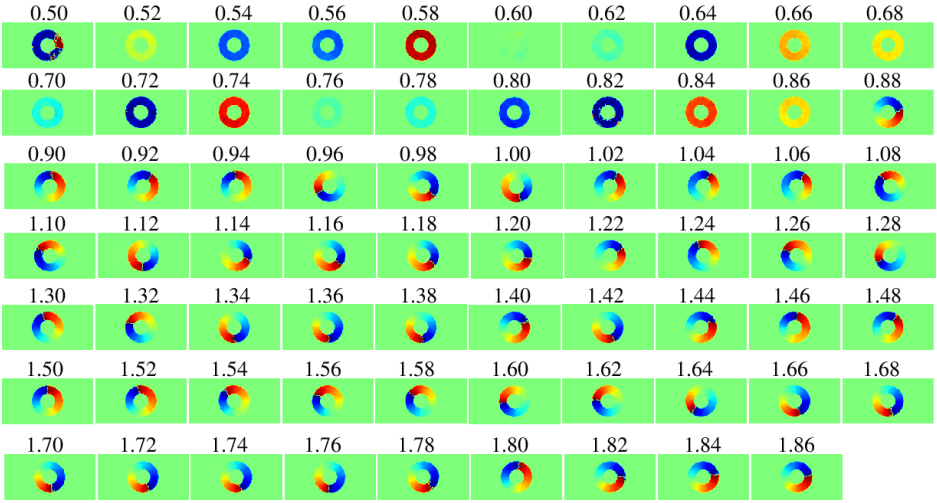

L_00_TR_03_T_200

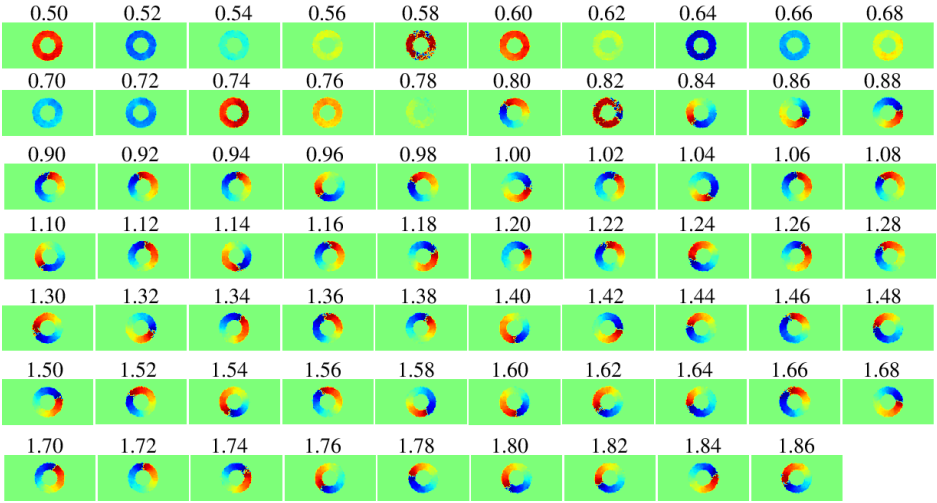

L_00_TR_06_T_100

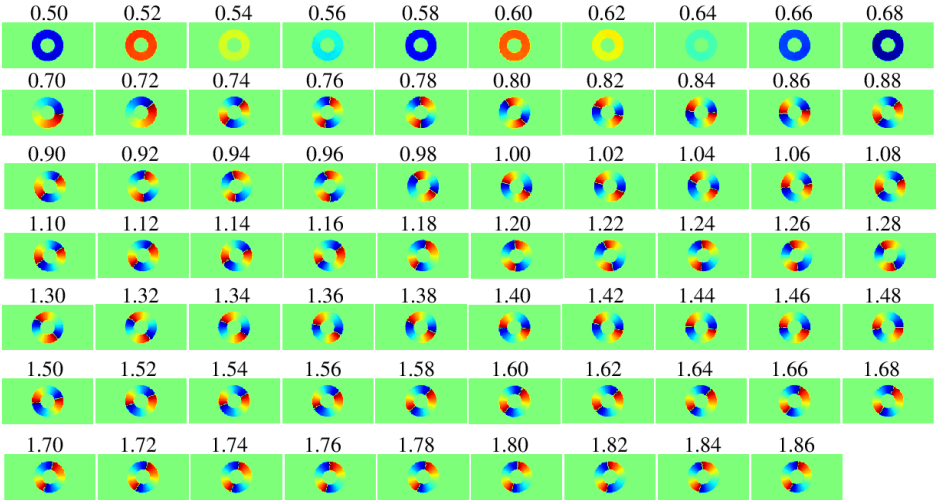

L_00_TR_06_T_150

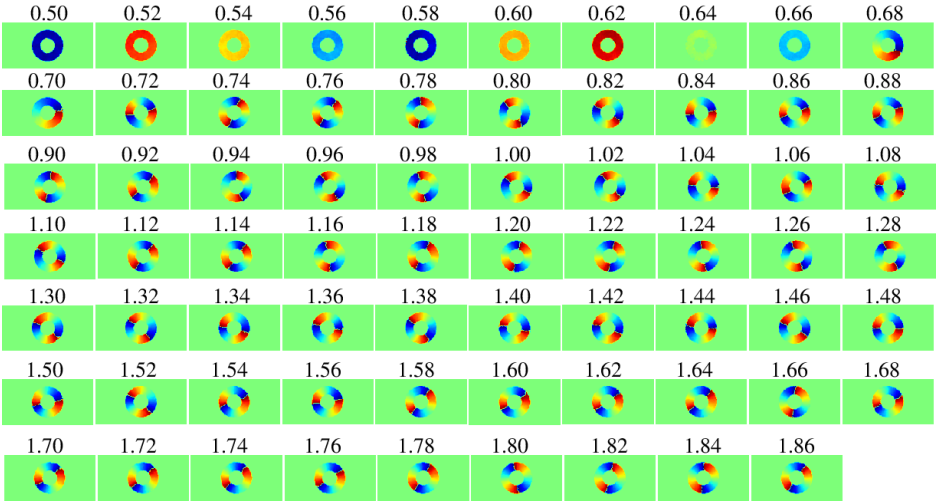

L_00_TR_06_T_200

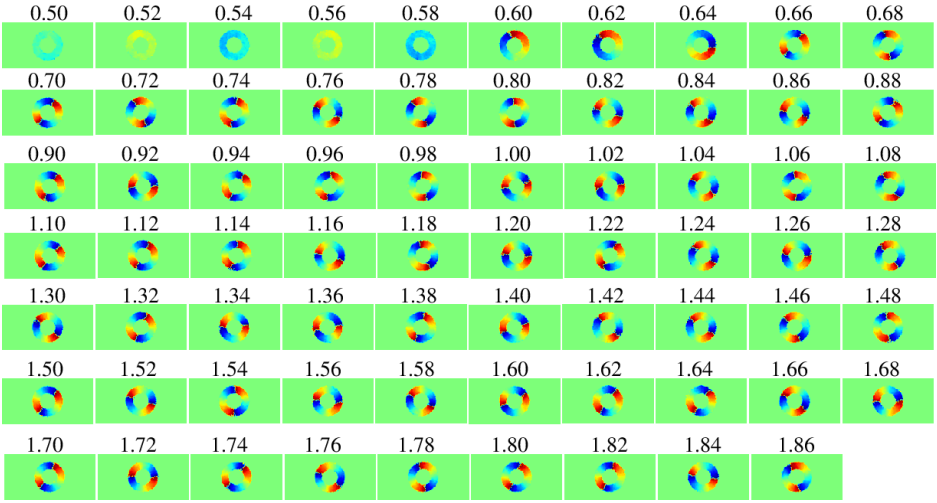

L_00_TR_09_T_100

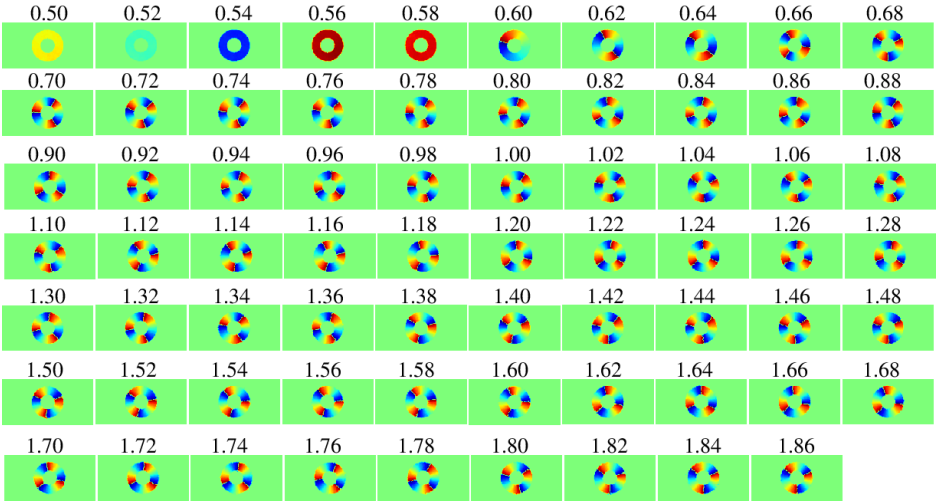

L_00_TR_09_T_150

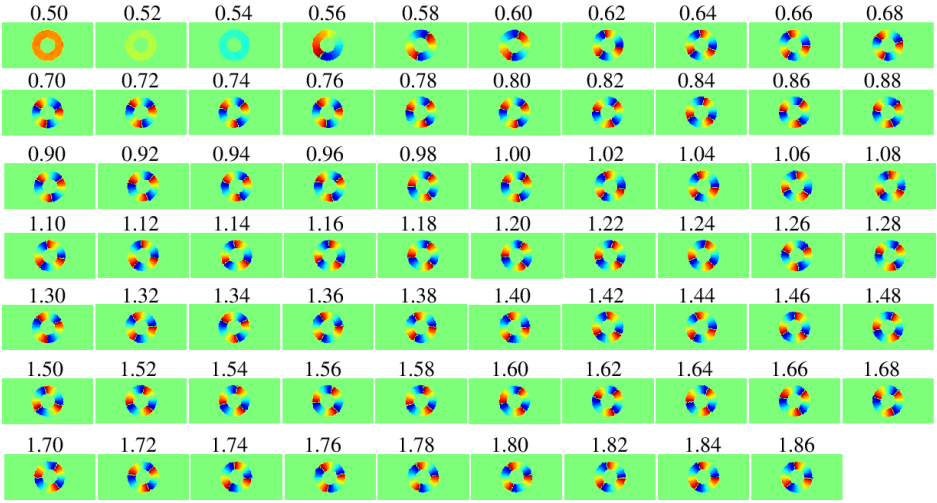

L_00_TR_09_T_200

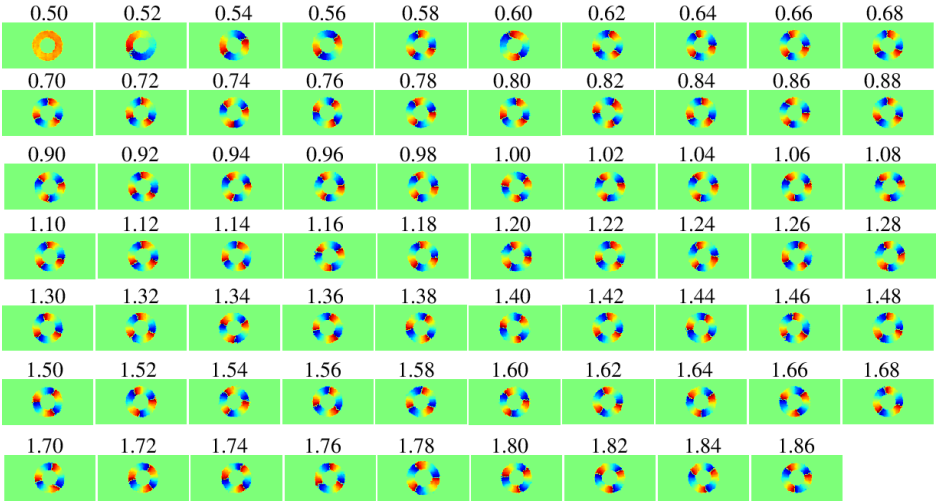

L_00_TR_12_T_100

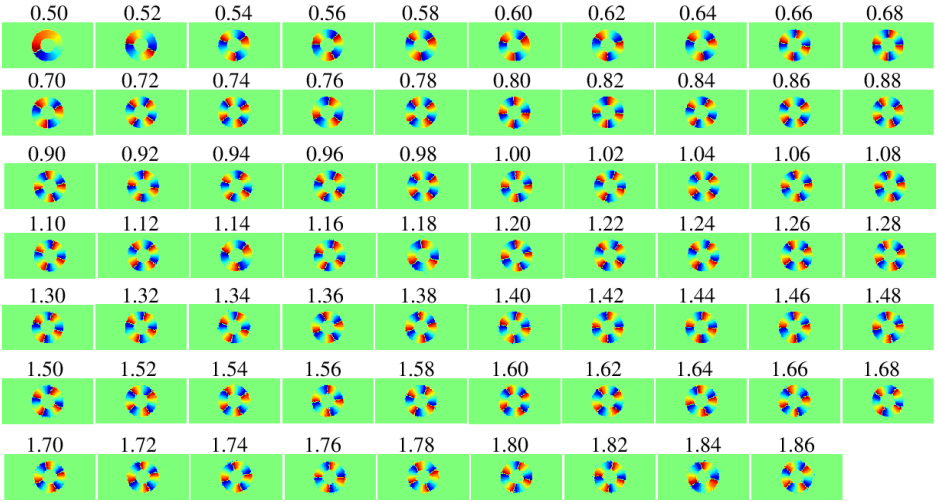

L_00_TR_12_T_150

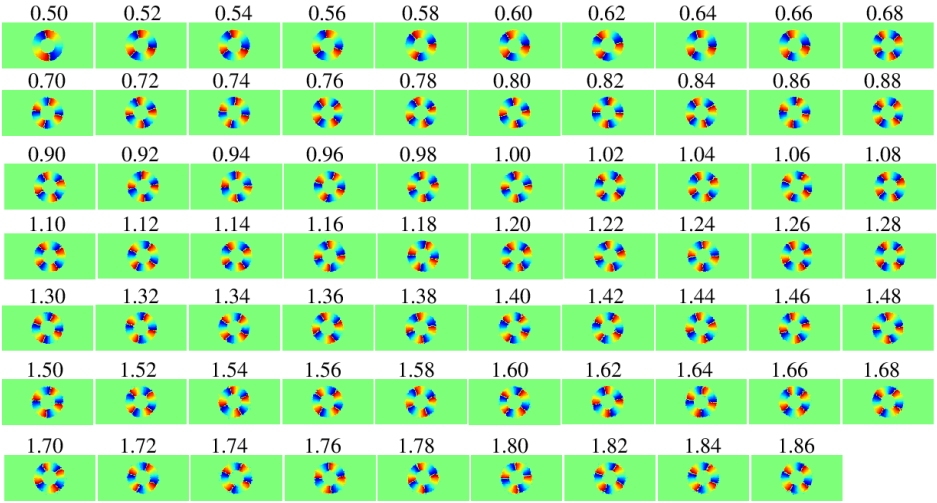

L_00_TR_12_T_200

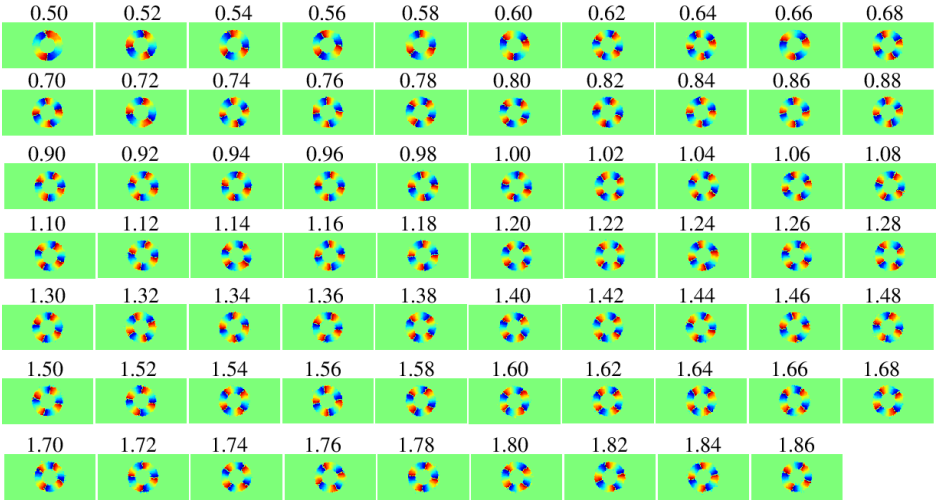

L_30_TR_03_T_100

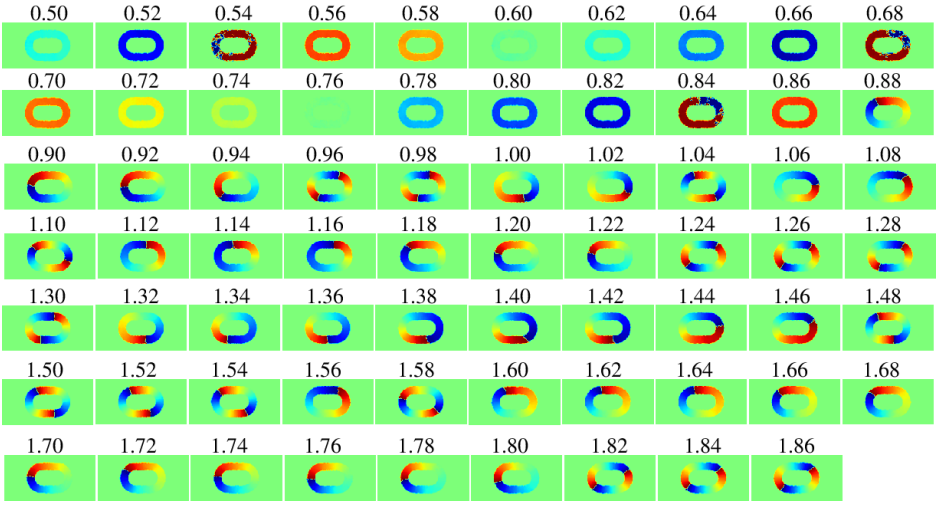

L_30_TR_03_T_150

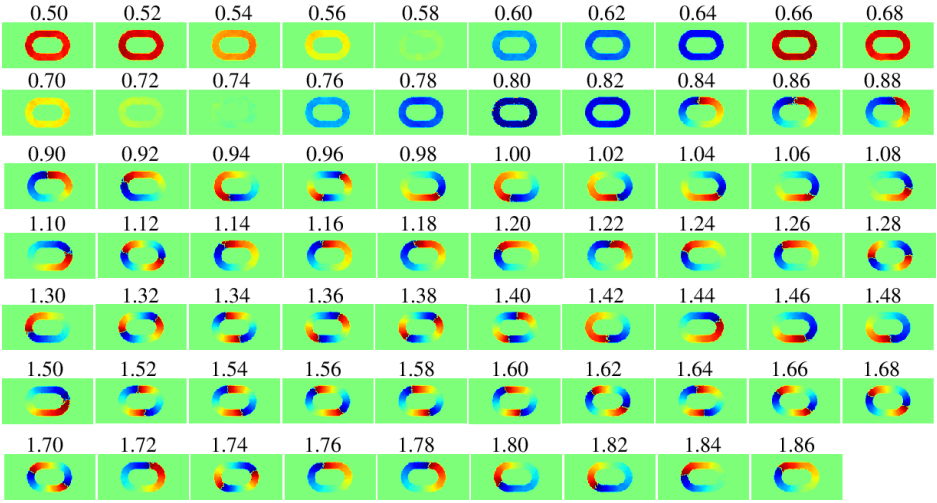

L_30_TR_03_T_200

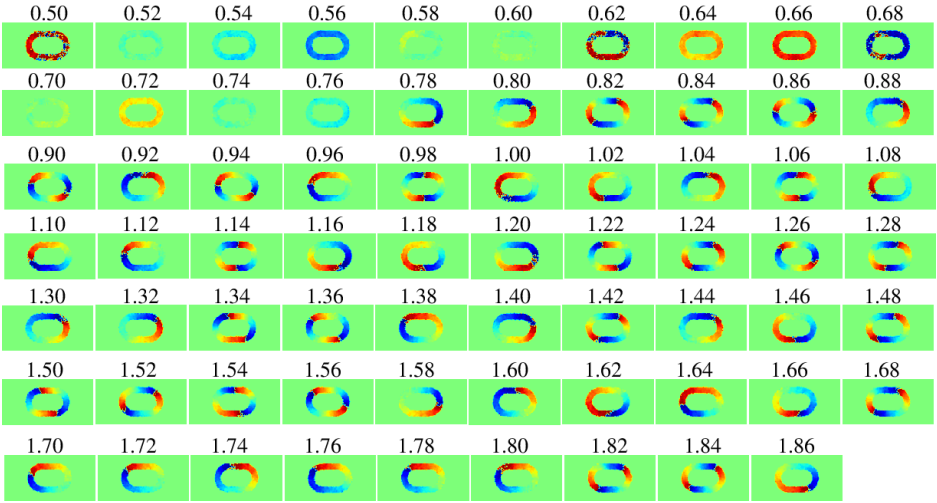

L_30_TR_06_T_100

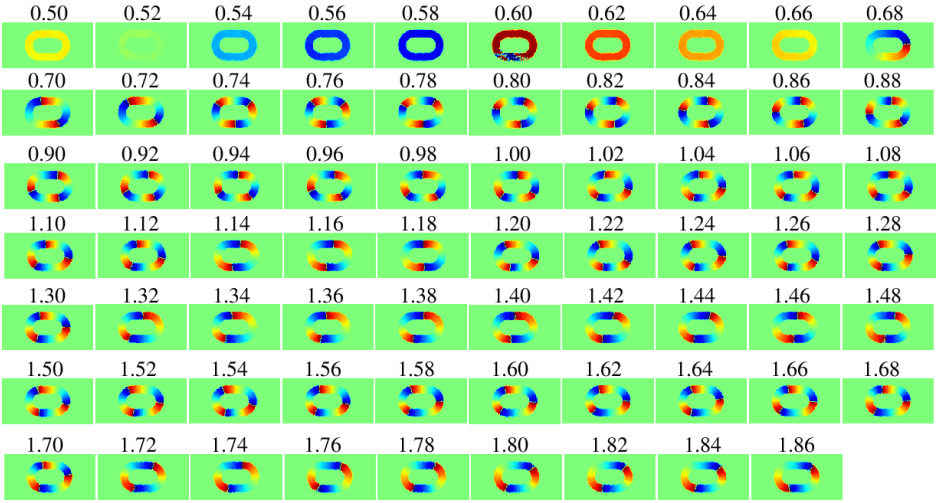

L_30_TR_06_T_150

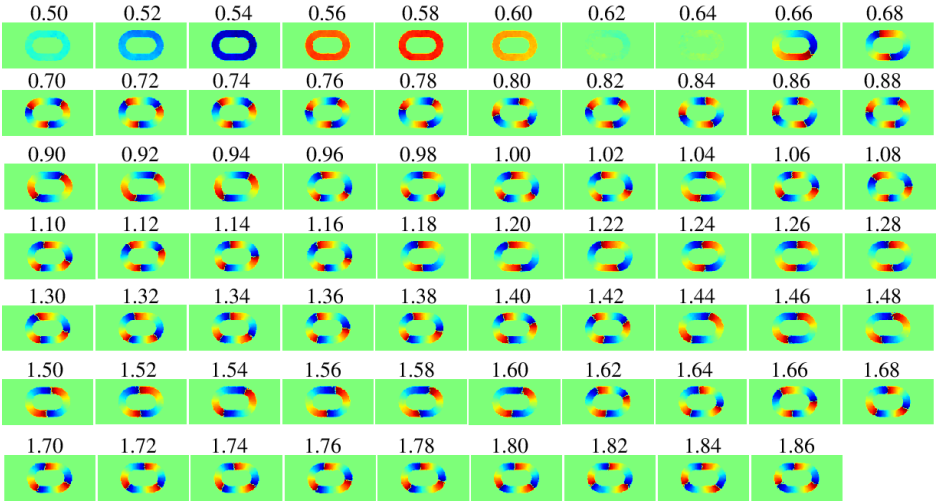

L_30_TR_06_T_200

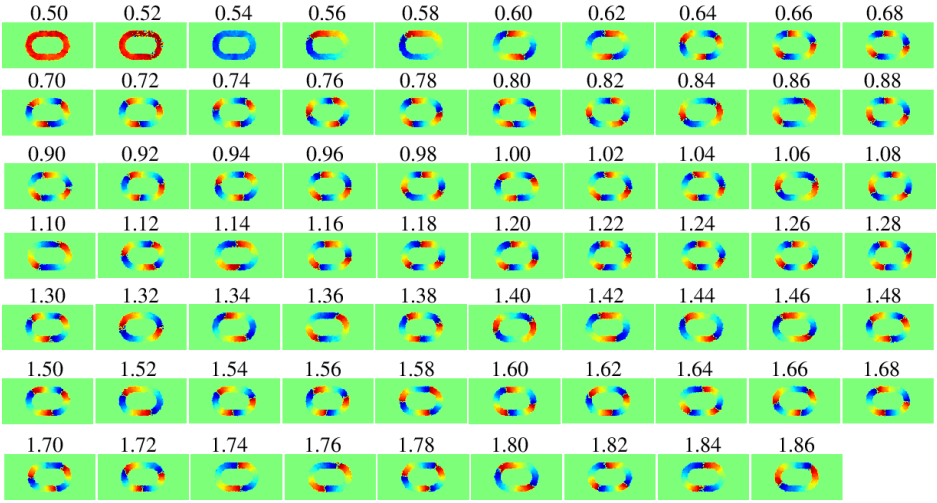

L_30_TR_09_T_100

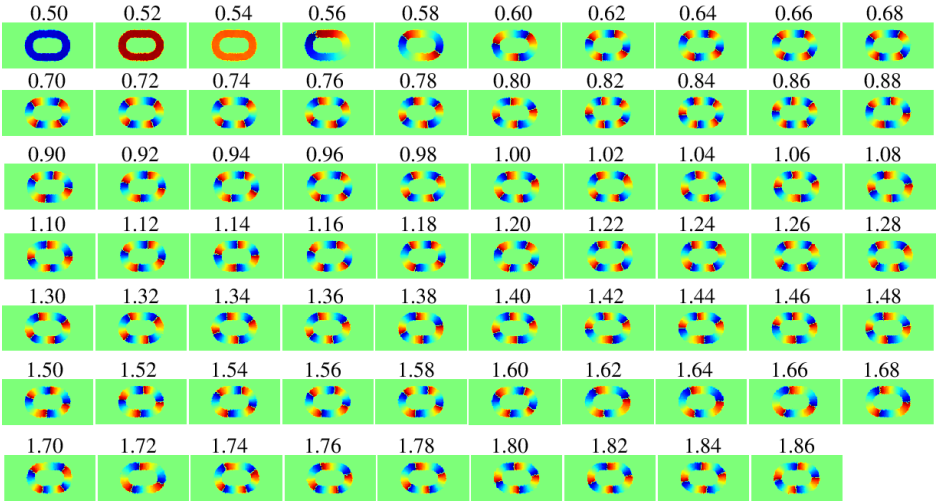

L_30_TR_09_T_150

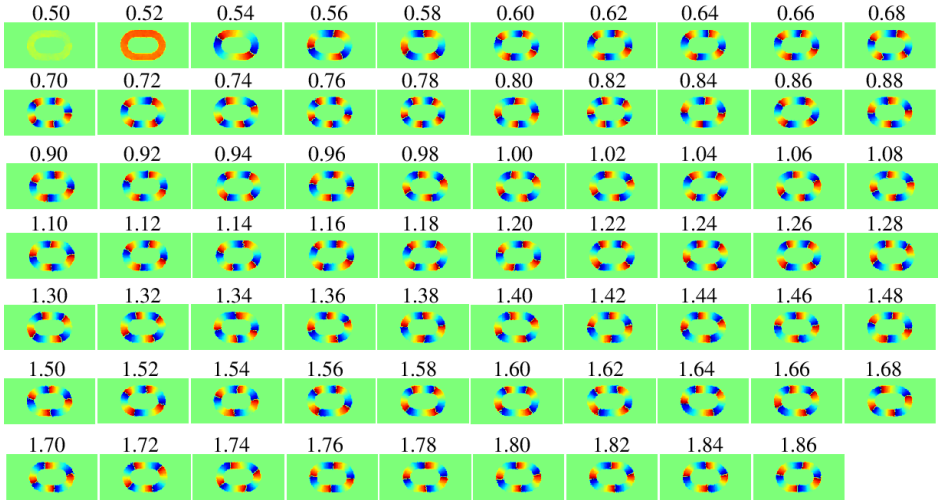

L_30_TR_09_T_200

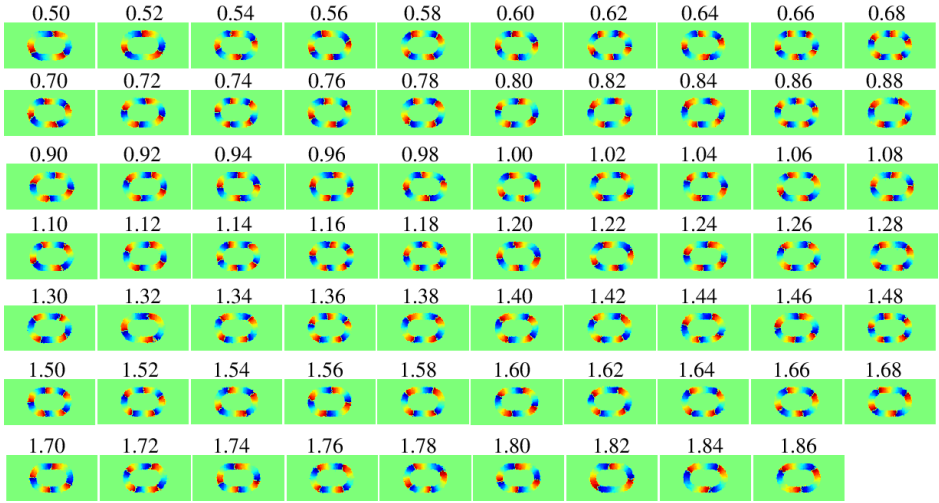

L_30_TR_12_T_100

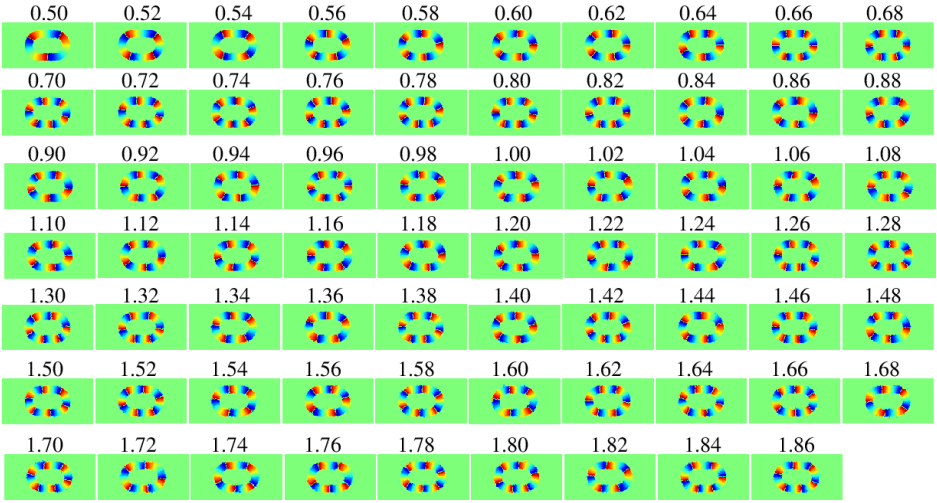

L_30_TR_12_T_150

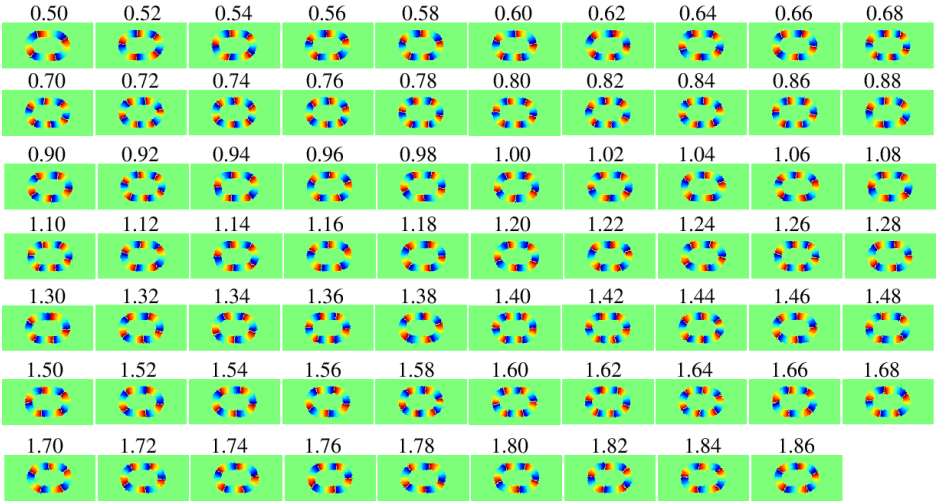

L_30_TR_12_T_200

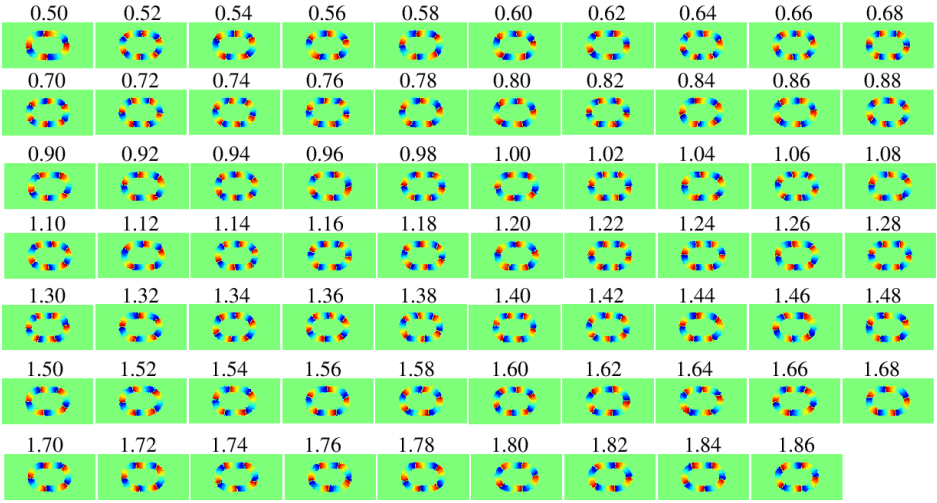

L_60_TR_03_T_100

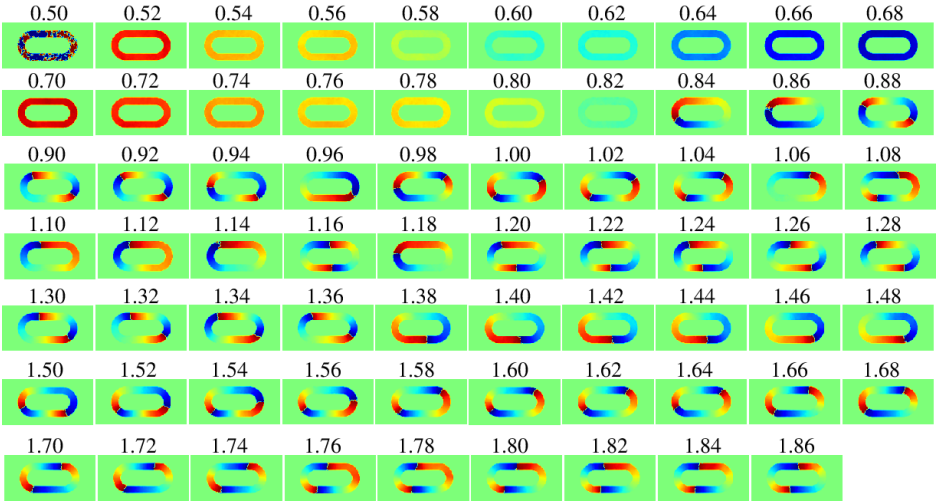

L_60_TR_03_T_150

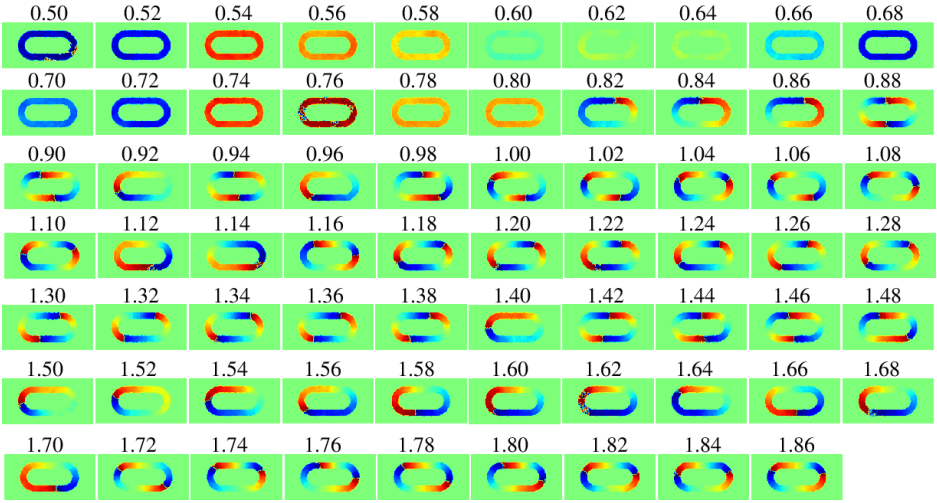

L_60_TR_03_T_200

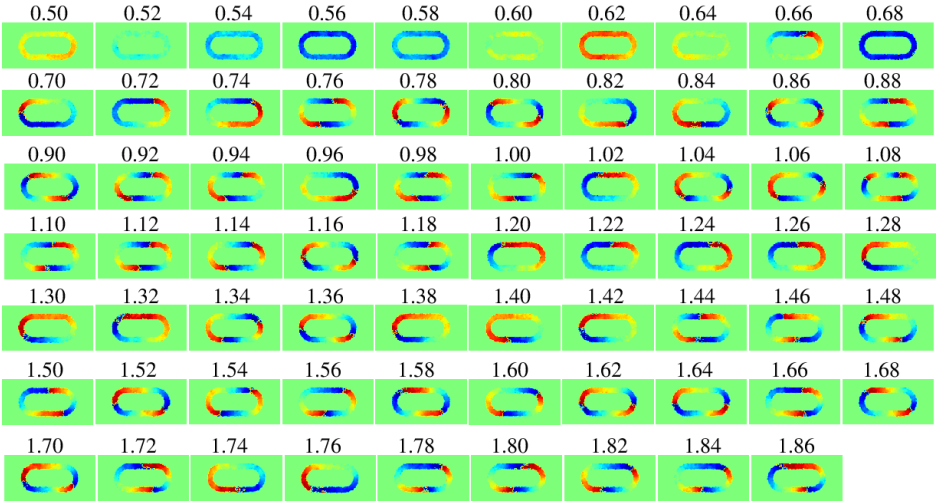

L_60_TR_06_T_100

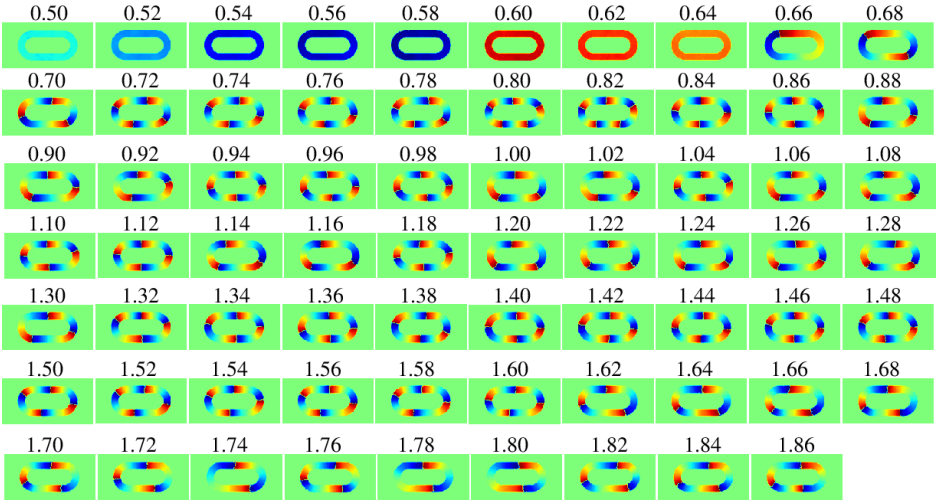

L_60_TR_06_T_150

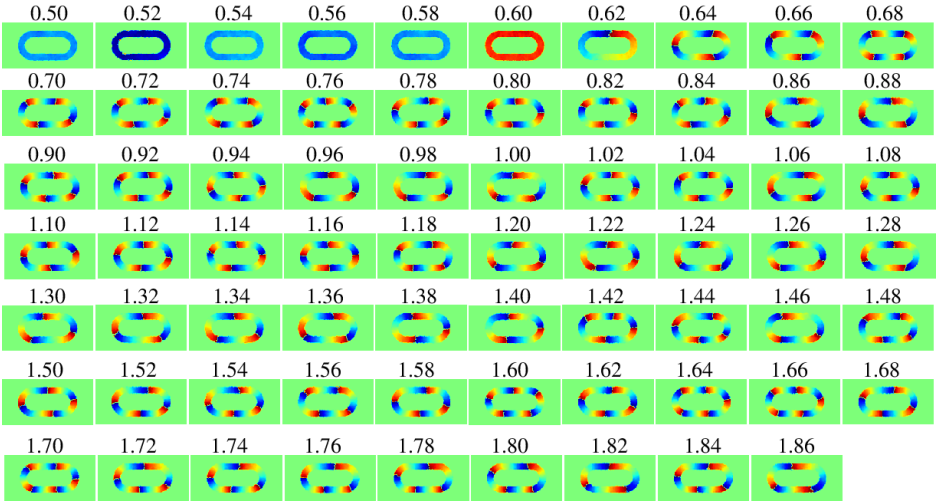

L_60_TR_06_T_200

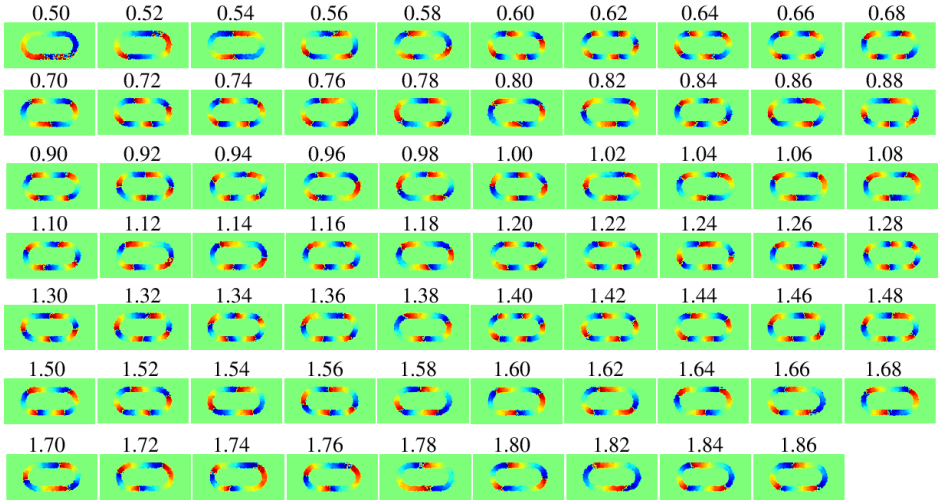

L_60_TR_09_T_100

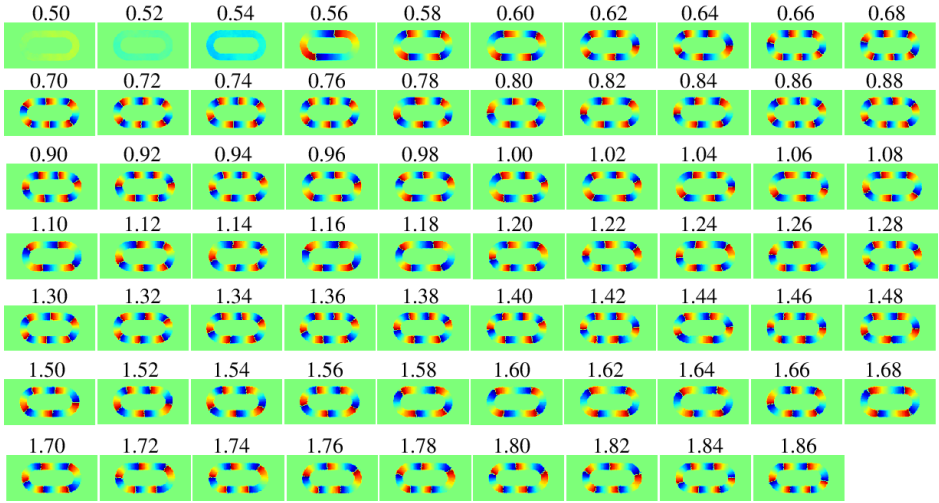

L_60_TR_09_T_150

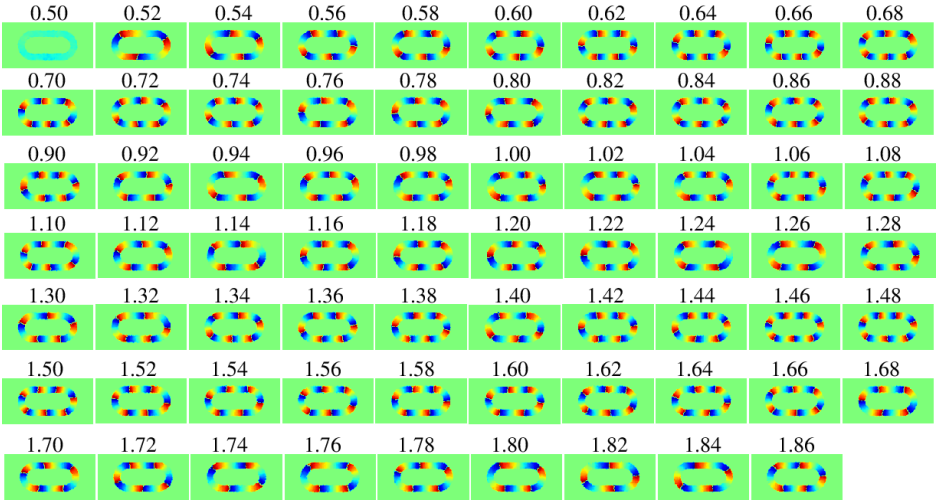

L_60_TR_09_T_200

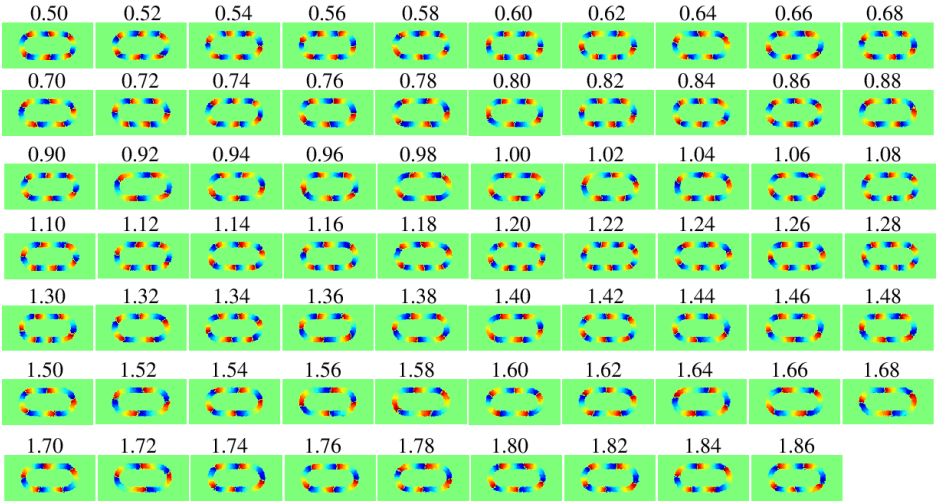

L_60_TR_12_T_100

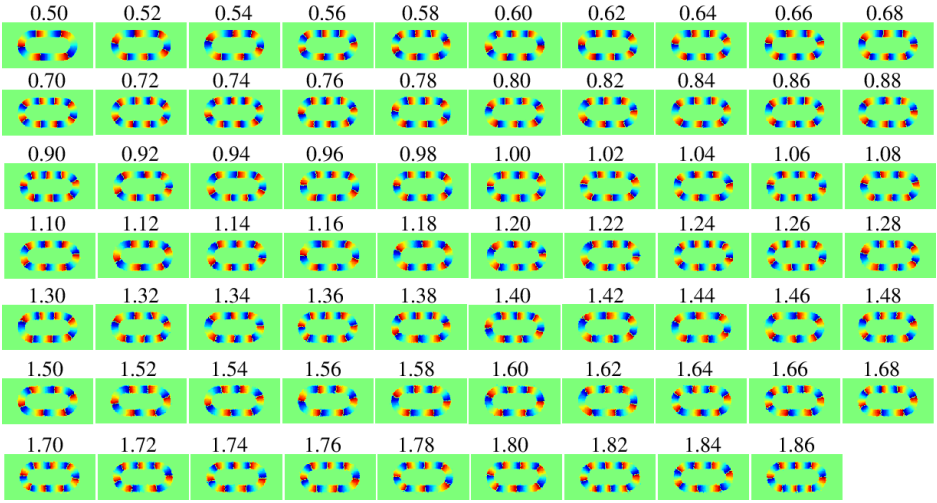

L_60_TR_12_T_150

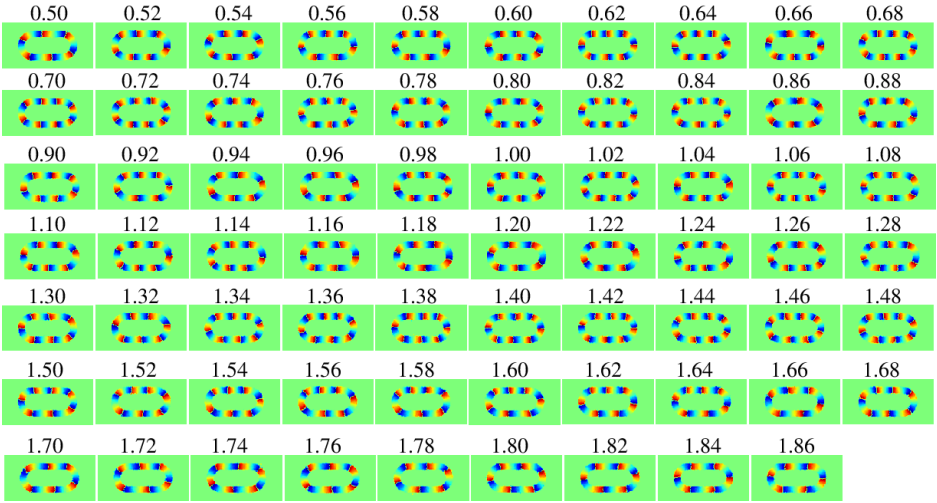

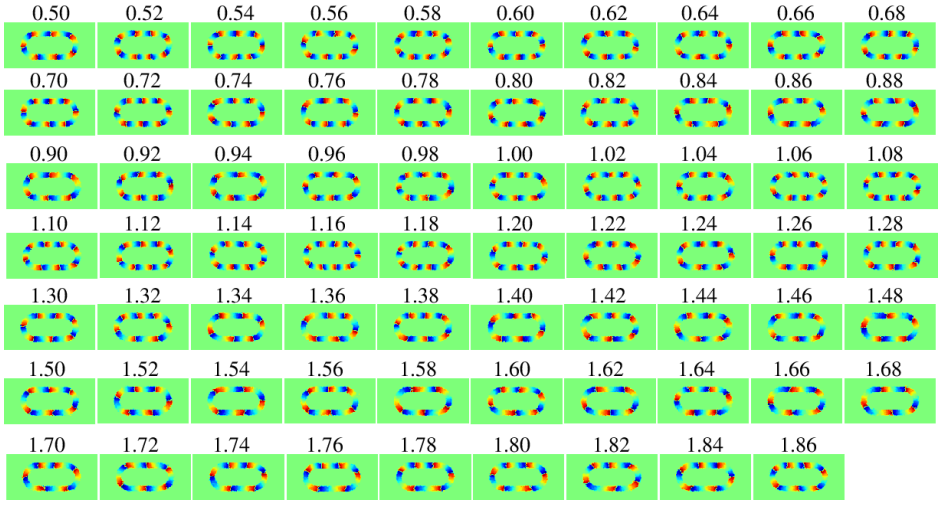
L_60_TR_12_T_200
0.50 0.52 0.54 0.56 0.58 0.60 0.62 0.64 0.66 0.68
0.70 0.72 0.74 0.76 0.78 0.80 0.82 0.84 0.86 0.88
0.90 0.92 0.94 0.96 0.98 1.00 1.02 1.04 1.06 1.08
1.10 1.12 1.14 1.16 1.18 1.20 1.22 1.24 1.26 1.28
1.30 1.32 1.34 1.36 1.38 1.40 1.42 1.44 1.46 1.48
1.50 1.52 1.54 1.56 1.58 1.60 1.62 1.64 1.66 1.68
1.70 1.72 1.74 1.76 1.78 1.80 1.82 1.84 1.86

APPENDIX C

WINDING NUMBER VS. V_{PMAX}/μ

The figures in this appendix show the winding number of the BEC circulation at the end of the simulation, $w(t_{\text{final}})$, plotted versus the parameter $V_{p\text{max}}$ scaled by the chemical potential of the initial state of the BEC, μ. Values of μ for different cases are found in Table 3.1. The different T cases have been offset slightly for clarity, and should be floored to the next lowest integer. These curves are extracted from the final phase distributions shown in Appendix B.

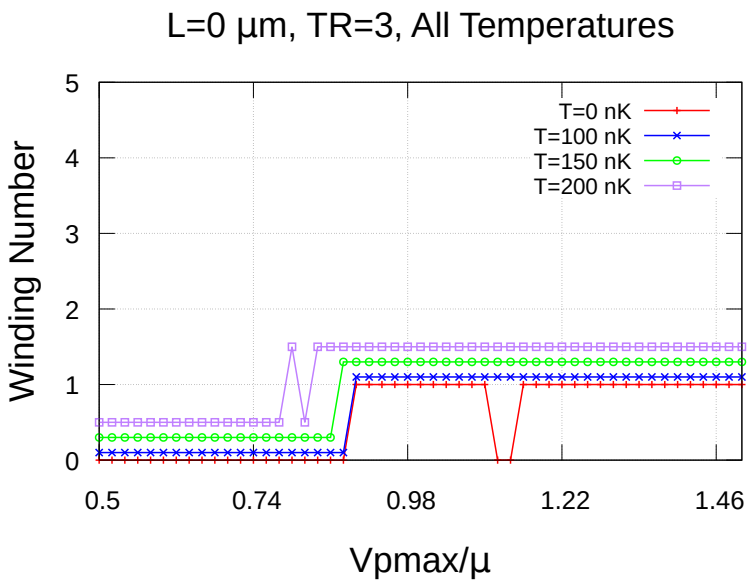

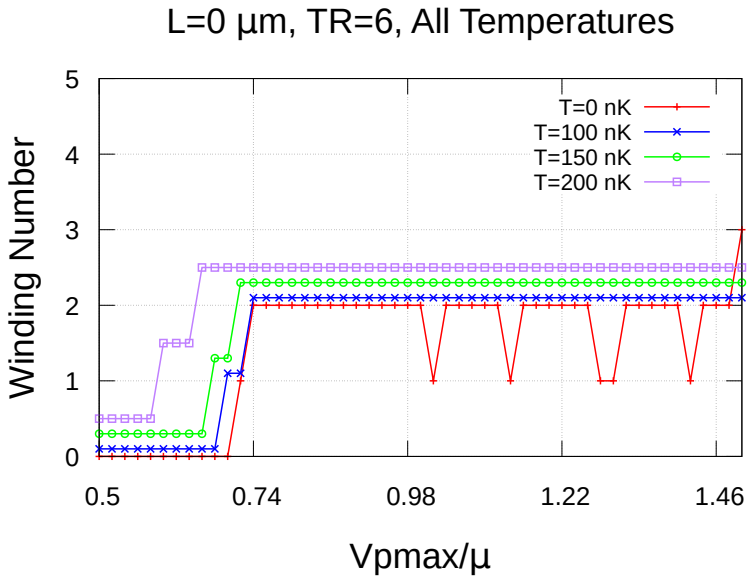
L=0 µm, TR=6, All Temperatures
Winding Number
Vpmax/µ
T=0 nK
T=100 nK
T=150 nK
T=200 nK
0
1
2
3
4
5
0.5
0.74
0.98
1.22
1.46

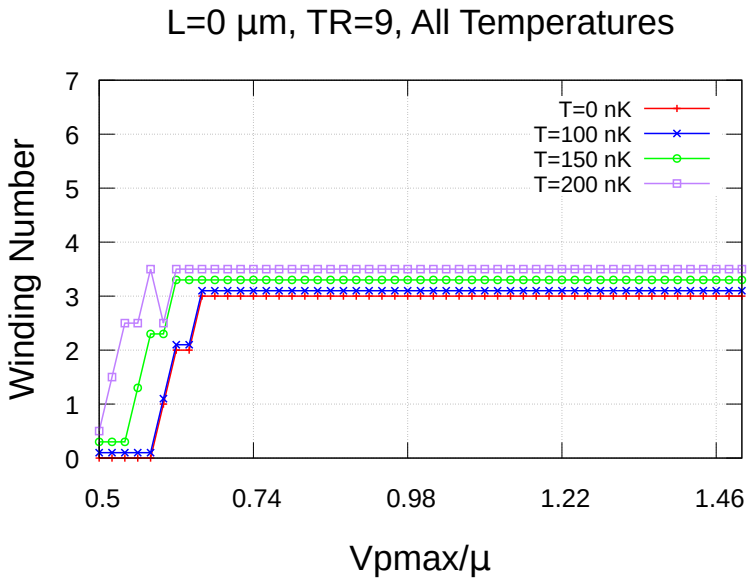
L=0 µm, TR=9, All Temperatures
Winding Number
Vpmax/µ
T=0 nK
T=100 nK
T=150 nK
T=200 nK
0
1
2
3
4
5
6
7
0.5
0.74
0.98
1.22
1.46

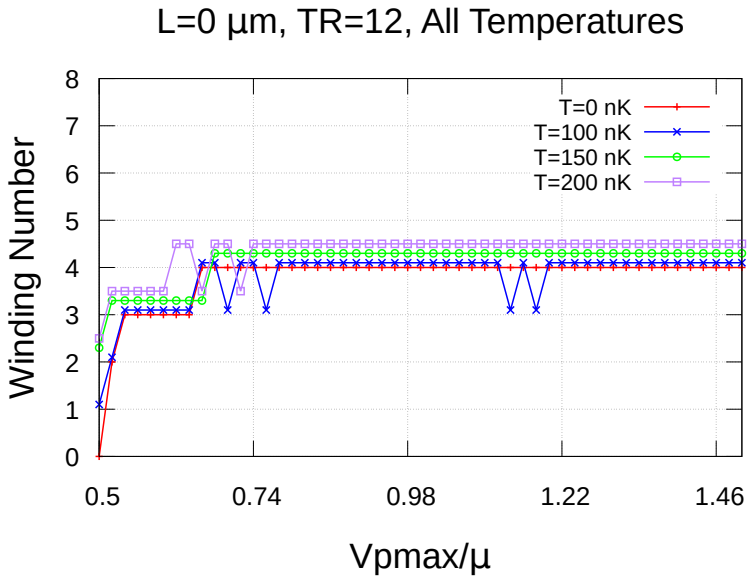
L=0 µm, TR=12, All Temperatures
Winding Number
Vpmax/µ
T=0 nK
T=100 nK
T=150 nK
T=200 nK
0
1
2
3
4
5
6
7
8
0.5
0.74
0.98
1.22
1.46

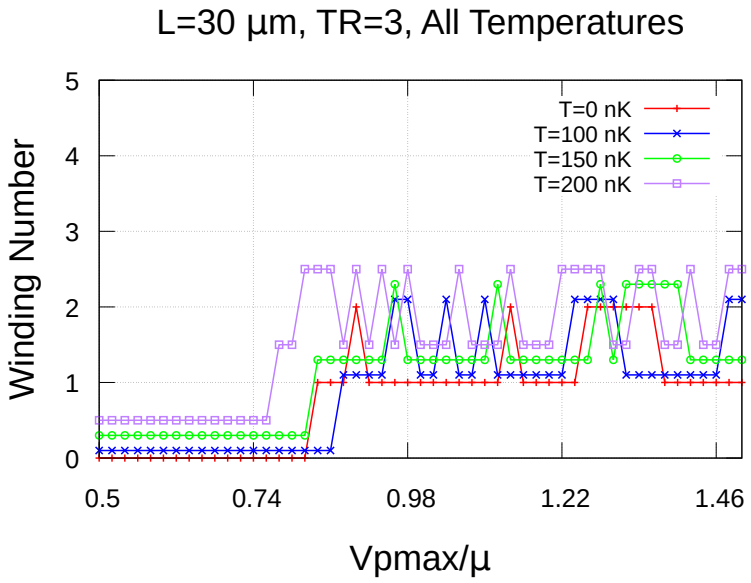
L=30 µm, TR=3, All Temperatures
Winding Number
Vpmax/µ
T=0 nK
T=100 nK
T=150 nK
T=200 nK
0
1
2
3
4
5
0.5
0.74
0.98
1.22
1.46

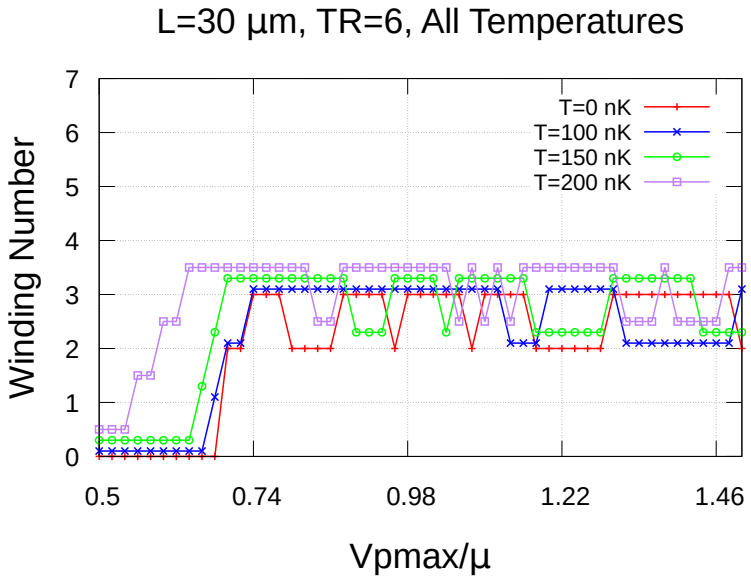
L=30 µm, TR=6, All Temperatures
Winding Number
Vpmax/µ
T=0 nK
T=100 nK
T=150 nK
T=200 nK
0
1
2
3
4
5
6
7
0.5
0.74
0.98
1.22
1.46

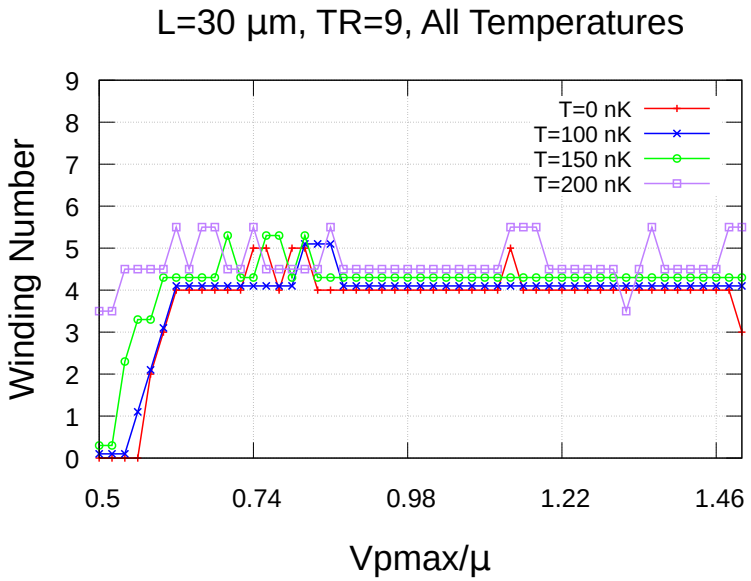
L=30 µm, TR=9, All Temperatures
Winding Number
Vpmax/µ
T=0 nK
T=100 nK
T=150 nK
T=200 nK
0
1
2
3
4
5
6
7
8
9
0.5
0.74
0.98
1.22
1.46

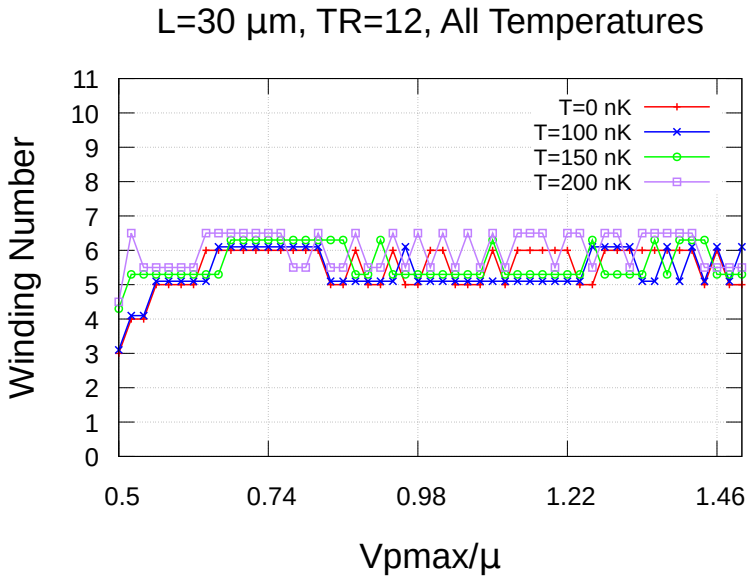
L=30 µm, TR=12, All Temperatures
Winding Number
Vpmax/µ
T=0 nK
T=100 nK
T=150 nK
T=200 nK
0
1
2
3
4
5
6
7
8
9
10
11
0.5
0.74
0.98
1.22
1.46

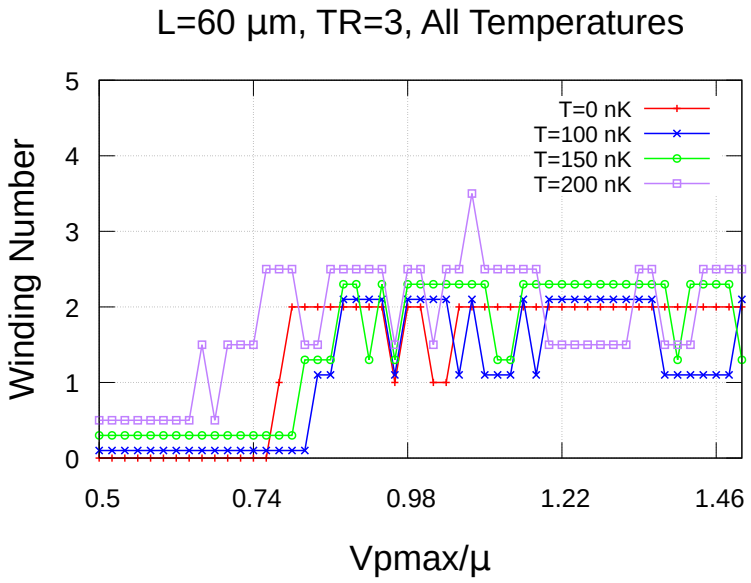
L=60 µm, TR=3, All Temperatures
Winding Number
Vpmax/µ
T=0 nK
T=100 nK
T=150 nK
T=200 nK
0
1
2
3
4
5
0.5
0.74
0.98
1.22
1.46

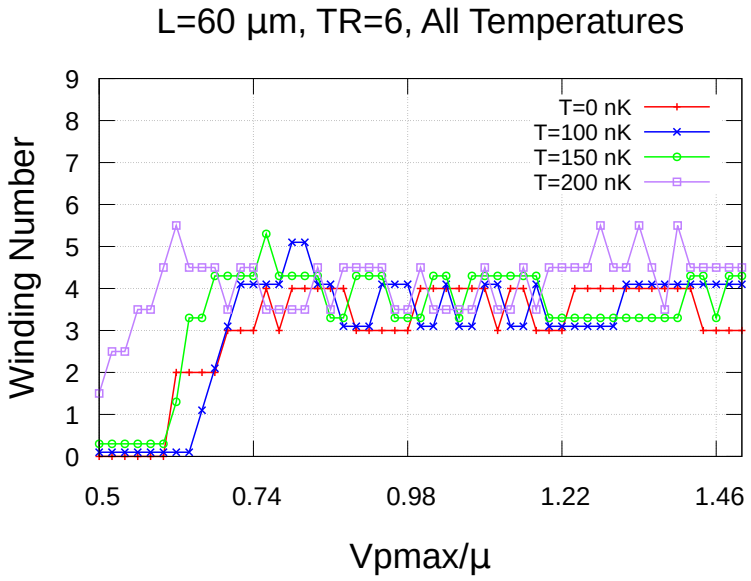
L=60 µm, TR=6, All Temperatures
Winding Number
Vpmax/µ
T=0 nK
T=100 nK
T=150 nK
T=200 nK
0
1
2
3
4
5
6
7
8
9
0.5
0.74
0.98
1.22
1.46

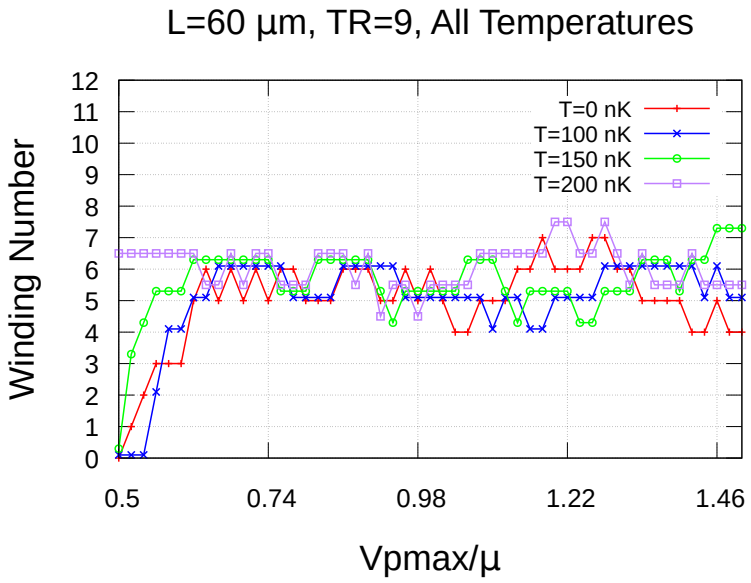
L=60 µm, TR=9, All Temperatures
Winding Number
Vpmax/µ
T=0 nK
T=100 nK
T=150 nK
T=200 nK
0
1
2
3
4
5
6
7
8
9
10
11
12
0.5
0.74
0.98
1.22
1.46

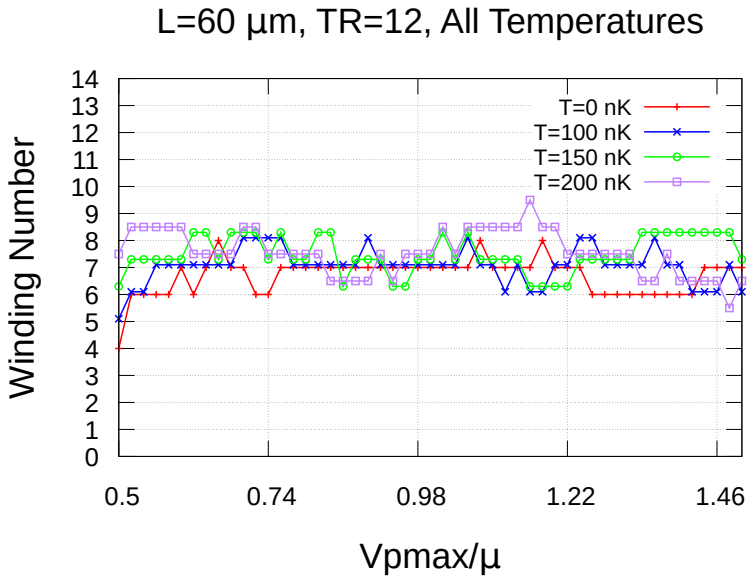
L=60 µm, TR=12, All Temperatures
Winding Number
Vpmax/µ
T=0 nK
T=100 nK
T=150 nK
T=200 nK
0
1
2
3
4
5
6
7
8
9
10
11
12
13
14
0.5
0.74
0.98
1.22
1.46

APPENDIX D

W_{MAX} CHARTS

The figures in this appendix show the maximum winding number, $w_{\max}$, achieved out of all the $V_{p\max}$ for different length, stirring speed, and temperature cases. The values of $w_{\max}(L, \mathrm{TR})$ are shown in the squares.

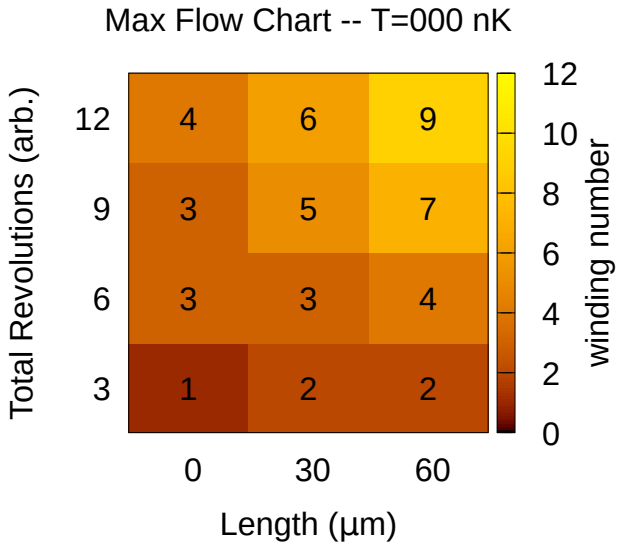

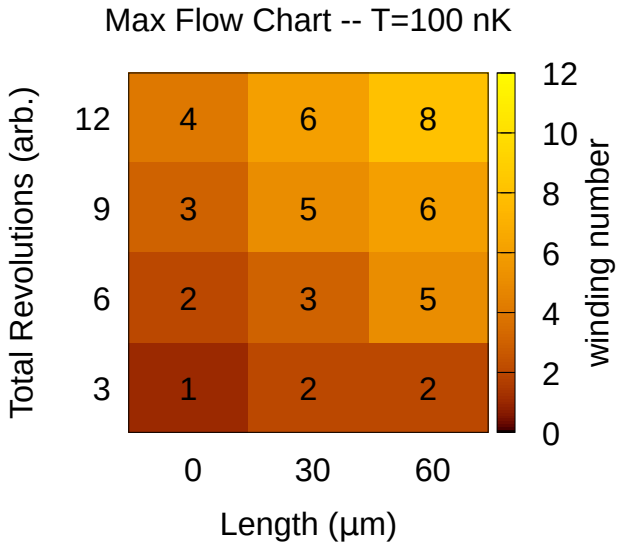

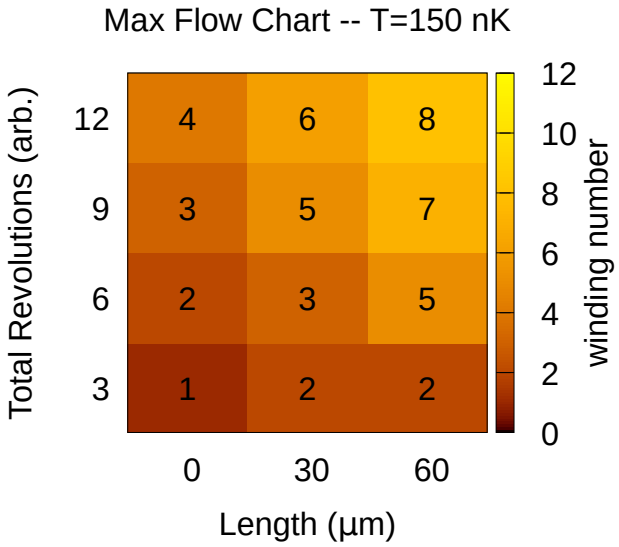
Max Flow Chart -- T=150 nK
Total Revolutions (arb.)
12
9
6
3
4
6
8
3
5
7
2
3
5
1
2
2
0
30
60
Length (µm)
12
10
8
6
4
2
0
winding number

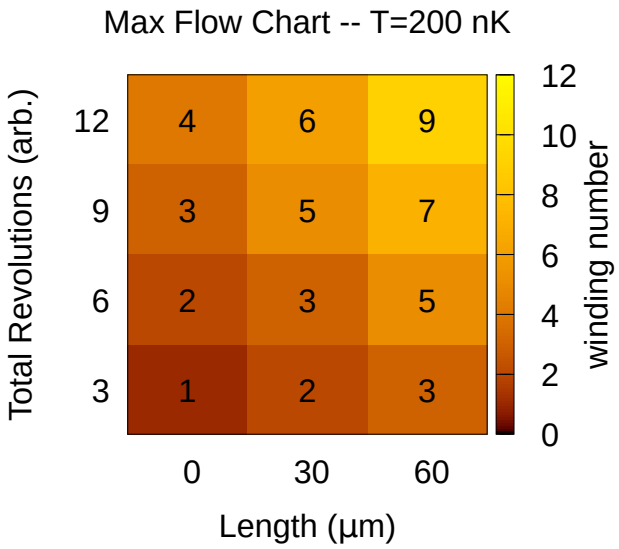
Max Flow Chart -- T=200 nK
Total Revolutions (arb.)
12
9
6
3
4
6
9
3
5
7
2
3
5
1
2
3
0
30
60
Length (µm)
12
10
8
6
4
2
0
winding number